Studies on phase/structure transformable copper coordination polymers using bis(trifluoromethanesulfonyl)imide anion

（ビス（トリフルオロメタンスルホニル）イミドアニオンを用いた相転移あるいは構造変化できる銅配位高分子に関する研究）

北海道大学大学院環境科学院

Xin Zheng

Preface

The study presented in this thesis has been carried out under the direction of Professor Shin-ichiro Noro between October 2015 and September 2020 at Graduate School of Environment Science, Hokkaido University.

The author would like to express his deepest gratitude to Professor Shin-ichiro Noro for his careful guidance, precious suggestions, and persistent encouragements during the course of this work.

The author would like to express his sincere gratitude to Professor Takayoshi Nakamura for his kind suggestions and warm encouragements. The author is deeply grateful to Assistant Professor Kiyonori Takahashi for his inspired suggestions and hearty encouragements. The author is grateful to Professor Ichiro Hisaki (Osaka University), Associate Professor Kazuya Kubo (University of Hyogo) and Assistant Professor Rika Ochi (Kochi University) for their kind advices and continuous encouragements.

The author is thankful to Professor Yuichi Kamiya and Mr. Kazutaka Hashimoto for SEM measurements and helpful suggestions. The author is grateful to Associate Professor Yuh Hijikata and Dr. Jenny Pirillo for theoretical calculations and kind advices. The author is thankful to Associate Professor Masaru Kato for XAS measurements and helpful suggestions. The author is thankful to Dr. Hiroyasu Sato (Rigaku Corporation) for his kind technical supports of single-crystal XRD and kind advices.

The author is thankful to Dr. Jun Xiong, Dr. Masashi Yoshitake, Dr. Yu Ohshima, Mr. Daisuke Nishide for their kind support and hearty encouragements. The author is also thankful to Mrs. Yukiko Takahashi, Mrs. Mayumi Kondo, Mr. Kazushige Suzuki, and Mr. Takashi Ohzeki for their kind experimental help and continuous encouragements during his time in the laboratory. The author is thankful to Mrs. Ayumi Nakaoka for her secretarial works and warm encouragements. Acknowledgements are to all other members of Professor Noro's laboratory and Professor Nakamura's laboratory for their friendship and encouragements.

The author is indebted for the financial support of Ambitious Leading Program in Hokkaido University.

Finally, the author expresses his deep appreciation to his fiancée Ling Li, his parents, Mr. Yi Zheng and Mrs Jihua Wang for constant financial supports and affectionate encouragements.

Xin Zheng

Graduate School of Environment Science

Hokkaido University

September 2020

Contents

Chapter 1

General introduction

1-1. Phase/structure transformations in materials

Phase transformations are ubiquitous in nature and people's lives. For example, humanity has learnt how to utilize the melting process of ice to preserve a food several thousand years ago. Phase transformations are defined as the change in state from one phase to another without composition changes in this thesis. Based on thermodynamic properties of materials, phase transformations can be classified to first-order phase transformations and second-order phase transformations by calculating the partial derivative function of temperature and pressure to free energy at the phase transformation point. If the derivative function is continuous at the phase transformation point, it should be the first-order phase transformation such as melting and freezing as shown in Fig. 1-1, and the materials owning this kind of phase transformations have been widely used for an energy storage.[1]

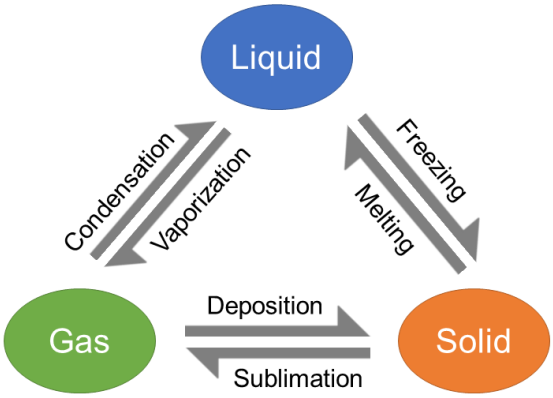

Fig. 1-1 Schematic view of first-order phase transformations among solid, liquid and gas.

At the same time, the uptake and release of guest molecules or exchange of guest molecules can also result in the change of structures that is defined as structure transformations in this thesis. These transformations are also very common such as the water absorption of superabsorbent polymers,[2] intercalation in hydrotalcites,[3] and hydrogen-absorbing metal alloys.[4] In these structure transformations, the compositions of the compounds change due to uptake and release of the guest or exchange of guests as shown in Fig. 1-2.

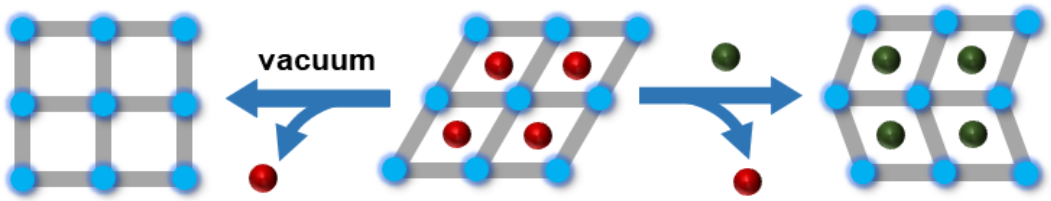

Fig. 1-2 Schematic view of structural transformations.

On one hand, phase and structure transformations helped researchers to understand the nature of some physical phenomena. For example, some researchers found that when the angle between two graphene layers changed by 1.1 degree, the superconductivity appeared.[5] On the other hand, researchers utilized these phase and structure transformations to develop a variety of functional materials. For instance, researchers reported the flexible hydrogen-bonded organic frameworks that are advantageous for operation under ambient air and will expand opportunities of utilizing functional gases in society.[6] In this thesis, I employed a hybrid material, coordination polymer, to develop a variety of structure/phase transformable materials showing interesting physical properties.

1-2. Coordination polymers

Coordination polymers (CPs) that are constructed from metal nodes and organic ligands with infinite one-, two- and three-dimensional (1D, 2D and 3D) structures were firstly reported in 1950s[7] and flourished in recent three decades. They show many potential applications including gas sorption/separation, catalytic, electric and magnetic properties.[8-11] Moreover, a structural diversity of CPs further provides chemists with almost infinite possibilities to design CPs with specific physical properties by introducing the corresponding building blocks,[12] and over 90000 distinct crystalline CPs have been registered in Cambridge Structural Database.[13]

Development of CPs was vastly accelerated in late 1990s as shown in Fig. 1-3,[14] because plenty of CPs with rigid frameworks and ultra-high surface areas were reported and their performances far exceeded other traditional porous materials such as activated carbons and zeolites.[15] However, compared with traditional porous materials, the stability of CPs was usually too poor to promote their industrial applications. Therefore, a lot of researches on improving the stability of CPs have been reported.[16]

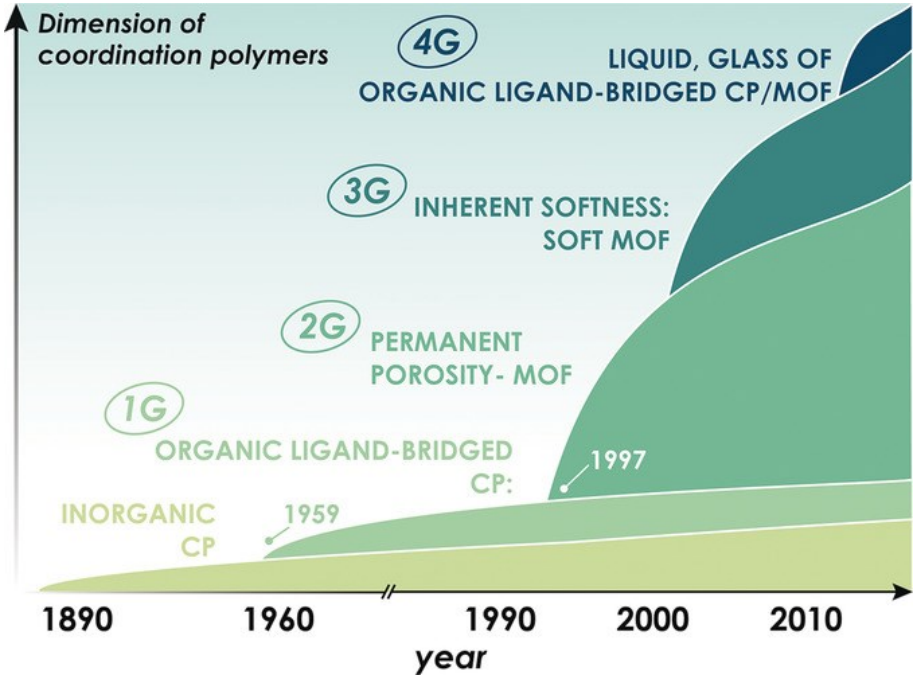

Fig. 1-3. Chronological progression of CPs.[14]

1-3. Structure transformations in CPs

CPs with inherent softness emerged and their flexible frameworks with reversible structure transformations by a guest uptake/release further developed the CPs' chemistry.[17] Different from rigid CPs with high porosity, flexible CPs can rearrange their conformations in tandem with guest molecules and this phenomenon is usually called breathing effect and gate-sorption behavior.[18] This effect, for example, can be ingeniously used to build a higher-energy phase to manage the exothermic/endothermic heat during adsorption/desorption process for higher usable gas capacities.[19] Another example is that a flexible CP, ZnGGH (GGH = H-Gly–Gly–L-His-OH) can identify varied guest molecules and show different reflex to different guest molecules.[20]

Flexible CPs that show structure transformations were firstly categorized into six groups by Kitagawa and Uemura based on the dimensionality of CPs.[21] Recently, Jenkins et. al also grouped them again into four categories based on rigid motifs in the compounds as shown in Fig. 1-4.[22] Firstly, for the dynamic CPs with no rigid dimensions, their frameworks should totally deform under the influence of guest molecules. However, it is difficult to investigate crystal structures of such totally flexible CPs before and after structural transition. Therefore, most of this kind of dynamic CPs utilized the rotation axis between metal clusters and rigid organic ligands to realize the whole contraction instead of using flexible organic ligands to construct the frameworks.[23-27] Secondly, for the dynamic CPs that are rigid in one- or two-dimension, a utilization of flexible organic ligands is very common.[28-32] Some of them contain the flexible organic ligands with polymethylene chains.[30,31] Although their breathing effects related to shrinkage/expansion of polymethylene chains are confirmed by powder X-ray diffraction (XRD) analysis, the specific conformations of polymethylene chains before and after structural transitions are still unknown. Thirdly, for the dynamic CPs that are rigid in 3D, all of them have interpenetration frameworks and the interpenetration frameworks slide slightly when the interactions between guest molecules and the frameworks are strong enough.[33-35]

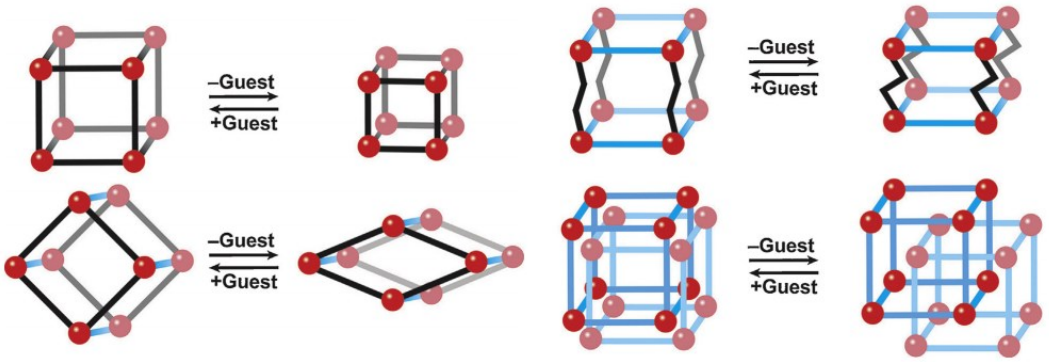

Fig. 1-4. Schematic views showing structure transformations of CPs with 0D, 1D, 2D, and 3D rigid components.[22]

1-4. Phase transformations in CPs

Very recently, beyond crystalline materials, amorphous CPs (liquids and glasses, Fig. 1-5) began to be found (less than 0.5 % of total structures of CPs).[36] Amorphous CPs may lead a new direction in this field due to their potential applications including gas sorption/separation,[37] trapping of a byproduct of nuclear energy production and enhancement of proton conductivities.[38,39]

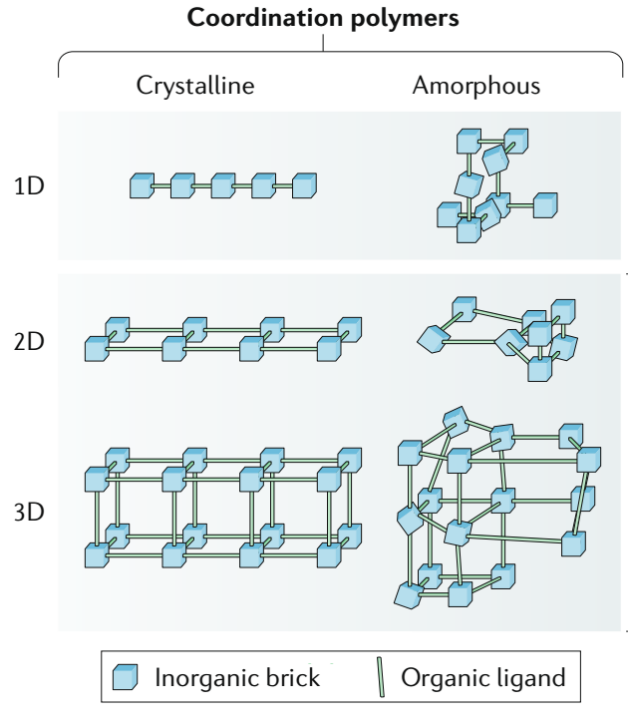

Fig. 1-5 Schematic views between crystalline and amorphous CPs.[36]

Amorphous CP was first reported by Bennett et. al in 2010.[40] They found that the 3D zeolitic imidazolate framework (ZIF), ZIF-4, constructed from zinc(II) ions and imidazolate ligands, melts at 866 K under ambient pressure by heating without decomposition and indicated that the analogy between ZIF-4 and silicate may result in such melting behavior. Horike et. al also reported that the 2D coordination polymer consisting of zinc(II) ions, dihydrogenphosphate anions and triazolate ligands shows a melting at 441 K.[41] Mudring et. al synthesized an 1D coordination polymer constructed from dithiocyanato copper(I) and 1-butyl-4-methyl-pyridinium that can melt at 364 K.[42] It seems that with dimensionality increased, the melting point of CPs increases, because

the components of CPs need more energy to get rid of the restraint of the lattice with dimensionality increased.

Different from crystalline CPs, amorphous CPs cannot be structurally well characterized using single-crystal and powder XRD techniques. The extended X-ray absorption fine structure (EXAFS)[43] and pair distribution function (PDF)[44] analysis based on total scattering are powerful methods to explore their structures, and the same methods have been widely used for investigating inorganic glasses. Solid-state NMR and terahertz (THz)/far-IR are also adopted to reveal the dynamic structures of amorphous CPs recently.[45] Moreover, molecular dynamics simulations provide the concretization of amorphous CPs matched well with experimental results.[46]

One of the most important applications of CPs is gas storage/separation. Amorphous CPs are expected to show potential gas storage/separation properties due to their high plasticity, while the porosity of CPs will inevitably decrease after amorphization. The amorphous CP that can keep porosity was reported very recently,[47] and the authors indicated that the bulky ligand, benzimidazolate, plays the key role for maintaining its porosity after amorphization. It is much easier for amorphous CPs to fabricate membranes without grain boundary structures than crystalline CPs. Jiang et. al first reported a membrane based on ZIF-62 glass that exhibits high separation performance for H_2/CH_4, CO_2/N_2 and CO_2/CH_4 mixtures.[48] Another potential application of amorphous CPs is an ionic conductivity. Horike et. al doped proton sources to a CP liquid and the proton conductivity of the CP glass obtained by a melt-quenching process became several orders of magnitude higher than the original crystalline compound.[49] As mentioned above, amorphous CPs can trap not only nuclear byproduct but also other harmful guest species such as iodine.[50]

Up to now, the research on amorphous CPs is mainly confined to a ZIF family due to their high thermal stability. Furthermore, there is no universal strategy to synthesize phase and structural transformable CPs.

1-5. CPs with anion components of ionic liquids

Ionic liquids (ILs) are usually constructed from organic cations with long polymethylene chains and inorganic polyatomic anions, and most of them can keep a liquid state at room temperature due to a large size and conformational flexibility of both cations and anions that result in small lattice enthalpies and large entropy changes.[51] The fluorinated anions are the most common anions in ILs and believed to be the key for lowering melting points because their delocalized negative charges and low electric polarizability contribute to weak intermolecular interactions. ILs with fluorinated anions have shown better performances in gas separation/recovery, especially for carbon dioxide.[52] For example, researchers found that anions are more effective than cations for promoting carbon dioxide capture in ILs, following the order of $[NO_3] < [SCN] < [MeSO_4] < [BF_4] < [DCA]$ (DCA = dicyanamide) $< [PF_6] < [NTf_2] < [C_7F_{15}CO_2]$,[53] indicating that ILs containing fluorinated anions should have better CO_2 solubilities. ILs with very low vapor pressure were also developed as potential electrolytes in batteries. Therefore, CPs with components of ILs could show interesting physical and chemical properties.

In order to obtain CPs with components of ILs, two strategies were adopted; one is to insert ionic liquids into the pores of CPs,[54] and another is to utilize components of ILs as building blocks to construct new CPs.[55] For the former strategy, CPs with high porosity are good containers to capture ILs. However, the strong host-guest interactions prevented the performances of loaded ILs.[56] Therefore, post impregnation approach is the most widely used nowadays, although the durability of such kind of IL-loaded CPs remains much scope for improvement.[57] Jiang et. al reported a series of IL-loaded CPs, [BMIM][A]/IRMOF-1, (BMIM = 1-*n*-butyl-3-methylimidazolium, A = BF_4^-, PF_6^-, NTf_2^- and SCN^-) for CO_2/N_2 separation.[58] Contrast to the CO_2/N_2 selectivity of pure ILs, the selectivity increases in the order of $[NTf_2^-] < [PF_6^-] < [BF_4^-] < [SCN^-]$, because the interaction between $BMIM^+$ and NTf_2^- is strongest among four kinds of anions when they are located in the pores of IRMOF-1.

For the later strategy, our group reported a variety of flexible CPs by introducing the small fluorinated anions, BF_4^-, PF_6^- and $CF_3SO_3^-$, which are widely used in ILs, into the frameworks. For example, the 1D flexible copper CP, $[Cu(PF_6)_2(bpe)_2]$ (bpe = 1,2-bis(4-pyridyl)ethane) with small fluorinated PF_6^- anions has the highly selective CO_2 adsorption behavior with three-step structural transformations, although the framework has no porosity originally.[59] Another flexible CP with longer organic ligands and larger fluorinated anions, $[Cu(CF_3SO_3)_2(bpp)_2]$ (bpp = 1,3-bis(4-pyridyl)propane), was reported, and its adsorption mechanism was proposed to accompany with a structural transformation from the closed form to the open form of the crystal based on 1D chains.[60] Kondo et. al investigated the selective CO_2 gate adsorption behavior of $[Cu(BF_4)_2(bpp)_2]$ by a powder XRD analysis and proposed that quasi-hexagonal cavities surrounded by six BF_4^- anions can recognize the CO_2 molecules.[61] In addition, thanks to low Lewis basicity of fluorinated anions, metal nodes cannot restrain anions tightly, leading to the structural transformations with the cleavage/reformation of metal-anion coordination bonds.[62] Based on these reported CPs, I can conclude that introducing the fluorinated anions as building blocks for CPs is effective for synthesizing phase/structure transformable CPs with high probability.

1-6. Survey of this thesis

The main purpose of this thesis is to explore phase/structure transition behaviors of flexible CPs constructed from components of ILs. In this thesis, a bulky fluorinated anion, bis(trifluoromethylsulfonyl)imide (NTf_2^-), which is one of the most popular anions in ILs with excellent CO_2 absorption performances, is adopted as one building block to construct phase/structure-transformable CPs. Because the NTf_2^- anion with highly delocalized negative charges as well as two revolving axes as shown in Fig. 1-6 is sensitive to guest molecules such as CO_2 and thermal stimuli,[63] phase/structure transformations could be observed in NTf_2-containing CPs. At the same time, organic ligands owning flexible polymethylene chains (Fig. 1-6) are selected as other building blocks to build dynamic CPs. As introduced above, the polymethylene chains are known to show the conformation changes during the phase/structure transitions.

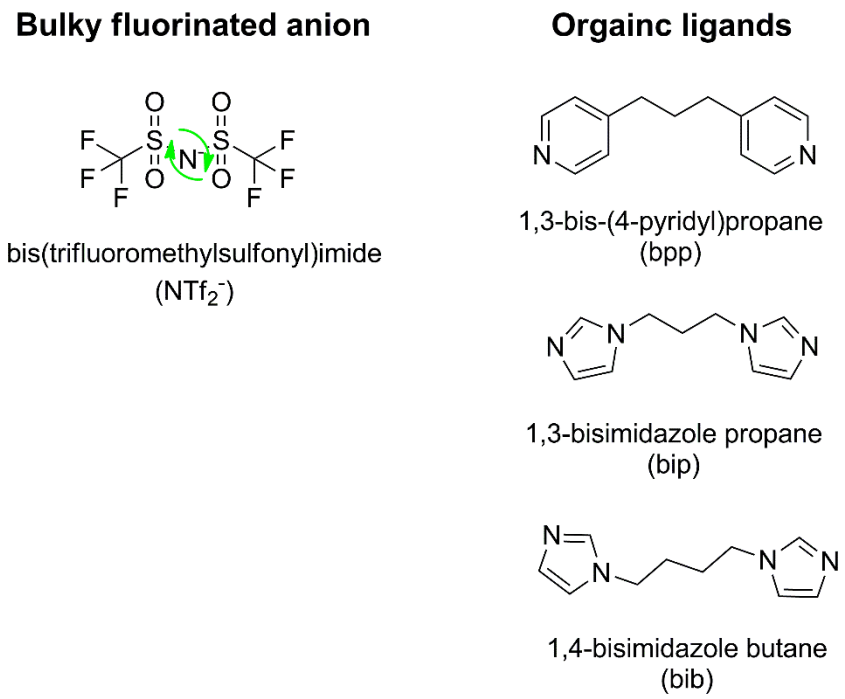

Fig. 1-6. Chemical structures of an NTf_2^- anion and organic ligands used in this thesis.

Chapter 2 describes a visualization of interactions between components of a ionic liquid and absorbed CO_2 using a flexible 1D CP $[Cu(NTf_2)_2(bpp)_2]$ (**1**). Analysis of the structure of a CO_2-loaded crystal using single-crystal X-ray diffraction analysis reveals

that CO_2 interacts with both fluorine and oxygen atoms of NTf_2^- anions in a *trans* rather than *cis* conformation about the S-N bond. Theoretical analysis of the structure of the CO_2-loaded crystal indicates that dispersion and electrostatic interactions exist between CO_2 and the framework. The overall results provide important insight into understanding and improving the CO_2 adsorption properties of ILs.

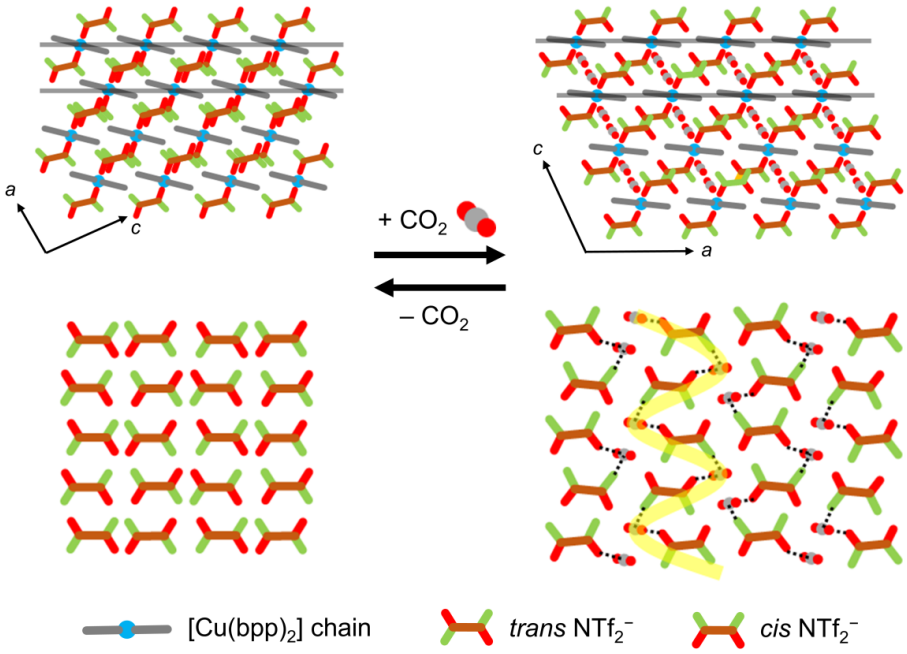

Chapter 3 describes the effect of uptake/release of coordinated molecules on gate-sorption behavior in flexible CP **1**, in which NTf_2^- anions are weakly constrained by Cu(II) ions. A series of small organic molecules, MeCN, DMF and DMSO that can coordinate to Cu(II) ions are introduced to make an impact on the structure. After removing coordinated guest molecules, the decrease in crystallite sizes and the slight change in coordination skeleton are observed and NTf_2^- anions coordinate to Cu(II) ions instead of coordinated guest molecules. CO_2 adsorption/desorption isotherms for **1** are affected after uptake and release of coordinated molecules, while they keep almost the same adsorption amount for CO_2.

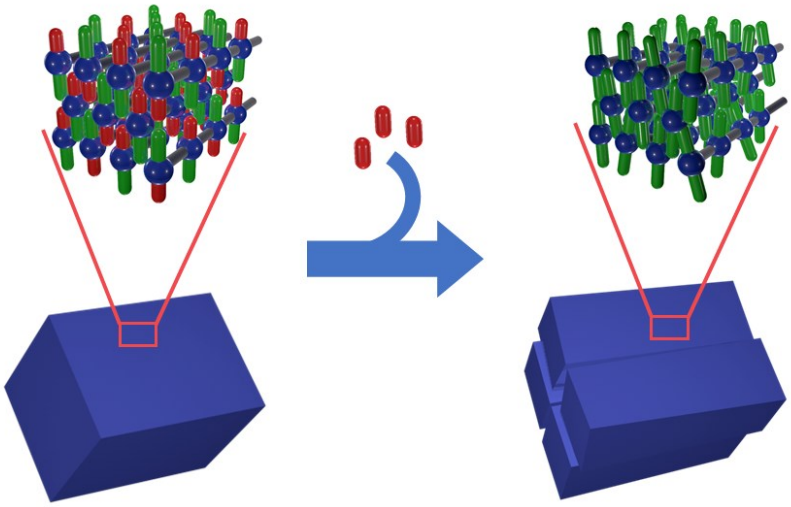

Chapter 4 describes a synchronous change in fluid space and encapsulated anions in a flexible 3D CP, $[Cu(bib)_{2.5}]$ (**3**), containing organic bridging ligands, bib with conformationally flexible tetramethylene ($(CH_2)_4$) unit. The combined results of DSC measurements, single-crystal X-ray diffraction analysis and impedance spectroscopy demonstrate that this CP encapsulating NTf_2^- anions contains fluid space and that it undergoes a crystal-to-crystal transition in association with a synchronous change in the conformations of both the bib ligand, caused by C-C bond rotation, and the NTf_2^- anion stemming from rotation about the N-S bond.

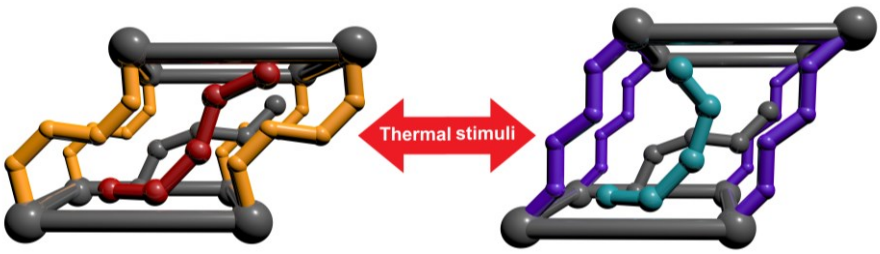

Chapter 5 describes the CP liquid and glass using the CP **3**. It has the lowest melting points (T_m), 303 K, and the lowest glass transition temperature (T_g), 448 K, among all 3D CPs that can melt without decomposition and the glass-forming ability that can be calculated by T_g/T_m ratio is 0.68, similar to those of melt-quenched glasses. Such low T_m and T_g are caused by its flexible cationic skeleton and encapsulated NTf_2^- anions

with flexible structure. The ionic conductivity of the glass state of **3** is several times higher than the crystalline **3** at the same temperature.

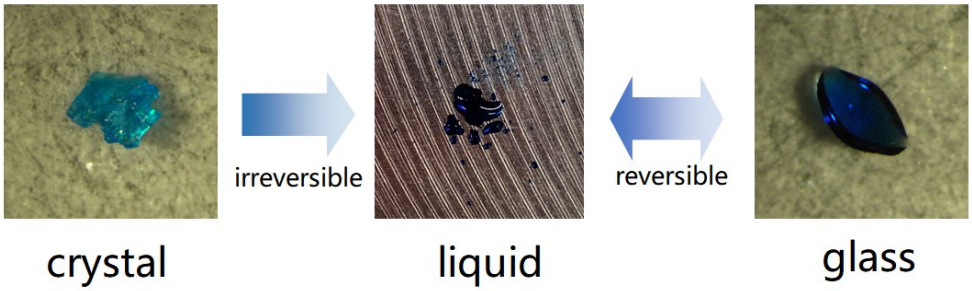

Chapter 6 deals with a 2D $\{[Cu(bip)_2(DMSO)_2]\cdot 2NTf_2\}$ (**4**·2DMSO) that can irreversibly convert to the 1D chain structure $[Cu(NTf_2)_2(bip)_2]$ (**4**) after removing coordinated DMSO molecules. Both **4**·2DMSO and **4** were structurally characterized. In **4**·2DMSO, one Cu(II) ion coordinates with four organic ligands and two DMSO molecules, while NTf_2^- anions are free in the frameworks. In **4**, one Cu(II) ion coordinates with four organic ligands and two NTf_2^- anions. This structural information reveals that the recombination of not only weak axial coordination bonds but also normal equatorial coordination bonds occurs during the irreversible 2D to 1D structure transformation. **4** owned reversible and irreversible phase transitions at high temperature region.

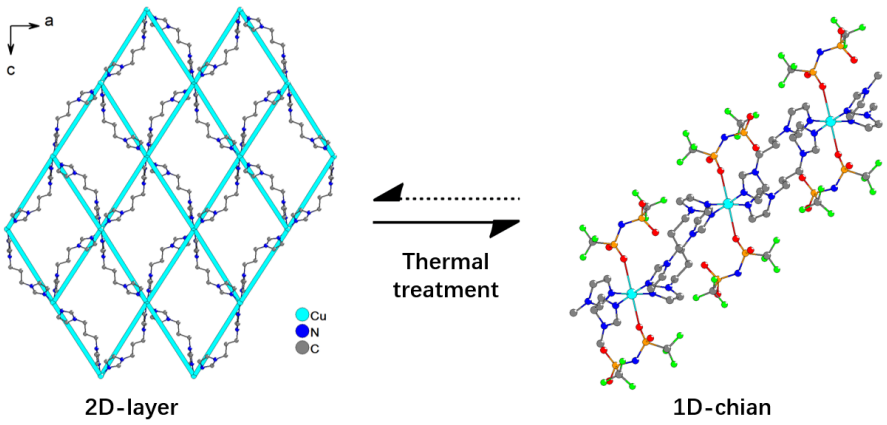

1-7. References

1. Y. Lin, et al., Review on thermal conductivity enhancement, thermal properties and applications of phase change materials in thermal energy storage. *Renew Sust. Energ. Rev.* **2018**, *82*, 2730.
2. X. Ma, , G. Wen, Development history and synthesis of super-absorbent polymers: a review. *J. Polym. Res.* **2020**, *27*, 136.
3. C. Chen, *et al.*, Synergistic effect of graphene oxide@phosphate-intercalated hydrotalcite for improved anti-corrosion and self-healable protection of waterborne epoxy coating in salt environments. *J. Mater. Chem. C* **2019**, *7*, 2318.
4. K. L. Hodge & J. E. Goldberger, Transition Metal-Free Alkyne Hydrogenation Catalysis with BaGa2, a Hydrogen Absorbing Layered Zintl Phase. *J. Am. Chem. Soc.* **2019**, *141*, 19969.
5. Y. Cao, *et al.*, Correlated insulator behaviour at half-filling in magic-angle graphene superlattices. *Nature* **2018**, *556*, 80.
6. Q. Huang, *et al.*, An exceptionally flexible hydrogen-bonded organic framework with large-scale void regulation and adaptive guest accommodation abilities. *Nat. Commun.* **2019**, *10*, 3074.
7. K. Yukio, *et al.*, The Crystal Structure of Bis(adiponitrilo)copper(I) Nitrate. *Bull. Chem. Soc. Jpn.* **1959**, *32*, 1221.
8. J.-R. Li, *et al.*, Carbon dioxide capture-related gas adsorption and separation in metal-organic frameworks. *Coord. Chem. Rev.* **2011**, *255*, 1791.
9. J.-Y. Lee, *et al.*, Metal–organic framework materials as catalysts. *Chem. Soc. Rev.* **2009**, *38*, 1450.
10. A. A. Talin, *et al.*, Tunable Electrical Conductivity in Metal-Organic Framework Thin-Film Devices. *Science* **2014**, *343*, 66.
11. G. Lorusso, *et al.*, A Dense Metal–Organic Framework for Enhanced Magnetic Refrigeration. *Adv. Mater.* **2013**, *25*, 4653.
12. B. M. Connolly, *et al.*, Shaping the Future of Fuel: Monolithic Metal–Organic Frameworks for High-Density Gas Storage. *J. Am. Chem. Soc.* **2020**, 142, 8541.

13. P. Z. Moghadam, *et al.*, Development of a Cambridge Structural Database Subset: A Collection of Metal–Organic Frameworks for Past, Present, and Future. *Chem. Mater.* **2017**, *29*, 2618.
14. S. Horike, *et al.*, A New Dimension for Coordination Polymers and Metal–Organic Frameworks: Towards Functional Glasses and Liquids. *Angew. Chem. Int. Ed.* **2020**, *59*, 6652.
15. Z. Chen, *et al.*, Balancing volumetric and gravimetric uptake in highly porous materials for clean energy. *Science* **2020**, *368*, 297.
16. M. Ding, *et al.*, Improving MOF stability: approaches and applications. *Chem. Sci.* **2019**, *10*, 10209.
17. A. Schneemann, *et al.*, Flexible metal–organic frameworks. *Chem. Soc. Rev.* **2014**, *43*, 6062.
18. C. Serre, *et al.*, Very Large Breathing Effect in the First Nanoporous Chromium(III)-Based Solids: MIL-53 or $Cr^{III}(OH)\cdot\{O_2C\text{-}C_6H_4\text{-}CO_2\}\cdot\{HO_2C\text{-}C_6H_4\text{-}CO_2H\}_x\cdot H_2O_y$. *J. Am. Chem. Soc.* **2002**, *124*, 13519.
19. J. A. Mason, *et al.*, Methane Storage in Flexible Metal-Organic Frameworks With Intrinsic Thermal Management. *Nature* **2015**, *527*, 357.
20. A. P. Katsoulidis, *et al.*, Chemical control of structure and guest uptake by a conformationally mobile porous material. *Nature* **2019**, *565*, 213.
21. S. Kitagawa & K. Uemura, Dynamic porous properties of coordination polymers inspired by hydrogen bonds. *Chem. Soc. Rev.* **2005**, *34*, 109.
22. C. R. Murdock, *et al.*, Approaches for synthesizing breathing MOFs by exploiting dimensional rigidity. *Coord. Chem. Rev.* **2014**, *258*, 119.
23. D. F. Jimenez, *et al.*, Opening the Gate: Framework Flexibility in ZIF-8 Explored by Experiments and Simulations. *J. Am. Chem. Soc.* **2011**, *133*, 8900.
24. S. A. Moggach, *et al.*, The Effect of Pressure on ZIF-8: Increasing Pore Size With Pressure and the Formation of a High-Pressure Phase at 1.47 GPa. *Angew. Chem. Int. Ed.* **2009**, *48*, 7087.
25. C. Yang, *et al.*, Crystallographic Observation of Dynamic Gas Adsorption Sites

and Thermal Expansion in a Breathable Fluorous Metal-Organic Framework. *Angew. Chem. Int. Ed.* **2009**, *48*, 2500.

26. C. M. Draznieks, *et al.*, Very Large Swelling in Hybrid Frameworks: A Combined Computational and Powder Diffraction Study. *J. Am. Chem. Soc.* **2005**, *127*, 16273.
27. Y. S. Wei, *et al.*, Turning on the flexibility of isoreticular porous coordination frameworks for drastically tunable framework breathing and thermal expansion. *Chem. Sci.* **2013**, *4*, 1539.
28. G. Ferey & C. Serre, Large breathing effects in three-dimensional porous hybrid matter: facts, analyses, rules and consequences. *Chem. Soc. Rev.* **2009**, *38*, 1380.
29. M. Taddei, *et al.*, Synthesis, breathing, and gas sorption study of the first isoreticular mixed-linker phosphonate based metal–organic frameworks. *Chem. Commun.* **2013**, *49*, 1315.
30. C. R. Murdock, *et al.*, Effects of Solvation on the Framework of a Breathing Copper MOF Employing a Semirigid Linker. *Inorg. Chem.* **2013**, *52*, 2182.
31. G. Alberti, *et al.*, Pillared Derivatives of γ-Zirconium Phosphate Containing Nonrigid Alkyl Chain Pillars. *J. Am. Chem. Soc.* **1998**, *120*, 9291.
32. R. M. P. Colodrero, *et al.*, Multifunctional lanthanum tetraphosphonates: Flexible, ultramicroporous and proton-conducting hybrid frameworks. *Dalton Trans.* **2012**, *41*, 4045.
33. S. Yang, *et al.*, A Partially Interpenetrated Metal-Organic Framework for Selective Hysteretic Sorption of Carbon Dioxide. *Nat. Mater.* **2012**, *11*, 710.
34. Y. Sakata, *et al.*, Shape-Memory Nanopores Induced in Coordination Frameworks by Crystal Downsizing. *Science* **2013**, *339*, 193.
35. Y. Gu, *et al.*, Structural-Deformation-Energy-Modulation Strategy in a Soft Porous Coordination Polymer with an Interpenetrated Framework. *Angew. Chem. Int. Ed.* **2020**, *132*, 1.
36. T. D. Bennett & S. Horike, Liquid, glass and amorphous solid states of coordination polymers and metal–organic frameworks. *Nat. Rev. Mater.* **2018**, *3*,

431.

37. C. Zhou, *et al.*, Metal-organic framework glasses with permanent accessible porosity. *Nat. Comm.* **2018**, *9*, 5042.
38. K. W. Chapman, *et al.*, Metal-organic framework glasses with permanent accessible porosity. *J. Am. Chem. Soc.* **2011**, *133*, 18583.
39. W. Chen, *et al.*, Glass Formation of a Coordination Polymer Crystal for Enhanced Proton Conductivity and Material Flexibility. *Angew. Chem. Int. Ed.* **2016**, *55*, 5195.
40. T. D. Bennett, *et al.*, Structure and Properties of an Amorphous Metal-Organic Framework. *Phys. Rev. Lett.* **2010**, *104*, 115503.
41. D. Umeyama, *et al.*, Inherent Proton Conduction in a 2D Coordination Framework. *J. Am. Chem. Soc.* **2012**, *134*, 12780.
42. E. T. Spielberg, *et al.*, (1-Butyl-4-methyl-pyridinium)[$Cu(SCN)_2$]: A Coordination Polymer and Ionic Liquid. *Chem. Eur. J.* **2014**, *20*, 5338.
43. X. Wu, *et al.*, Packaging and delivering enzymes by amorphous metal-organic frameworks. *Nat. Comm.* **2019**, *10*, 5165.
44. J. Hou, *et al.*, Metal-organic framework crystal-glass composites. *Nat. Comm.* **2019**, *10*, 2580.
45. J. Hou, *et al.*, Halogenated Metal–Organic Framework Glasses and Liquids. *J. Am. Chem. Soc.* **2020**, *142*, 3880.
46. R. Gaillac, *et al.*, Liquid metal–organic frameworks. *Nat. Mat.* **2017**, *16*, 1149.
47. R. N. Widmer, *et al.*, Pressure Promoted Low-Temperature Melting of Metal-Organic Frameworks. *Nat. Mat.* **2019**, *18*, 370.
48. Y. Wang, *et al.*, A MOF Glass Membrane for Gas Separation. *Angew. Chem. Int. Ed.* **2020**, *59*, 4365.
49. S. S. Nagarkar, *et al.*, Enhanced and Optically Switchable Proton Conductivity in a Melting Coordination Polymer Crystal. *Angew. Chem. Int. Ed.* **2017**, *56*, 4976.
50. T. D. Bennett, *et al.*, Ball-Milling-Induced Amorphization of Zeolitic Imidazolate Frameworks (ZIFs) for the Irreversible Trapping of Iodine. *Chem. Eur. J.* **2013**,

19, 7049.

51. I. Krossing, *et al.*, Why Are Ionic Liquids Liquid? A Simple Explanation Based on Lattice and Solvation Energies. *J. Am. Chem. Soc.* **2006**, *128*, 13427.
52. X. Zhang, *et al.*, Carbon capture with ionic liquids: overview and progress. *Energy Environ. Sci.*, **2012**, *5*, 6668.
53. M. Ramdin, *et al.*, State-of-the-Art of CO_2 Capture with Ionic Liquids. *Ind. Eng. Chem. Res.* **2012**, *51*, 8149.
54. K. Kazuyuki, *et al.*, Ionic liquid transported into metal–organic frameworks. *Coord. Chem. Rev.* **2016**, *307*, 382.
55. S. Noro & T. Nakamura, Fluorine-functionalized metal–organic frameworks and porous coordination polymers. *NPG Asia Mater.* **2017**, *9*, 433.
56. E. R. Parnham & R. E. Morris, Ionothermal Synthesis of Zeolites, Metal–Organic Frameworks, and Inorganic–Organic Hybrids. *Acc. Chem. Res.* **2007**, *40*, 1005.
57. Y. Yoshida & H. Kitagawa, Ionic Conduction in Metal–Organic Frameworks with Incorporated Ionic Liquids. *ACS Sustainable Chem. Eng.* **2019**, *7*, 70.
58. K. M. Gupta, *et al.*, Metal–organic framework supported ionic liquid membranes for CO_2 capture: anion effects. *Phys. Chem. Chem. Phys.* **2012**,*14*, 5785.
59. S. Noro, *et al.*, Selective Gas Adsorption in One-Dimensional, Flexible Cu^{II} Coordination Polymers with Polar Units. *Chem. Mater.* **2009**, *21*, 3346.
60. K. Fukuhara, *et al.*, Porous Coordination Polymer Polymorphs with Different Flexible Pores Using a Structurally Flexible and Bent 1,3-Bis(4-pyridyl)propane Ligand. *Inorg. Chem.* **2013**, *52*, 4229.
61. T. Suzuki, *et al.*, Structural Investigation of a Flexible MOF [$Cu(BF_4)_2$(1,3-bis(4-pyridyl)propane)$_2$] Showing Selective Gate Adsorption with Dynamic Pore-Opening/Pore-Closing Processes. *J. Phys. Chem. C* **2016**, *120*, 21571.
62. S. Noro, *et al.*, Selective separation of larger molecules from a Lewis-base mixture by flexible one-dimensional Cu(II) coordination polymer with shape-recognizing space. *Chem. Commun.* **2010**, *46*, 3134.
63. K. Fujii, *et al.*, Conformational Equilibrium of Bis(trifluoromethanesulfonyl)

Imide Anion of a Room-Temperature Ionic Liquid: Raman Spectroscopic Study and DFT Calculations. *J. Phys. Chem. B* **2006**, *110*, 8179.

Chapter 2

Understanding the interactions between the bis(trifluoromethylsulfonyl)imide anion and absorbed CO_2 using X-ray diffraction analysis of a soft crystal surrogate

Abstract

The selective carbon dioxide (CO_2) adsorption properties of ionic liquids (ILs) are highly pertinent to the development of methods to capture CO_2. Although it has been reported that fluorinated components give ILs enhanced CO_2 solubilities, it has been challenging to gain a deep understanding of the interactions occurring between ILs and CO_2. In this investigation, I have utilized the soft crystalline material $[Cu(NTf_2)_2(bpp)_2]$ (**1**), in which NTf_2 is bis(trifluoromethylsulfonyl)imide, bpp is 1,3-bis-(4-pyridyl)propane, as a surrogate for single-crystal X-ray diffraction analysis to visualize interactions occurring between CO_2 and NTf_2^-, the fluorinated IL component that is responsible for high CO_2 solubility. Analysis of the structure of a CO_2-loaded crystal reveals that CO_2 interacts with both fluorine and oxygen atoms of NTf_2^- anions in a *trans* rather than *cis* conformation about the S-N bond. Theoretical analysis of the structure of the CO_2-loaded crystal indicates that dispersion and electrostatic interactions exist between CO_2 and the framework. The overall results provide important insight into understanding and improving the CO_2 adsorption properties of ILs.

2-1. Introduction

Ionic liquids (ILs) have received increasing attention in the past several decades owing to their wide variety of potential industrial applications.[1-3] This is especially true for ILs that have selective CO_2 adsorption properties as a result of the tremendous interest in and urgency for stemming global warming by removal of greenhouse gases from the atmosphere.[4] It is known that anion components of ILs significantly influence CO_2 adsorption capacities and that fluorine containing anions are superior CO_2 absorbers as compared to those that lack this halogen.[5] This phenomenon is exemplified by the bis(trifluoromethylsulfonyl)imide (NTf_2^-) anion, which is one of the most interesting building blocks for the construction of ILs with high CO_2 adsorption propensities.[6] Although several theories have been advanced to explain the physical interactions that take place between NTf_2^--containing ILs and CO_2, some of which have been tested experimentally and by using simulations,[7-12] a full understanding of the interactions has not yet been gained. In particular, based on the current state of knowledge, it is still not possible to ascertain whether oxygen or fluorine is the key CO_2 adsorption site in NTf_2^-, and to determine the nature of primary interactions occurring between this anion and this gas. The main hurdle to obtaining this information is associated with difficulties with determining the structures of ILs owing to their non-crystalline nature. In addition, the conformationally flexible structure of the NTf_2^- anion, originating from reasonably rapid rotation (barrier of 25.1 kJ mol^{-1}) of the CF_3SO_2 substituent around the S-N bond, complicates elucidation of the IL-CO_2 interactions.

Recently, a new class of materials, referred to as soft crystals, has attracted great attention. These materials can exist in both a highly crystalline and soft states, which can be reversibly interconverted in response to external chemical and physical stimuli.[13,14] Interestingly, some of the soft materials retain their single crystalline nature upon being treated with external stimuli. I envisaged that it might be possible to design and fabricate soft crystals, which contain components that are the same as or similar to those present in ILs, and that might possess the ability to absorb CO_2 in synchrony with stimuli promoted structural changes. In this way, it would be possible to utilize these

substances as surrogates to determine the structures of and elucidate important interactions in ILs containing absorbed CO_2 using standard single-crystal X-ray diffraction techniques.

To explore this proposal, I prepared a new soft crystal $[Cu(NTf_2)_2(bpp)_2]$ (**1**), which is composed of an NTf_2^- anion and the flexible 1,3-bis(4-pyridyl)propane (bpp) ligand and Cu^{2+} (Fig. 2-1) that possess an alkyl chain and positively charged Cu^{2+} coordinated nitrogen centers that are typical of those present in a ILs (e.g., the alkylimidazolium and NTf_2^-containing IL in Fig. 2-1). In the effort described below, I demonstrated that the soft crystal **1** displays reversible adsorption of CO_2 associated with a stimulus induced structural transformation, while retaining its permanent single crystalline nature. Moreover, by using standard single-crystal X-ray diffraction techniques, we elucidated the nature of interactions with the NTf_2^- anion that are responsible for CO_2 adsorption.

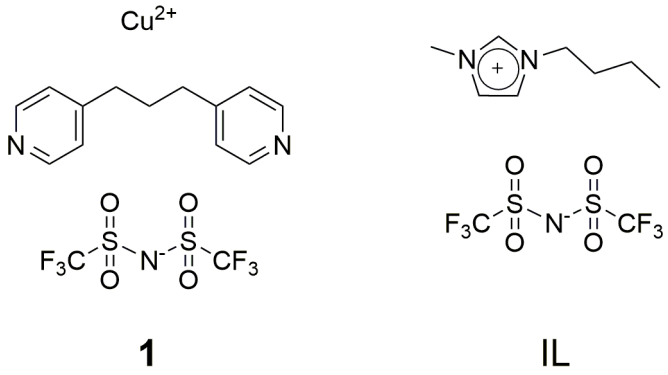

Fig. 2-1. Structures of the components of soft crystal **1** and a typical IL [1-*n*-butyl-3-methylimidazolium][NTf_2^-] containing NTf_2^-.[6]

2-2. Results and discussion

A single-crystal of **1** was prepared by using the diffusion method and a three-phase system including a 0.1 M aqueous $Cu(NTf_2)_2$ bottom layer, a 1:1 water and MeOH, middle layer, and 0.2 M bpp in MeOH top layer. Upon standing, this system generated transparent and rod-like purple single crystals, which were shown by using elemental analysis to have the desired atomic composition and purity. The soft crystal **1** crystallized in the monoclinic space group *P*2/*n*, containing crystallographically independent one copper ion, two NTf_2^- anions and two bpp ligands. The copper ion, surrounded by two NTf_2^- anions and four bpp ligands, exists in a distorted octahedral environment (Fig. 2-2(a)). The distance between the copper ion and NTf_2^- anions (Cu1-O1 = 2.801(2) Å) is much longer than that between the copper ion and the bpp ligands (Cu1–N1 = 2.002(2) Å, Cu1–N2 = 2.013(3) Å) as a consequence of Jahn-Teller distortion and the weak coordination ability of NTf_2^-. The NTf_2^- anions exist in a *trans* conformation, which is known to be thermodynamically more stable than the *cis* conformation.[15] The bpp ligands bridge the copper ion to form one-dimensional (1D) chains oriented along the *b*-axis with a toroidal space of 6.4 Å × 12.2 Å (Fig. 2-2(b)). The 1D chains aggregate through weak CH/π interactions to form quasi two-dimensional (2D) layers with an interchain distance of 9.9 Å (Fig. 2-2(c)). In addition, NTf_2^- anions are sandwiched between the 2D layers through weak coordinative interactions, in which the distance between two neighboring layers is 8.0 Å (Fig. 2-2(c)). The 2D layers and NTf_2^- anions are densely packed through the above-mentioned weak coordinative interactions and weak hydrogen bonding interactions between the trifluoromethylsulfonyl groups of NTf_2^- and pyridyl groups of the bpp ligands (Fig. 2-2(d)). As a result, almost no pores exist in the crystal structure of **1**, and the pore space calculated by using MERCURY software (probe radius: 1.2 Å, approximately grid spacing: 0.7 Å) is only 0.7%.

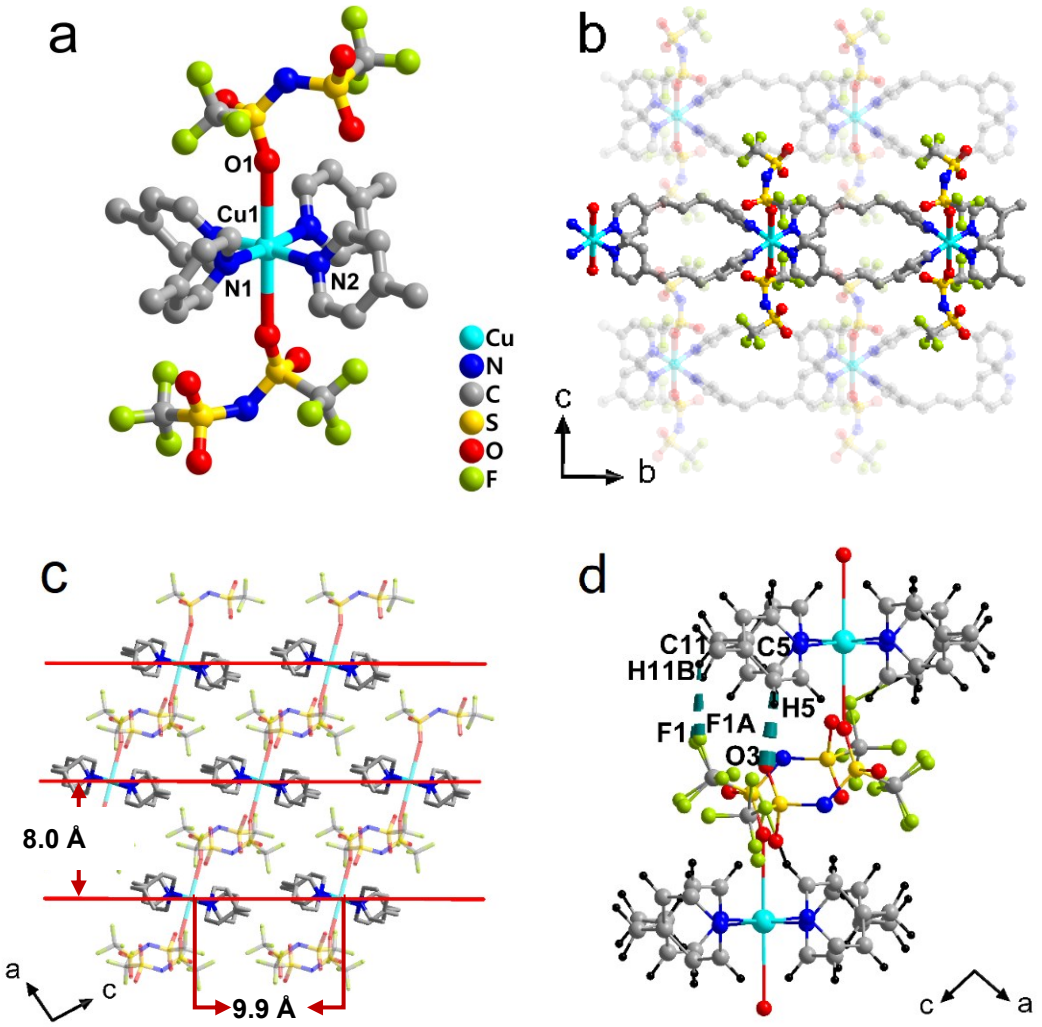

Fig. 2-2. Views of the crystal structure of **1**. (a) Coordination environment around the Cu center in; (b) 1D chain structure; (c) Packing structure viewed along *b* axis; (d) View of the interchain interactions. (The CF_3 parts in **1** are disordered over two sites with occupancies of 0.66 and 0.34)

Inspection of adsorption/desorption isotherms of **1** displayed in Fig. 2-3(a) shows that almost no adsorption of N_2 and Ar occurs at 77 K and 195 K proving that this soft crystal has a densely assembled structure. In contrast, **1** exhibits a steep increase and decrease in the amount of absorbed CO_2 at $P/P_0 = 0.21$ and 0.09, respectively, and 195 K, which suggests that adsorption of this gas takes place in association with a change between a closed and an open structure.[16] The saturated adsorption amount of CO_2 was found to be 2.03 mol mol^{-1} at $P/P_0 = 0.98$, which corresponds to 1.02 mol per mol of

NTf_2. This value is close to those of NTf_2-containing CO_2 absorbing ILs at 313 K and 40 bar (under this condition, adsorption by NTf_2-containing ILs is ca. 0.5 CO_2 mole fraction, corresponding to 1 mol per one mol of NTf_2).[17]

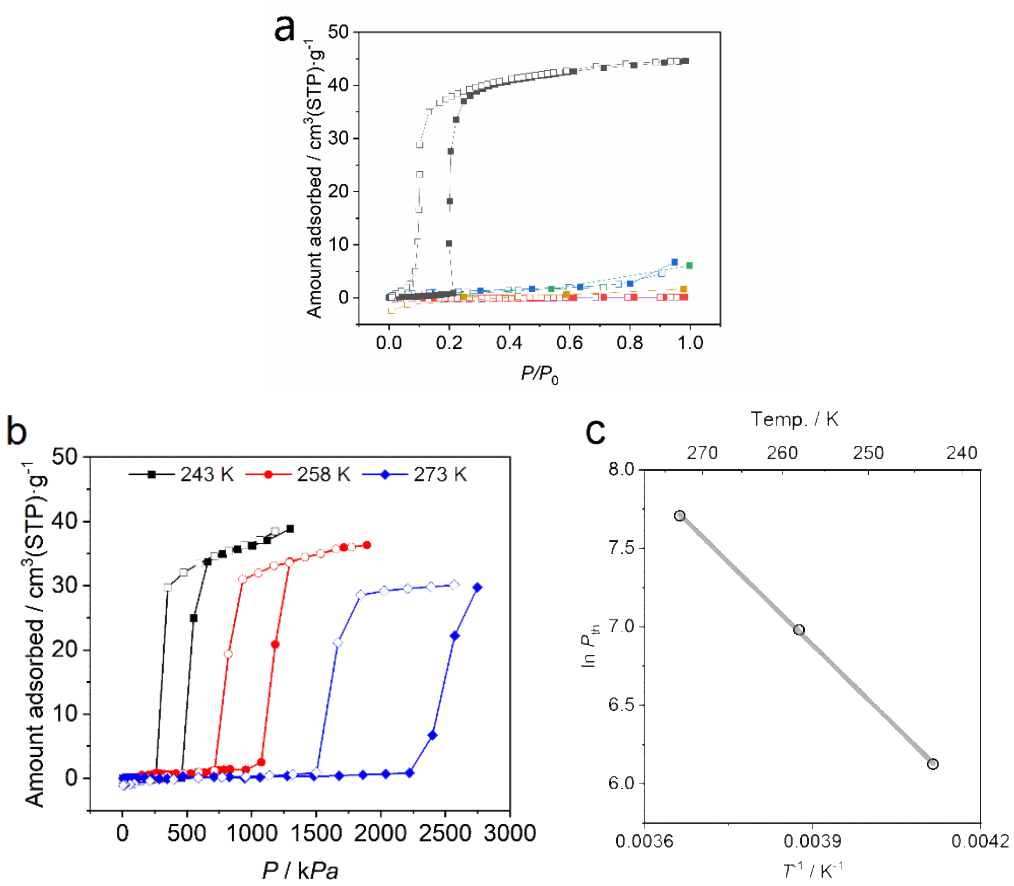

Fig. 2-3. (a) Adsorption (closed symbols)/desorption (open symbols) isotherms of CO_2 (black), N_2 (red), Ar (purple) at 195 K (CO_2), N_2 (green), Ar (blue) at 77 K and H_2O (yellow) 298 K for **1**. (b) CO_2 adsorption (closed symbols)/desorption (open symbols) isotherms for **1** at 243 K (black), 258 K (red), and 273 K (blue). (c) Plot of ln P_{th} against T^{-1}.

The integer number (2 mol mol^{-1}) of the amount of CO_2 absorbed at saturation indicates that specific adsorption sites are present in the soft crystal **1**. The results of investigation of the variable-temperature CO_2 adsorption of **1** reveal that similar behavior is followed but that different threshold pressures exist in the adsorption and desorption isotherms (Fig. 2-3(b)). From the CO_2 adsorption isotherms at different

temperatures, remarkable threshold points (P_{th}) are determined and they are regarded as the equilibrium pressures for the CO_2 adsorption reaction. The enthalpy of CO_2 adsorption (Q_{st}) can be calculated using the following Clausius-Clapeyron equation:

$$Q_{st}/R = d \ln P_{th}/dT^{-1}$$

where R and Q_{st} represent the gas constant and the enthalpy of adsorption, respectively. The plot of ln P_{th} versus T^{-1} yields the straight line (Fig. 2-3(c)), whose slope affords the Q_{st} = –29.1 kJ mol^{-1}. This enthalpy value is only moderate when compared with those of other CO_2 adsorption/adsorption materials including a 30 wt% monoethanolamine solution (–72 to –79 kJ mol^{-1}),[18] amine-functionalized porous organic polymer (–61 kJ/mol)[19] and zeolites (–49.1, –50.0 and -38.0 kJ mol^{-1} for NaX, Na-ZSM-5 and H-ZSM-5, respectively).[20] [1-*n*-Alkyl-3-methylimidazolium][NTf_2^-] (alkyl = ethyl, butyl, and hexyl) ILs have smaller Q_{st} values ranging from –11 to –14 kJ mol^{-1} because of more limited physisorption between dynamic liquid and a gas phase.[21] The only moderate Q_{st} value among those of other solid adsorbents suggests that the interaction between NTf_2^- in **1** and CO_2 and/or that between bpp and CO_2 is not strong.

The stability and absorbability of **1** for water, which are important issues when contemplating practical uses, were also investigated. NTf_2^- anion is hydrophobic as reflected by the fact that the IL [1-*n*-butyl-3-methylimidazolium][NTf_2^-] (Fig. 2-1) has a low absorbability for water and a CO_2 adsorption capacity that is not effected by water adsorption.[17] The soft crystal **1** also has negligible H_2O absorbability (Fig. 2-3(a)). Furthermore, soaking in neutral and acidic (0.1 M HCl) H_2O for 2 d does not affect the powder X-ray diffraction (PXRD) patterns of **1** (Fig. 2-4). These results show that **1** has outstanding stability and low water absorbability.

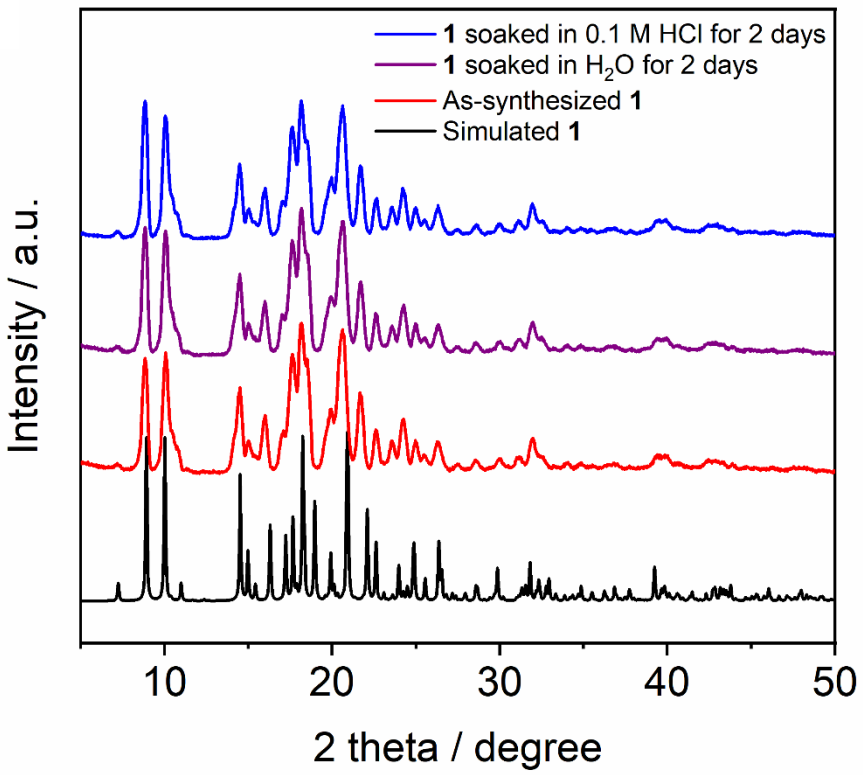

Fig. 2-4 Calculated PXRD pattern of **1** from its single-crystal X-ray structure (black) and observed PXRD patterns of as-synthesized **1** (red), **1** soaked in H_2O (purple) and 0.1 M HCl (blue) for 2 days.

To investigate the effect of fluorine on CO_2 adsorption/desorption properties, I prepared a nonfluorinated version of **1**, $[Cu(NMes_2)_2(bpp)_2]$ (**2**) ($NMes_2^-$ = bis(methanesulfonyl)amide, Fig. 2-5(a)). In **2**, the copper ion is surrounded by two $NMes_2^-$ anions and four bpp ligands to show a distorted octahedral environment (Fig. 2-5(b)). The distance between the copper ion and $NMes_2^-$ anions (Cu1–O1 = 2.48(1) Å, Cu1–O2 = 2.64(1) Å) is much longer than that between the copper ion and the bpp ligands (Cu1–N1 = 2.021(6) Å, Cu1–N2 = 2.029(9) Å, Cu1–N3 = 2.060(7) Å, Cu1–N4 = 2.04(1) Å) as a consequence of Jahn-Teller distortion. The bpp ligands bridge the copper ion to form one-dimensional (1D) chains oriented along the *b*-axis with a toroidal space of 6.0 Å × 11.5 Å (Fig. 2-5(c)). The 1D chains aggregate through weak CH/π interactions to form quasi two-dimensional (2D) layers with an interchain

distance of 10.6 Å (Fig. 2-5(d)). In addition, $NMes_2^-$ anions are sandwiched between the 2D layers through weak coordinative interactions, in which the distance between two neighboring layers is 9.7 Å (Fig. 2-5(d)). The 2D layers and $NMes_2^-$ anions are densely packed through the above-mentioned weak coordinative interactions and weak hydrogen bonding interactions between the sulfonyl groups of $NMes_2^-$ and pyridyl groups of the bpp ligands (Fig. 2-5(e)). Its pore space calculated by using MERCURY software (probe radius: 1.2 Å, approximately grid spacing: 0.7 Å) is 1.0 % near to **1** whose void space is 0.7 %.

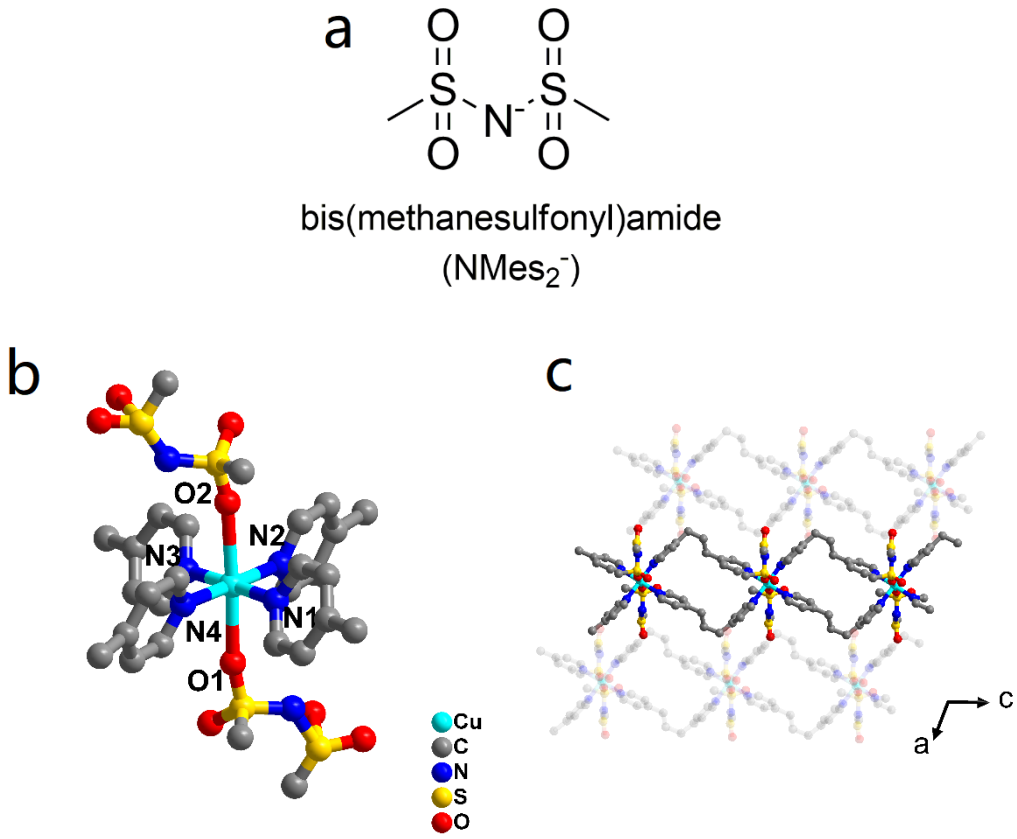

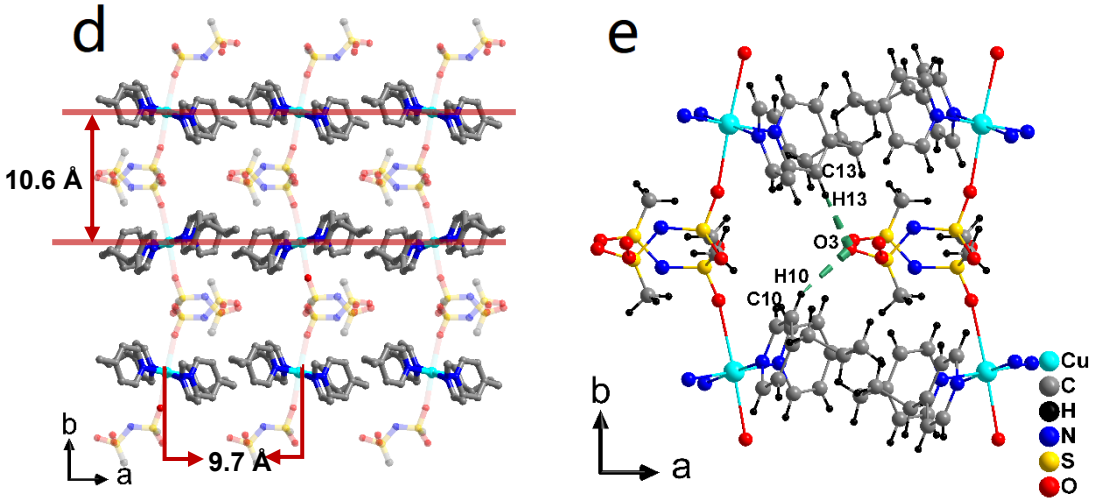

Fig. 2-5. Views of the crystal structure of **2**. (a) the non-fluorinated anion, $NMes_2^-$; (b) Coordination environment around the Cu center in; (c) 1D chain structure; (d) Packing structure viewed along *c* axis; (e) View of the interchain interactions.

Investigation of adsorption/desorption isotherms of **2** displayed in Fig. 2-6 shows a steep increase and decrease in the amount of absorbed CO_2 at P/P_0 = 0.32 and 0.05, respectively, at 195 K, while in **1**, the corresponding values are 0.21 and 0.09. These results indicate that **2** is less flexible compared with the soft crystal **1** due to a lack of fluorinated components. The saturated adsorption amount of CO_2 was found to be near the integer number 3 mol mol^{-1} at P/P_0 = 1 (2.95 mol mol^{-1}), implying that **2** should also have the specific adsorption sites for CO_2 molecules.

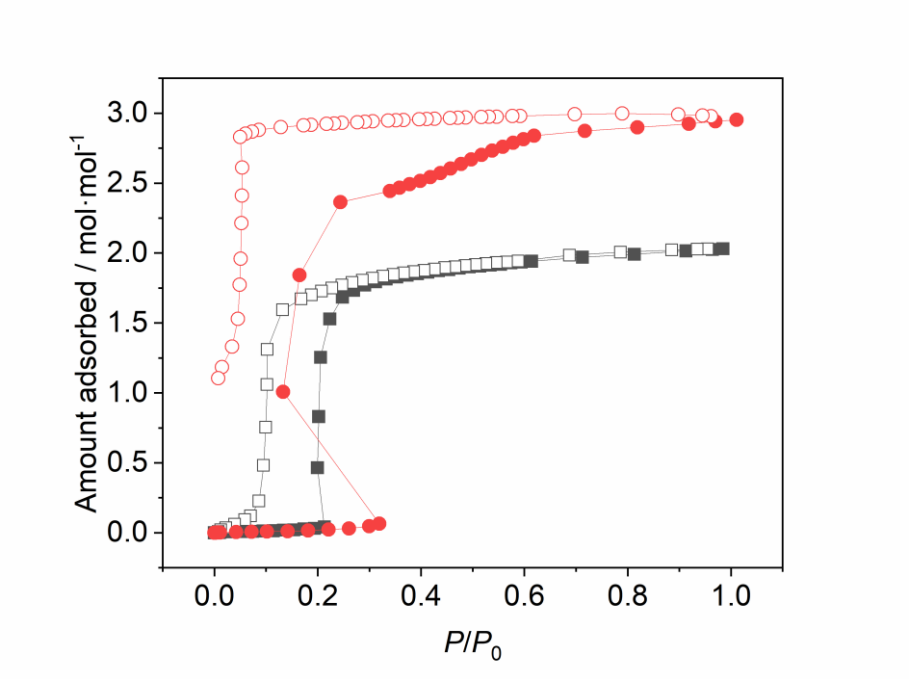

Fig. 2-6. Adsorption (closed symbols)/desorption (open symbols) isotherms of CO_2 for **1** (black) and **2** (red) at 195 K.

The stability and absorbability of **2** for water were also investigated. Different from the hydrophobic NTf_2^- anion, the $NMes_2^-$ anion is hydrophilic, and the CP **2** quickly captures atmospheric water molecules. As shown in Fig. 2-7(a), **2** starts to adsorb H_2O from low relative pressure and the saturated adsorption amount of H_2O in **2** was found to be 3.09 mol mol^{-1} at P/P_0 = 0.98, near to the integer number 3 mol mol^{-1} and the saturated adsorption amount of CO_2, suggesting that CO_2- and H_2O-adsorbed structures of **2** are similar to each other. Furthermore, variable-temperature PXRD patterns prove that **2** has a reversible H_2O adsorbing capacity as shown in Fig. 2-7(b).

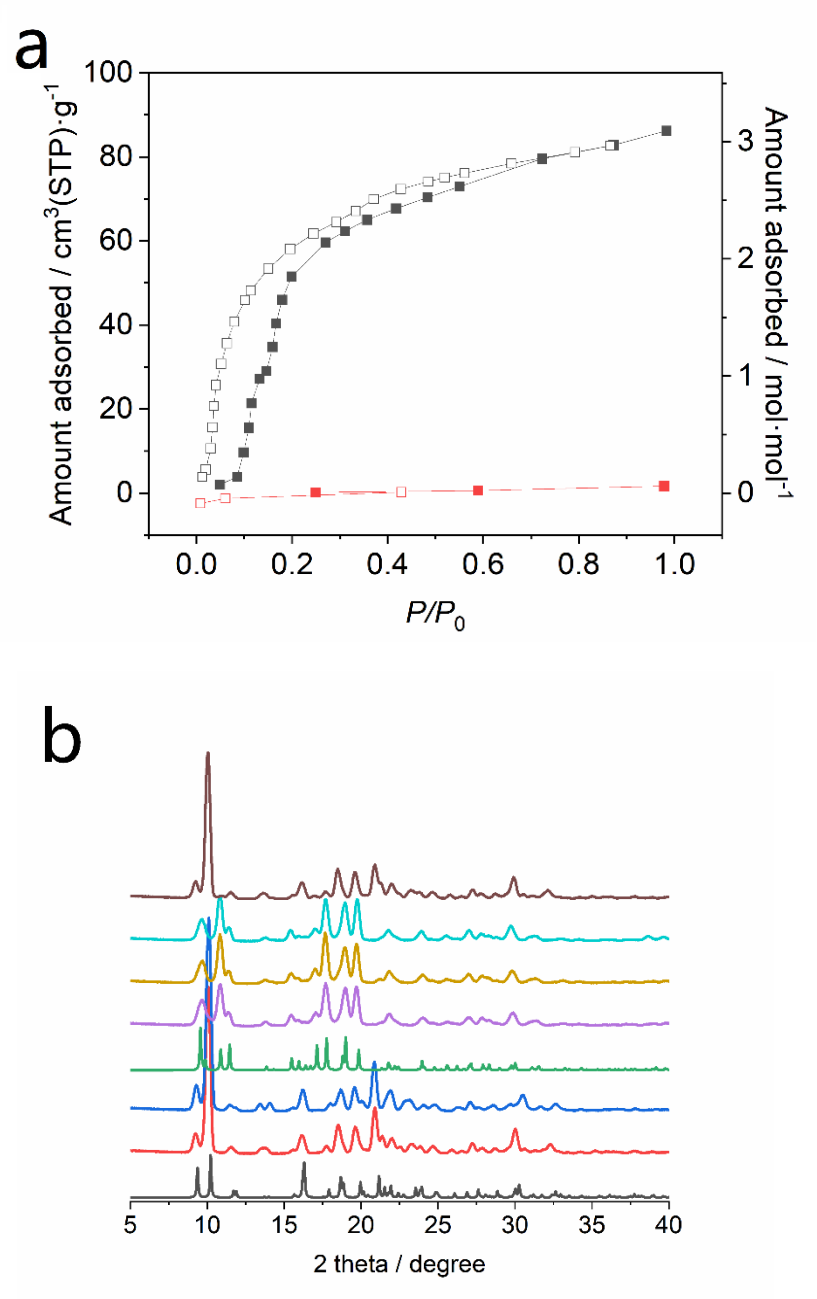

Fig. 2-7 (a) Adsorption (closed symbols)/desorption (open symbols) isotherms of CO_2 for **1** (red) and **2** (black) at 298 K. (b) Calculated PXRD patterns of **2**·3H_2O (black) and **2** (green) from their single-crystal X-ray structures at 293 K, PXRD patterns of as-synthesized **2**·3H_2O at 298 K (red), 323 K (blue), 348 K (purple), 373 K (yellow) and after cooling at 298 K (cyan), and PXRD pattern of the sample obtained by an exposure of **2** to a humidified air (relative humidity = 64 %) for 15 minutes (brown).

Because soft crystal **1** retains its single crystalline nature after adsorption of CO_2, I

was able to determine the structure of the CO_2-loaded crystal **1**·2CO_2 by using standard single-crystal X-ray diffraction analysis. The space group of **1**·2CO_2 was found to be *C*2/*c*, which can be considered as being a transform to a *C*-centered lattice with space group *P*2/*n*. The coordination environments of the copper ion in **1** and **1**·2CO_2 are similar (Fig. 2-8(a)), while the distance between the cooper center and NTf_2^- anion is 7% shorter (Cu1′-O1′ = 2.600(2) Å) and that between the cooper center and bpp ligands is slightly longer (Cu1′–N1′ = 2.015(3) Å, Cu1′–N2′ = 2.018(3) Å) in **1**·2CO_2 compared to **1**. The toroidal shape of 1D chains in **1**·2CO_2 are almost unchanged (6.3 Å × 12.3 Å, Fig. 2-8(b)) in contrast with **1**, and the dihedral angles of neighboring pyridine rings coordinated to the same copper ions decrease from 69°/68° in **1** to 59°/64° in **1**·2CO_2. Moreover, **1**·2CO_2 contains slightly different quasi 2D layers in contrast to **1**. Specifically, each 1D chain in **1**·2CO_2 is inclined against the plane composed of copper ions, resulting in a slightly larger interchain distance (10.3 Å) (Fig. 2-8(c)). The interlayer space is occupied by both NTf_2^- anions and CO_2 molecules, and the presence of absorbed CO_2 causes a significant expansion of the interlayer distance from 8.0 to 8.6 Å (Fig. 2-8(c)). Consequently, the cell volume of **1**·2CO_2 is 8.5 % larger than that of **1** largely because of a 7.5% expansion of the interlayer.

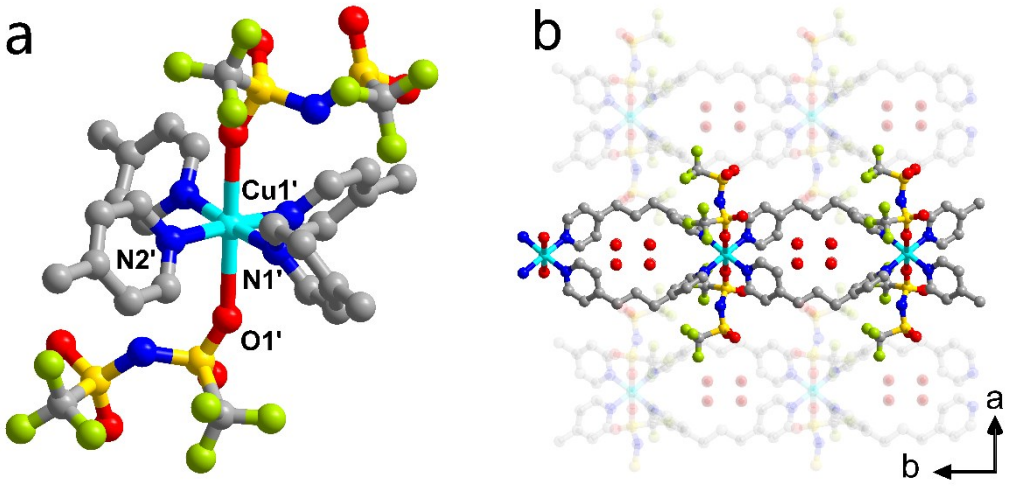

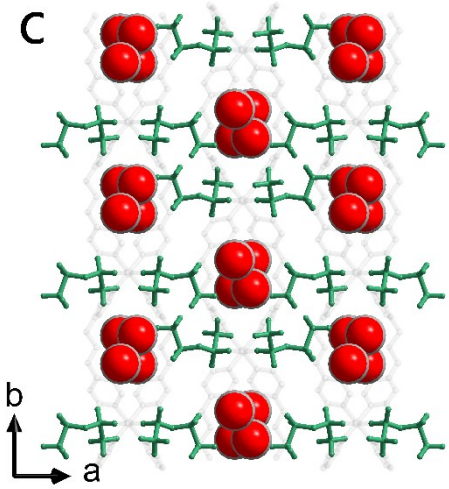

Fig. 2-8. Views of the crystal structure of **1**·CO_2. (a) Coordination environment around the Cu center; (b) 1D chain structures; (c) Conformation of NTf_2^-.

As mentioned above, all NTf_2^- anions in **1** are arranged in a parallel manner in the *trans* conformation (Fig. 2-9(a)). However, after CO_2 adsorption, six NTf_2^- anions exist in a *cis* conformation and are positioned at corners of hexagonal vertexes (Fig. 2-9(b)) to form a cavity which encloses two CO_2 molecules (Fig. 2-9(c)). The significant changes taking place in the interlayer distance and conformation of NTf_2^- anions, along with other slight structural changes suggest that the soft crystal **1** undergoes induced-fit to accommodate CO_2.

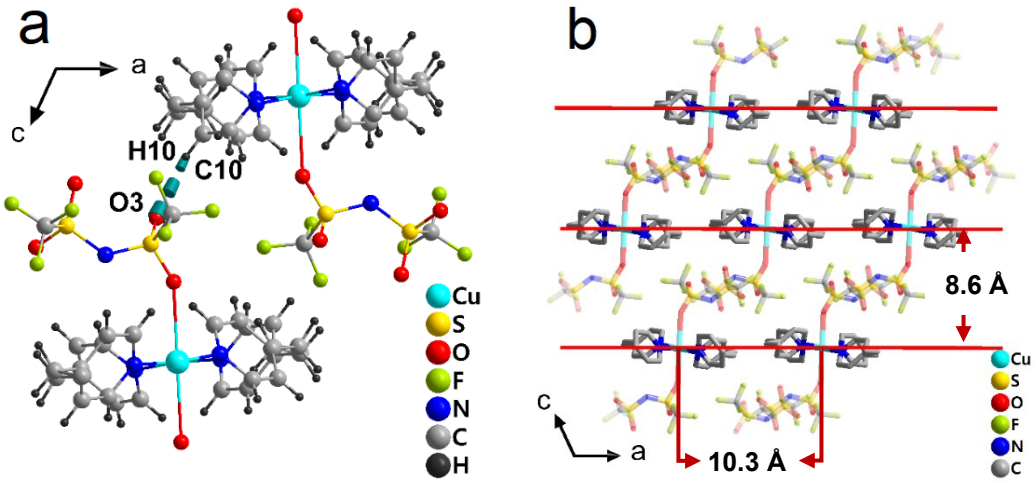

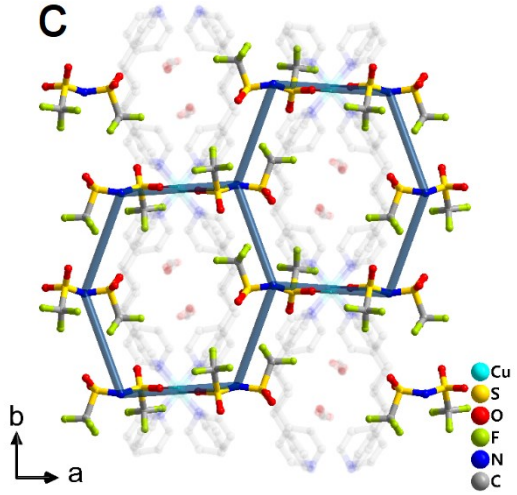

Fig. 2-9. Views of the crystal structure of **1**·CO_2. (a) View of the interchain interactions; (b) Packing structures of viewed along *b* axis; (c) Arrangement of NTf_2^- anions viewed along *c* axis

Interactions that exists between the 1D chains and CO_2 in **1**·2CO_2 are shown in Fig. 2-10. CO_2 molecules in **1**·2CO_2 are disordered over two sites with occupancies of 0.66 (molecule A) and 0.34 (molecule B). The shortest contact exists between a fluorine of one NTf_2^- anion and the carbon of CO_2 with F•••C distances of 2.95(2) (molecule A) and 2.68(5) Å (molecule B), which are shorter than the sum of their van der Waals radii (3.17 Å). On the other hand, the distance between oxygen of another NTf_2^- anion and the carbon of CO_2 in molecule B (O•••C = 3.28(5) Å) is slightly longer than the sum of their van der Waals radii (3.22 Å) and that in molecule A (O•••C =3.02(2) Å) is shorter. Considering that molecule A has a larger occupancy, it is expected that both fluorine and oxygen in the NTf_2^- anion should play prominent roles in governing CO_2 adsorption. Weak hydrogen bonding interactions also exist between the bpp ligand and CO_2 (H•••O and C•••O = 2.52(2) and 3.30(2) Å in molecule A and 2.58(4) and 3.34(4) Å in molecule B).

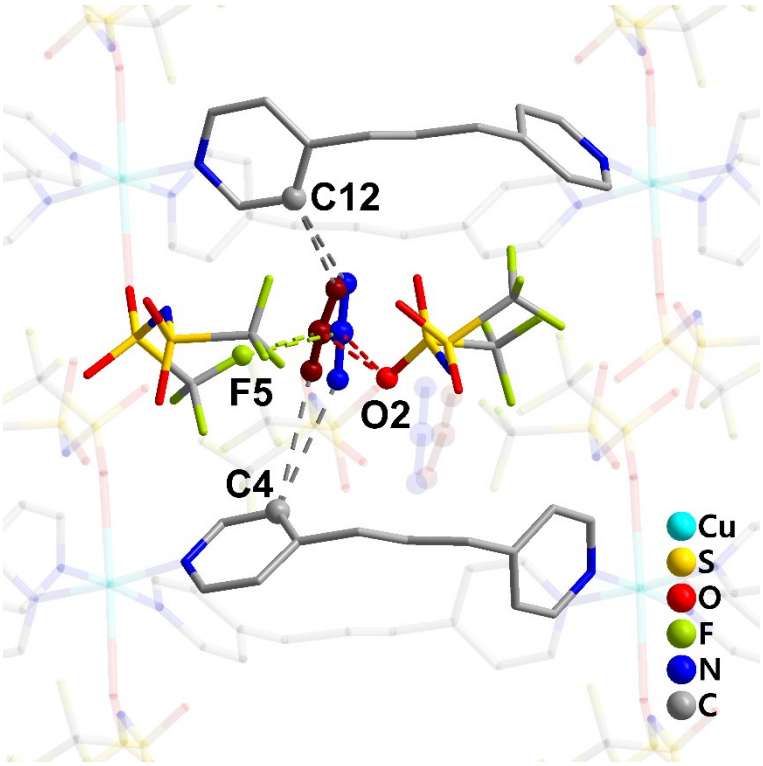

Fig. 2-10. View of the interactions between the CO_2 molecule (blue: molecule A, red: molecule B) and structural components in **1**·2CO_2.

The degree of quadrupole-quadrupole interactions between CO_2 molecules is related to the distances between carbons of two neighboring CO_2 molecules. In **1**·2CO_2, the respective distances between CO_2 carbons in molecules A and A, molecules A and B, and molecules B and B are 3.82(3) Å, 4.03(6) Å and 4.28(8) Å. Although the crystal structure of **1**·2CO_2 was determined at a temperature below the sublimation point of CO_2, the intermolecular C-C distances are longer than the intermolecular distance (3.58 Å) in solid CO_2.[22] Moreover, the C-C distance between CO_2 molecules in molecules B and B is greater than 4.1 Å, which is the intermolecular C-C distance in gaseous CO_2.[23] The differences in the intermolecular CO_2•••CO_2 distances show that a quadrupole-quadrupole interaction contributes little to stabilization of absorbed CO_2 in **1**·2CO_2 and, consequently, demonstrate that interactions with both a fluorine and oxygen atom in the NTf_2^- anion are the most influential in governing adsorption of CO_2 gas by **1**.

A density functional theory calculation was performed under periodic boundary conditions to gain more information about interactions occurring between NTf_2^- anions

and CO_2 in **1**·2CO_2. The binding energy (E_b) was determined by using the equation:

$$E_{\mathrm{b}} = E_{\mathrm{Framework+Gas}} - (E_{\mathrm{Framwork}} + E_{\mathrm{Gas}})$$

where $E_{\mathrm{Framework+gas}}$ and $E_{\mathrm{Framework}}$ are the respective energies of the complete complex **1**·2CO_2 and only the framework of **1**·2CO_2, and E_{Gas} is the energy of CO_2 in a sufficiently large super cell. The calculated E_b value was found to be –31.3 kJ·mol^{-1}, which is consistent with the experimentally determined enthalpy of CO_2 adsorption. Next, an analysis of the energy decomposition of **1**·2CO_2 was performed, utilizing a cluster model (Fig. 2-8) and an extended transition state method combined with the natural orbitals from chemical valence theory, in order to elucidate the nature of the interaction that most strongly contributes to CO_2 adsorption. The results (Table 2-1) show that the strongest interaction promoting stabilization of the structure of **1**·2CO_2 is associated with a dispersion force (–28.7 kJ mol^{-1}), an electrostatic interaction (–25.0 kJ mol^{-1}) contributes to a lesser extent, and orbital interaction energy (–13.3 kJ mol^{-1}) is a minor contributor.

Table 2-1. Energetic components of interaction energy (in kJ mol^{-1}) in the framework•••CO_2 model structure used for the ETS-NOCV analysis.

E_{pauli}	31.1
E_{elst}	-25.0
E_{orb}	-13.3
E_{disp}	-28.7
E_{int}	-35.9

This result is consistent with previous findings, which suggest that calculated Lewis acid-base binding energies between CO_2 and naked anions are inversely proportional to the solubility of CO_2 in ILs. Thus, Lewis acid-base interactions are not important contributors to solubilities of CO_2 in ILs.[24]

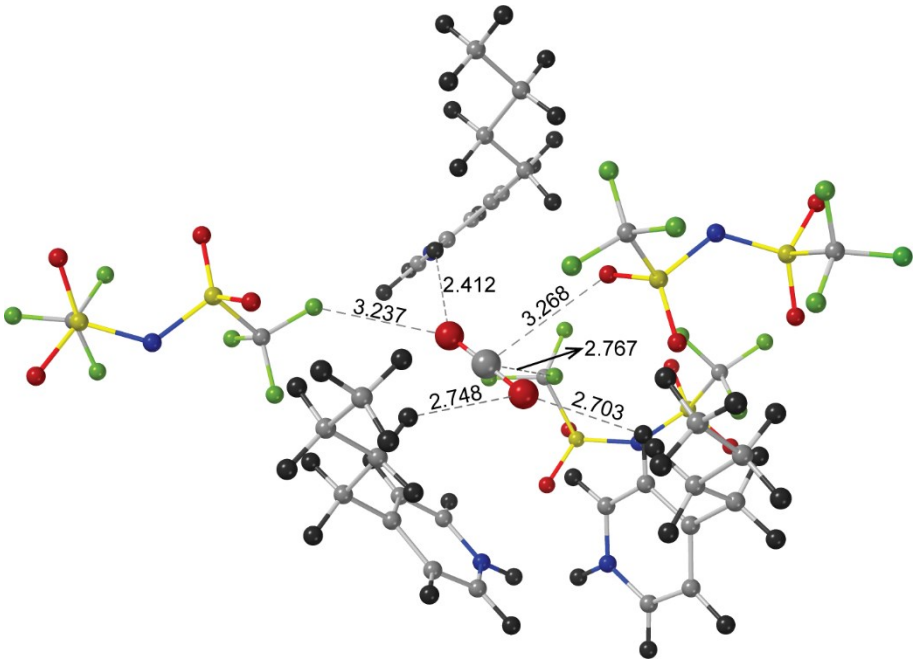

Fig.2-11. Model structure used for the energy decomposition analysis (ETS-NOCV). The values indicate the distances (Å) between neighboring atoms.

In Fig. 2-12 are displayed schematic views of the structures of soft crystal **1** formed during the CO_2 absorption process. Analysis of the structures before and after CO_2 absorption shows that the CO_2 absorption process by **1** has features that are similar to those of ILs. Firstly, **1** preferably absorbed CO_2 over other gases such as N_2 and Ar. Secondly, during absorption, the lattice of **1** expands to create an interstitial space for CO_2,[25] while the distance between the cation (in this case, copper) and anion (in this case, NTf_2^-) changes only slightly.[26] In addition, our studies have uncovered a unique feature not observed previously in studies of CO_2 absorption by ILs. Specifically, we obtained direct evidence showing that the NTf_2^- anion undergoes a conformational change from the *trans* to *cis* upon CO_2 binding. In ILs, the NTf_2^- anion can exist in two possible conformations (*trans* and *cis*) at room temperature with the *trans* form being thermodynamically more stable.[15,27] The reason why the conformation of the NTf_2^- anion changes when **1** absorbs CO_2 is that cohesion energy is enhanced owing to the larger dipole moment of the *cis* form (dipole moments for *trans* and *cis* forms are 0.2-0.4 and 4.4-5.4, respectively).[28] This enables the absorbed CO_2 molecule interact more strongly and cooperatively with the fluorine and oxygen atoms of the two neighboring

cis- NTf_2^- anions by taking full advantage of delocalized negative charges (Table 2-2), in the 1D alternate arrangement of •••NTf_2^-•••CO_2•••NTf_2^-•••CO_2•••.

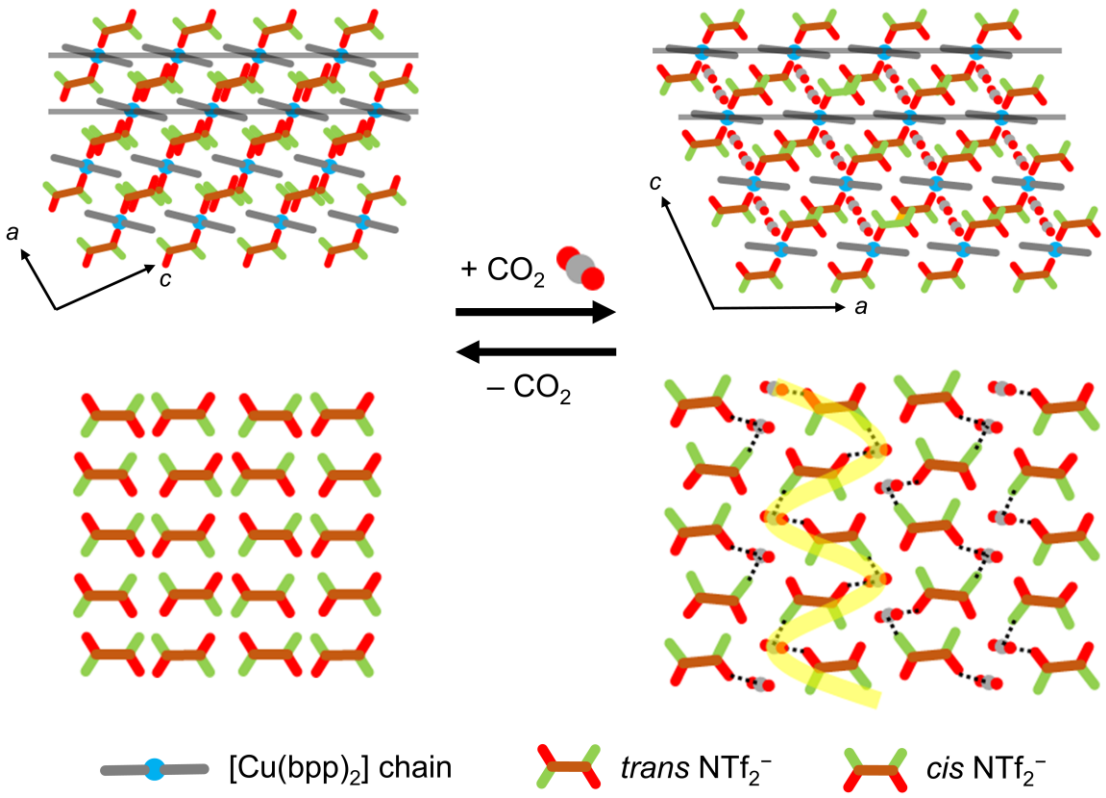

Fig. 2-12. Schematic views of structural changes occurring in the CO_2 absorption process by soft crystal **1**. The upper figures show packing structures viewed along the *b*-axis and bottom figures show arrangements of NTf_2^- anions in the presence and absence of CO_2. The 1D $[Cu(bpp)_2]$ chains are oriented along the *b*-axis. The dotted lines indicate intermolecular interactions between the NTf_2^- anion and CO_2. The yellow meandering line shows the 1D alternate arrangement of •••NTf_2^-•••CO_2•••NTf_2^- •••CO_2•••.

Gas absorption in association with a change between a closed structure and an open structure is dominated by a balance between the energy barrier for structural transition of an absorbent and the enthalpy associated with the open form of an absorbent absorbing a gas.[29,30] Regarding the former, fluorinated moieties contribute to decrease the energy barrier because their charge delocalization ability (Table 2-2) and fluorine's

low electronic polarizability weaken intermolecular interactions.[31] Regarding the latter, a fluorination of anions with Lewis base sites decreases their Lewis basicity, while this study revealed that Lewis acid-base interactions are not important contributors to solubilities of CO_2. Indeed, the most basic sites in anions are close to the most acidic sites in cations, preventing the formation of Lewis acid-base interactions between CO_2 and the most basic sites. The charge delocalization and low electric polarizability derived from a fluorination make impacts on an electrostatic interaction and a dispersion force, respectively, to interact with CO_2, though we still need more detailed investigation.

Table 2-2. Atomic charges obtained from the Bader analysis for NTf_2^- anions in the model structure with CO_2 constructed from the CO_2-absorbed phase (**1**·2CO_2). The atom numbering figures are shown in the bottom. Atomic charges in the similar model without CO_2 constructed from the desolvated phase (**1**) are shown in parentheses.

NTf_2^- in the model		
F1: -0.607 (-0.608)	F2: -0.605 (-0.618)	F3: -0.598 (-0.603)
F4: -0.610 (-0.600)	F5: -0.611 (-0.608)	F6: -0.616 (-0.584)
O3: -1.260 (-1.261)	O4: -1.267 (-1.281)	O5: -1.264 (-1.278)
O6: -1.260 (-1.285)	S1: +2.992 (+3.027)	S2: +3.014 (+3.053)
N1: -1.538 (-1.577)	C2: +1.670 (+1.645)	C3: +1.645 (+1.600)
F1′: -0.602 (-0.603)	F2′: -0.612 (-0.618)	F3′: -0.601 (-0.608)
F4′: -0.610 (-0.608)	F5′: -0.603 (-0.584)	F6′: -0.615 (-0.600)
O3′: -1.274 (-1.281)	O4′: -1.252 (-1.261)	O5′: -1.271 (-1.278)
O6′: -1.291 (-1.285)	S1′: +2.970 (+3.027)	S2′: +3.004 (+3.053)
N1′: -1.518 (-1.577)	C2′: +1.657 (+1.645)	C3′: +1.664 (+1.600)

2-3. Conclusions

Prior to the study described above, a lot of experiments and discussions has been conducted about the CO_2 absorption states in ILs.[7-12] In this effort, using the soft crystal **1** as a surrogate, we were able to visualize interactions that occur between the NTf_2^- anion component of ILs and CO_2. The pyridine rings in bpp ligands and NTf_2^- anions in **1** synergistically constrain CO_2 molecules in the crystal. The NTf_2^- anion contains the primary absorption sites for CO_2 comprised of a trifluoromethyl fluorine and sulfonyl oxygen atom. The bpp ligand supports the NTf_2^--CO_2 interaction through formation of a weak phenyl hydrogen-CO_2 interaction. As a result, a dispersion force and electrostatic interaction are the main contributors to stabilization of the CO_2-absorbed complex. Furthermore, a conformational change of the NTf_2^- anions from *trans* to *cis* occurring upon CO_2 capture by **1** also contributes to the absorption capacity. Of course, we understand that the observations made in this investigation have been made using a surrogate and not under real IL conditions especially because of differences in temperature and fluidity of the system. In addition, ILs with the NTf_2^- anion are not practical for application of CO_2 separation because the NTf_2^- anion with perfluorinated groups is not an environment-friendly. Nevertheless, the findings should not only increase the level of understanding of CO_2 absorption by ILs but also provide new approaches to probe interactions between ILs and CO_2 and to design new systems for applications of CO_2 separation.

2-4. Experimental Section

2-4-1. Materials

Commercially available reagents were used as received without further purification. $Cu(NTf_2)_2$ was synthesized using a previously described procedure.[28] $Cu(NMes_2)_2$ was synthesized by a reported procedure.[29]

2-4-2. Synthesis of $[Cu(NTf_2)_2(bpp)_2]$ (1) and $[Cu(NMes_2)_2(bpp)_2]$ (2)

A single-crystal **1** was prepared by using a diffusion method in the straight glass tube containing a bottom layer of 0.1 M aqueous $Cu(NTf_2)_2$, a middle layer of 1:1 water and MeOH, and a top layer of 0.2 M bpp in MeOH. After 1 week, the formed transparent and rod like purple single crystals were separated by filtration, washed with water, and dried in the atmosphere. Elemental analysis was used to confirm the atomic composition and purity of the as-synthesized single crystals. Elemental analysis (%) calcd for $C_{30}H_{28}Cu_1F_{12}N_6O_8S_4$: C 35.31, H 2.77, N 8.24, F 22.34, S 12.57. Found: C 34.86, H 2.57, N 8.04, F 22.77, S 12.69.

A single-crystal **2**·$3H_2O$ was prepared by using a solvent evaporation method in the beaker containing 0.1 M aqueous $Cu(NMes_2)_2$ and 0.2 M bpp in MeOH. After 1 week, the formed transparent and plate like blue single crystals were separated by filtration. Elemental analysis was used to confirm the atomic composition and purity of the as-synthesized single crystals. Elemental analysis (%) calcd for $C_{30}H_{46}CuN_6O_{11}S_4$: C 41.97, H 5.40, N 9.79. Found: C 42.47, H 4.91, N 9.78.

2-4-3. Single-crystal X-ray diffraction analysis of 1, 1·$2CO_2$, 2·$3H_2O$ and 2.

Crystal data for **1** were collected at 173 K on a RIGAKU RAXIS-RAPID imaging-imaging diffractometer with a graphite-monochromated Mo-Kα radiation (λ = 0.71075 Å). Crystal data for **2·3H₂O** and **2** were collected at 293 K on a RIGAKU XtaLab Synergy-R with a graphite-monochromated Mo-Kα radiation (λ = 0.71075 Å). The structure was solved by using direct method (SHELXT)[30] and refined by using full-matrix least-squares techniques on F^2 using SHELXL-2018 (ver. 2018/3).[31] All non-

hydrogen atoms were refined anisotropically. Hydrogen atoms were located at geometrically calculated positions and refined using a riding model. Olex2 was used as a graphical user interface.[32] Crystallographic data are shown in Table 2-3 and 2-4.

The structural determination of **1**·2CO_2 was carried out using the following procedure. A single crystal of **1** was placed at the bottom of a glass capillary, which was then adhered to the base using glue. The base was installed on the adsorption equipment (BELSORP-mini, MicrotracBEL Corp.) and the crystal was heated at 373 K for 30 min under a vacuum as the pre-treatment. After pre-treatment, CO_2 gas at 40 kPa was added and the capillary was cut and sealed quickly. The capillary containing single crystal sample and CO_2 gas was placed in the single-crystal X-ray diffractometer with a cryogenic unit, and cooled at a rate of 1 K min^{-1} from 293 K to 173 K, and then held at 173 K for 4 h. X-ray diffraction measurements were then made at 173 K on a RIGAKU XtaLAB P200 with a multi-mirror monochromated Cu-Kα radiation (λ = 1.5418 Å). Data analysis was performed in the manner described for **1**. Crystallographic data are shown in Table 2-3.

Table 2-3. The crystallographic data of the crystals **1** and **1·CO₂**

	1	**1·2CO₂**
Chemical formula	$[Cu(NTf_2)_2(bpp)_2]$	$\{[Cu(NTf_2)_2(bpp)_2]\cdot 2CO_2\}$
Empirical formula	$C_{30}H_{28}CuF_{12}N_6O_8S_4$	$C_{32}H_{28}CuF_{12}N_6O_{12}S_4$
Formula weight	1020.36	1108.38
Crystal system	Monoclinic	Monoclinic
Space group	*P*2/*n*	*C*2/*c*
Temperature / K	173	173
a / Å	9.7230(9)	20.5810(6)
b / Å	12.1946(10)	12.3407(2)
c / Å	17.1072(14)	18.9377(6)
α / °	90	90
β / °	96.176(3)	114.545(4)
γ / °	90	90
V / Å^3	2016.6(3)	4375.2(2)
Z	2	4
GOF on F^2	1.102	1.280
R_1 [$I > 2\sigma(I)$][a]	0.0579	0.0823
R_w [$I > 2\sigma(I)$][b]	0.1530	0.2665

[a] $R_1 = \sum||F_o| - |F_c||/\sum|F_o|$. [b] $R_w = [(\sum w(|F_o|^2 - |F_c|^2)^2)/\sum w(F_o^2)^2]^{1/2}$.

Table 2-4. The crystallographic data of the crystals **2**·3H_2O and **2**

	2·3H_2O	**2**
Chemical Formula	{[Cu(NMes$_2$)$_2$(bpp)$_2$]·3H_2O}	[Cu(NMes$_2$)$_2$(bpp)$_2$]
Formula	$C_{30}H_{46}CuN_6O_{11}S_4$	$C_{30}H_{40}CuN_6O_8S_4$
Formula weight	858.53	804.48
Crystal system	Triclinic	Monoclinic
Space group	*P*-1	$P2_1/c$
Temperature / K	293	293
a / Å	9.1281(4)	9.7086(8)
b / Å	11.0414(4)	17.8811(11)
c / Å	11.1340(4)	11.4903(7)
α / °	117.748(4)	90
β / °	100.600(4)	109.910(8)
γ / °	98.482(3)	90
V / Å^3	940.46(8)	1875.5(2)
Z	1	2
GOF on F^2	1.027	1.282
R_1 [$I > 2\sigma(I)$][a]	0.0606	0.1282
R_w [$I > 2\sigma(I)$][b]	0.1779	0.2813

[a] $R_1 = \sum||F_o| - |F_c||/\sum|F_o|$. [b] $R_w = [(\sum w(|F_o|^2 - |F_c|^2)^2)/\sum w(F_o^2)^2]^{1/2}$.

2-4-4. Gas adsorption isotherm experiments.

CO_2 (195 K), N_2 (77 K and 195 K) and Ar (77 K and 195 K) adsorption/desorption isotherms were measured by using a BELSORP-max (MicrotracBEL Corp.). Water adsorption/desorption isotherms were measured at 298 K by using a BELSORP-aqua (MicrotracBEL Corp.). Before the measurement, the sample was heated at 373 K in a vacuum for 20 h for activation by BELPREP-vac (MicrotracBEL Corp.). High-pressure CO_2 adsorption/desorption isotherms were measured by using a BELSORP-HP

(MicrotracBEL Corp.). Activation of the sample was performed on a BELSORP-HP at 373 K in a vacuum.

2-4-5. Theoretical calculations.

For determining the S-N bond rotational barrier in NTf_2^-, relax scan calculations were performed using gaussian 09 Rev. E.01 software at the B3LYP/aug-cc-pVDZ level of theory.[36] A PBE functional,[37] with projector augmented wave potentials and van der Waals interaction corrected by using a D3 scheme[38] to optimize the atomic positions of **1**, CO_2 and **1**·2CO_2, was used to obtain an estimate of the binding energy of CO_2. In all cases, spin polarized calculations were employed under periodic boundary condition and Γ-point approximation using the Vienna Ab initio Simulation Package (VASP)[39-42] with the cut-off energy of 400 eV. The atomic charges were evaluated based on Bader analysis.[43-46] Similarly to other reported approaches,[47-49] after optimization of **1**·2CO_2, a model consisting of one CO_2, three NTf_2^- and three (4-pyridyl)butane, which are protonated instead of bonded to Cu^{2+} (Supplementary Fig. S12), was employed to investigate the nature of the interaction between CO_2 and **1**. The positions of added H atoms were optimized with a PBE functional using Amsterdam Density Functional 2018 program.[50] A standard triple-ζ STO basis set with two sets of polarization functions (TZ2P)[51] and a Grimme D3 type dispersion correction were applied to all atoms in the model. The model structure was optimized by using the extended transition state method[52] combined with the natural orbitals for chemical valence theory[53,54] with the same level of theory as that used for optimization of H atoms.

2-5. References

1. K.R. Seddon, Ionic liquids for clean technology. *J. Chem. Technol. Biotechnol*. **1997**, *68*, 351.
2. D. Zhao, *et al.*, Ionic liquids: applications in catalysis. *Catal. Today* **2002**, *74*, 157.
3. N. V. Plechkova & K. R. Seddon, Applications of ionic liquids in the chemical industry. *Chem. Soc. Rev.* **2008**, *37*, 123.
4. Z. Lei, *et al.*, Gas Solubility in Ionic Liquids. *Chem. Rev.* **114**, 1289-1326(2014).
5. J. M. Pringle, *et al.*, The effect of anion fluorination in ionic liquids-physical properties of a range of bis(methanesulfonyl)amide salts. *New J. Chem.* **2003**, *27*, 1504.
6. J. L. Anthony, *et al.*, Anion Effects on Gas Solubility in Ionic Liquids. *J. Phys. Chem. B* **2005**, *109*, 6366.
7. S. P. Kelley, *et al.*, Understanding Carbon Dioxide Solubility in Ionic Liquids by Exploring the Link with Liquid Clathrate Formation. *Chem. Eur. J.* **2017**, *23*, 14332.
8. S. S. Rao & S. P. Gejji, CO_2 Adsorption Using Fluorine Functionalized Ionic Liquids: Interplay of Hydrogen and σ-Hole Interactions. *J. Phys. Chem. A* **2016**, *120*, 1243.
9. G. B. Damas, *et al.*, A Quantum Chemistry Study for Ionic Liquids Applied to Gas Capture and Separation. *J. Phys. Chem. B* **2014**, *118*, 9046.
10. M. Ramdin, *et al.*, State-of-the-Art of CO_2 Capture with Ionic Liquids. *Ind. Eng. Chem. Res.* **2012**, *51*, 8149.
11. Y. F. Hu, *et al.*, The molecular characteristics dominating the solubility of gases in ionic liquids. *Chem. Soc. Rev.* **2011**, *40*, 3802.
12. T. C. Lourenço, *et al.*, Insights on the Solubility of CO_2 in 1-Ethyl-3-methylimidazolium Bis(trifluoromethylsulfonyl)imide from the Microscopic Point of View. *Environ. Sci. Technol.* **2013**, *47*, 7421.
13. S. Horike, *et al.*, Soft porous crystals. *Nature Chem.* **2009**, *1*, 695.

14. M. Kato, *et al*., Soft Crystals: Flexible Response Systems with High Structural Order. *Chem. Eur. J.* **2019**, *25*, 5105.

15. J. C. Lassègues, *et al.*, Raman and ab initio study of the conformational isomerism in the 1-ethyl-3-methyl-imidazolium bis(trifluoromethanesulfonyl)imide ionic liquid. *J. Raman Spectrosc.* **2007**, *38*, 551.

16. R. Kitaura, *et al.*, Porous coordination-polymer crystals with gated channels specific for supercritical gases. *Angew. Chem., Int. Ed.* **2003**, *42*, 428.

17. S. N. V. K. Aki, *et al.*, High-Pressure Phase Behavior of Carbon Dioxide with Imidazolium-Based Ionic Liquids. *J. Phys. Chem. B* **2004**, *108*, 20355.

18. H.-J. Song, *et al.*, Simplified Estimation of Regeneration Energy of 30 wt % Sodium Glycinate Solution for Carbon Dioxide Adsorption. *Ind Eng Chem Res.* **2008**, *47*, 9925.

19. W. Lu, *et al.*, Cost-Effective Synthesis of Amine-Tethered Porous Materials for Carbon Capture. *Chemsuschem* **2014**, *8*, 410.

20. J. A. Dunne, *et al.*, Calorimetric Heats of Adsorption and Adsorption Isotherms. 1. O_2, N_2, Ar, CO_2, CH_4, C_2H_6, and SF_6 on Silicalite. *Langmuir* **1996**, *12*, 5888.

21. B. Dębski, *et al.*, Thermodynamic interpretation and prediction of CO_2 solubility in imidazolium ionic liquids based on regular solution theory. *J. Mol. Liq.* **2019**, *291*, 110477.

22. N. Brigot, *et al.*, The structure of the carbon dioxide dimer. *Chem. Phys. Lett.* **1977**, *49*, 157.

23. L. Mannik, *et al.*, An Infrared Spectrum of CO_2 Dimers in the "Locked" Configuration. *Can. J. Phys.* **1971**, *49*, 3056.

24. B. Bhargava & S. Balasubramanian, Probing anion–carbon dioxide interactions in room temperature ionic liquids: Gas phase cluster calculations. *Chem Phys. Lett.* **2007**, *44*, 242.

25. R. Babarao, *et al.*, Understanding the High Solubility of CO_2 in an Ionic Liquid with the Tetracyanoborate Anion. *J. Phys. Chem. B* **2011**, *115*, 32, 9789.

26. T. C. Lourenço, *et al.*, Local environment structure and dynamics of CO_2 in the

1-ethyl-3-methylimidazolium bis(trifluoromethanesulfonyl)imide and related ionic liquids. *J. Chem. Phys.* **2017**, *146*, 104502.

27. K. Fujii, *et al.*, Conformational Equilibrium of Bis(trifluoromethanesulfonyl) Imide Anion of a Room-Temperature Ionic Liquid: Raman Spectroscopic Study and DFT Calculations. *J. Phys. Chem. B* **2006**, *110*, 8179.
28. T. V. Hoogerstraete, *et al.*, Crystal structures of low-melting ionic transition-metal complexes with N-alkylimidazole ligands. *CrystEngComm*. **2012**, *14*, 4902.
29. Numaguchi, R. et al. Molecular simulation of capillary phase transitions in flexible porous materials. *J. Chem. Phys.* **2013**, *138*, 054708.
30. Gurkan, B. et al. Molecular Design of High Capacity, Low Viscosity, Chemically Tunable Ionic Liquids for CO_2 Capture. *J. Phys. Chem. Lett.* **2010**, *1*, 3494.
31. Noro, S. et al. Controlling the gate-sorption properties of solid solutions of Werner complexes by varying component ratios. *Dalton Trans.* **2020**, *49*, 9438.
32. D. Henschel, et al. Metall(II)-dimethylamid-Tetrahydrate: Das Dimethylamin-Anion als einzähniger O-Ligand und tetrafunktioneller Wasserstoffbrucken-Akzeptor in den isotypen Komplexen $[M(H_2O)_4\{(CH_3SO_2)_2N\}_2]$ mit M = Magnesium, Nickel, Kupferund Zink, *Z. anorg. Allg. Chem.* **1996**, *622*, 1065
33. G. M. Sheldrick, SHELXT–Integrated space-group and crystal-structure determination. *Acta Cryst.* **2015**, *A71*, 3.
34. G. M. Sheldrick, Crystal structure refinement with SHELXL. *Acta Cryst.* **2015**, *C71*, 3.
35. O.V. Dolomanov, *et al.*, OLEX2: a complete structure solution, refinement and analysis program. *J. Appl. Cryst.* **2009**, *42*, 339.
36. Frisch, M. J. et al. Gaussian 09, Revision E.01, Gaussian, Inc., Wallingford CT 2009.
37. Perdew, J. P. et al. Generalized Gradient Approximation Made Simple. *Phys. Rev. Lett.* **1996**, *77*, 3865.
38. Grimme, S. et al. A consistent and accurate ab initio parametrization of density functional dispersion correction (DFT-D) for the 94 elements H-Pu. *J. Chem.*

Phys. **2010**, *132*, 154104.

39. Kresse, G. & Hafner, J. Ab initio molecular dynamics for liquid metals. Phys. Rev. B **1993**, *47*, 558.

40. Kresse, G. & Hafner, J. Ab initio molecular-dynamics simulation of the liquid-metal–amorphous-semiconductor transition in germanium. Phys. Rev. B **1994**, *49*, 14251.

41. Kresse, G. & Furthmüller, J. Efficiency of ab-initio total energy calculations for metals and semiconductors using a plane-wave basis set. *J. Comput. Mat. Sci.* **1996**, *6*, 15.

42. Kresse, G. & Furthmüller, J. Efficient iterative schemes for ab initio total-energy calculations using a plane-wave basis set. *Phys. Rev. B* **1996**, *54*, 11169.

43. Tang, W. et al. A grid-based Bader analysis algorithm without lattice bias. *J. Phys.: Condens. Matter* **2009**, *21*, 084204.

44. Sanville, E. Improved grid-based algorithm for Bader charge allocation. *J. Comp. Chem.* **2007**, *28*, 899.

45. Henkelman, G. A. et al. A fast and robust algorithm for Bader decomposition of charge density. *Comput. Mater. Sci.* **2006**, *36*, 354.

46. Yu, M. & Trinkle, D. R. Accurate and efficient algorithm for Bader charge integration. *J. Chem. Phys.* **2011**, *134*, 064111.

47. Sillar, K. et al. Ab Initio Study of Hydrogen Adsorption in MOF-5. *J. Am. Chem. Soc.* **2009**, *131*, 4143.

48. Valenzano, L. et al. Heats of Adsorption of CO and CO_2 in Metal–Organic Frameworks: Quantum Mechanical Study of CPO-27-M (M = Mg, Ni, Zn). *J. Phys. chem. C* **2011**, *15*, 21777.

49. Simpson, S. et al. Modulating Bond Lengths via Backdonation: A First-Principles Investigation of a Quinonoid Zwitterion Adsorbed to Coinage Metal Surfaces. *J. Phys. Chem. C* **2016**, *120*, 6633.

50. Velde, G. T. et al. Chemistry with ADF. *J. Comput. Chem.* **2001**, *22*, 931.

51. Lenthe, E. V. et al. Relativistic regular two-component Hamiltonians. *Int J*

Quantum Chem. **1996**, *57*, 281.

52. Ziegler, T. & Rauk, A. On the calculation of bonding energies by the Hartree Fock Slater method. *Theor. Chim. Acta.* **1977**, *46*, 1.

53. Michalak, A. et al. Bond Orbitals from Chemical Valence Theory. *J. Phys. Chem. A* **2008**, *112*, 1933.

54. Mitoraj, M. & Michalak, A. Natural orbitals for chemical valence as descriptors of chemical bonding in transition metal complexes. *J. Mol. Model.* **2007**, *13*, 347.

Chapter 3

Effect of uptake/release of coordinated molecules on gate-opening adsorption behavior in coordination polymer

Abstract

Gate-opening adsorption behavior of guest molecules is one of interesting properties in flexible CPs. In CPs that exhibit gate-adsorption behaviors, a rapid increase in an adsorption amount is observed when a pressure crosses the threshold and this threshold pressure is called a gate pressure. In this work, I investigated the effect of uptake/release of guest molecules on gate-adsorption behaviors using the one-dimensional flexible CP, $[Cu(NTf_2)_2(bpp)_2]$ (**1**), which shows the typical gate adsorption behavior for CO_2. Although the Cu(II) ion in **1** is hexa-coordinated by four bpp ligands and two NTf_2^- anions, the NTf_2^- anions are weakly constrained by the Cu(II) ion. Therefore, coordinated organic molecules, acetonitrile (MeCN), dimethyl sulfoxide (DMSO) and *N,N*-dimethylformamide (DMF), can coordinate to Cu(II) ions instead of the NTf_2^- anions when **1** is exposed to their vapors. After removing coordinated guest molecules, the skeleton disorder is observed from the powder XRD data. CO_2 adsorption/desorption isotherms for **1** are affected after uptake and release of coordinated molecules, and gate pressure is significantly reduced while they keep almost the same adsorption amount for CO_2. I successfully lowered the gate pressure by this strategy, and it will broaden the potential applications of **1** for gas separation.

3-1. Introduction

Different from traditional porous materials such as activated carbons and zeolites, coordination polymers (CPs) often possess flexible frameworks, which exhibit unique adsorption properties for different kinds of gas.[1-4] Gate-adsorption behaviors were observed in many flexible CPs.[5-9] The adsorption amounts of CPs with gate-adsorption behaviors suddenly increased after reaching a specific pressure that is called a gate pressure (P_g), but after getting over P_g, rapid increases in adsorption amounts are observed because the structures of CPs convert from a dense closed phase to an open porous phase or from a small porous phase to a large porous phase to accept more guest molecules.[10] CPs with gate-adsorption behaviors are considered for selective gas adsorption[11] and gas detection.[12]

Although a lot of CPs with gate-adsorption behaviors are reported, controlling this unique phenomenon is still a challenging issue, especially lowering the gate pressure P_g, because practical applications prefer low operation pressure to save operation costs. Cheng et al. treated the flexible two-dimensional (2D) CP, $[Cu(BF_4)_2(4,4'\text{-bpy})_2]$ (ELM-11), in which 4,4′-bpy is 4,4′-bipyridine, with alcohols and successfully lowered its P_g of CO_2 adsorption.[13] However, the CO_2 adsorption amount of ELM-11 treated by this method decrease by more than 10 % because partial introduced alcohol molecules remained in the framework to disturb the original host-guest interaction. Miura et al. synthesized a series of $[Ni_2(2,6\text{-ndc})_2\text{dabco}]$ (2,6-ndc = 2,6-naphthalenedicarboxylate, dabco = 1,4-diazabicyclo[2.2.2]octane) with different crystalline sizes by micromixer-based synthesis and found that the crystallite size influenced P_g.[12] When the crystalline size is larger than 1000 nm, the gate opening behavior becomes obvious with increase in the crystallite size, and when crystalline size is smaller than 500 nm, gate-adsorption behavior disappeared.

In this chapter, to achieve lowering P_g of CPs without any loss of adsorption amount, I tried to disturb the arrangement of NTf_2^- anions and the one-dimensional (1D) chain structures from ordered to disordered in $[Cu(NTf_2)_2(bpp)_2]$ (**1**) by uptake/release of coordinated guest molecules. Effective CO_2 adsorption sites have been discussed in

chapter 2, that trifluoromethyl fluorine and sulfonyl oxygen atoms of NTf_2^- anions and pyridine rings of bpp ligands showed weak interaction for CO_2 adsorption in **1**. Here, a slight structural disorder of NTf_2^- anions and 1D $Cu(bpp)_2$ chains may contribute to weaken the inter-chain interactions in **1**, resulting in for lowering P_g for CO_2.

3-2. Results and discussion

Three kinds of coordinated neutral guest molecules, acetonitrile (MeCN), dimethyl sulfoxide (DMSO) and *N,N*-dimethylformamide (DMF) were adopted for the purpose in this chapter. First, guest-coordinated CPs, {[Cu(bpp)$_2$(G)]·2NTf$_2$} (**1**·G (G = MeCN, DMSO, and DMF)), were directly synthesized and crystallographically characterized. All CPs have the similar 1D doubly linked chain structure to **1** without any guest molecules. One copper ion coordinates with four bpp ligands and one guest molecule as shown in Fig. 3-1. The distances between the copper ions and bpp ligands (2.020(8) ~ 2.040(8) Å) are shorter than those between the copper ions and coordinated guest molecules (2.246(6), 2.211(7), and 2.165(3) Å for **1**·MeCN, **1**·DMSO, and **1**·DMF, respectively). There are two kinds of NTf_2^- anions in each CP and both of them are in *trans* conformation. One NTf_2^- anion is located near the copper ion but their Cu•••O distances are too long (3.790(6), 4.037(9), and 4.226(3) Å for **1**·MeCN, **1**·DMSO, and **1**·DMF, respectively) to form coordinative interactions. However, weak hydrogen bonding interactions between pyridine ring of bpp ligands and sulfonyl oxygen atoms of NTf_2^- anions are observed. The O•••N distances between NTf_2^- anions and pyridine rings were 3.076(8), 3.08(1) and 3.156(4) Å for **1**·MeCN, **1**·DMSO, and **1**·DMF, respectively, and the O•••H•••C angles are 111.8(3)°, 105.0(4)° and 104.2(2)° for **1**·MeCN, **1**·DMSO, and **1**·DMF, respectively. Another kind of NTf_2^- anion is highly disordered and no intermolecular interaction is found between these anions and the 1D chains.

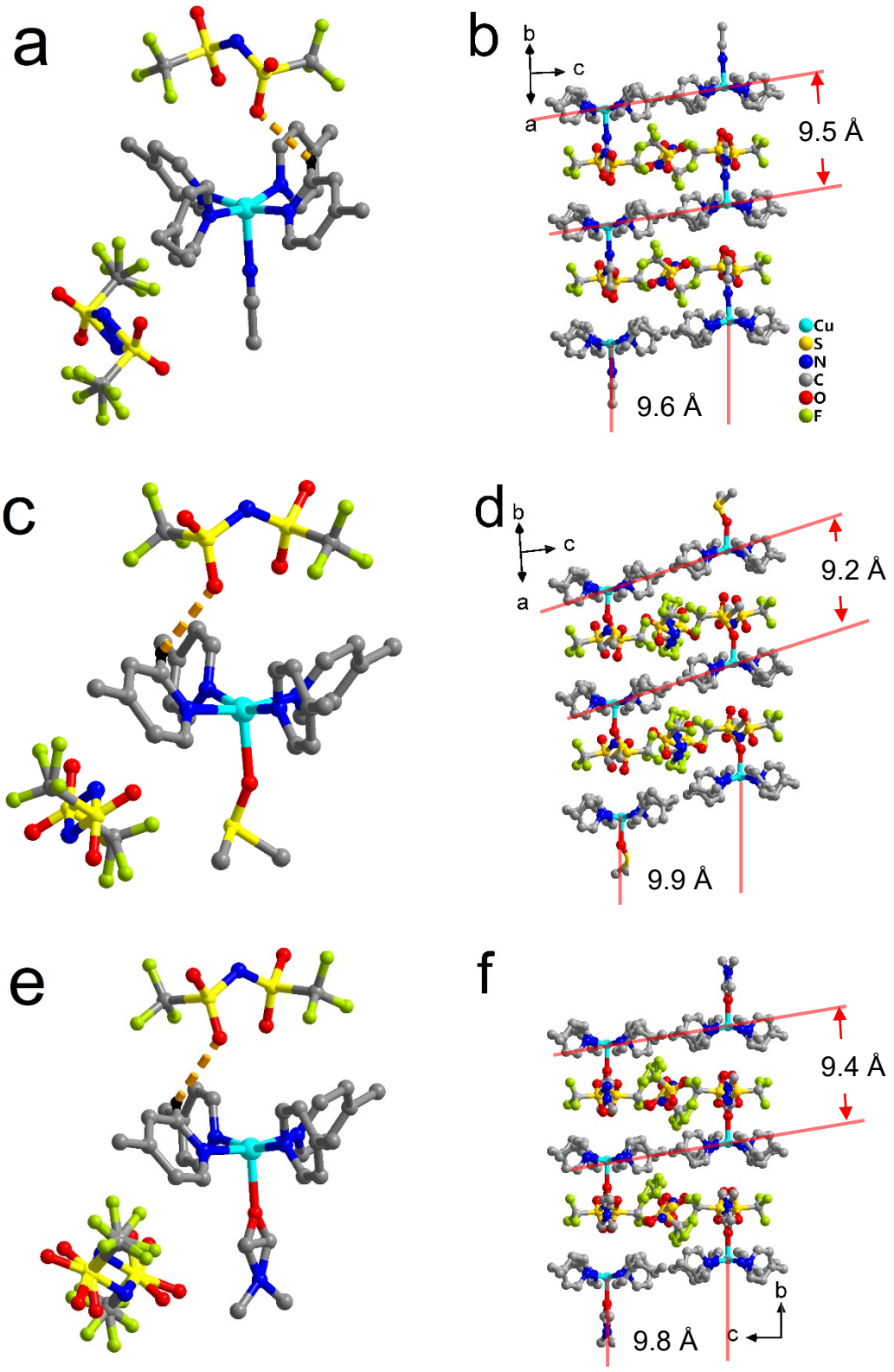

Fig. 3-1. Coordination environment around the Cu center and view of the weak hydrogen bonding interaction in (a) **1**·MeCN, (b) **1**·DMSO, and (c) **1**·DMF. Packing structures of one-dimensional chains in (d) **1**·MeCN, (e) **1**·DMSO, and (f) **1**·DMF.

The 1D chains of **1**·MeCN, **1**·DMSO and **1**·DMF aggregate through weak CH/π interactions to form quasi 2D layers with the interchain distances of 9.6 Å, 9.9 Å and 9.8 Å, respectively (Fig. 3-1), near 9.9 Å in **1**. In addition, NTf_2^- anions are sandwiched between the quasi 2D layers through weak hydrogen bonding interactions, in which the distances between two neighboring layers are 9.5 Å, 9.2 Å and 9.4 Å, respectively, much longer than 8.0 Å in **1**. Therefore, the introduction of coordinated solvent molecules significantly enlarges the distances between the quasi 2D layers.

To find appropriate temperatures, at which coordinated guest molecules are completely removed, the TG measurements were performed. The TG curves indicate that all CPs are stable until 500 K as shown in Fig. 3-2(a). The removal of guest molecules was then performed by heating the as-synthesized **1**·G at 373, 423, and 423 K for **1**·MeCN, **1**·DMSO and **1**·DMF, respectively, under vacuum. Hereafter, the heated samples are denoted as "heated **1**·G". The TG curves of the heated **1**·G indicate that there is no weight loss corresponding to the release of coordinated guest molecules (Fig. 3-2(b)), implying the complete removal of guests.

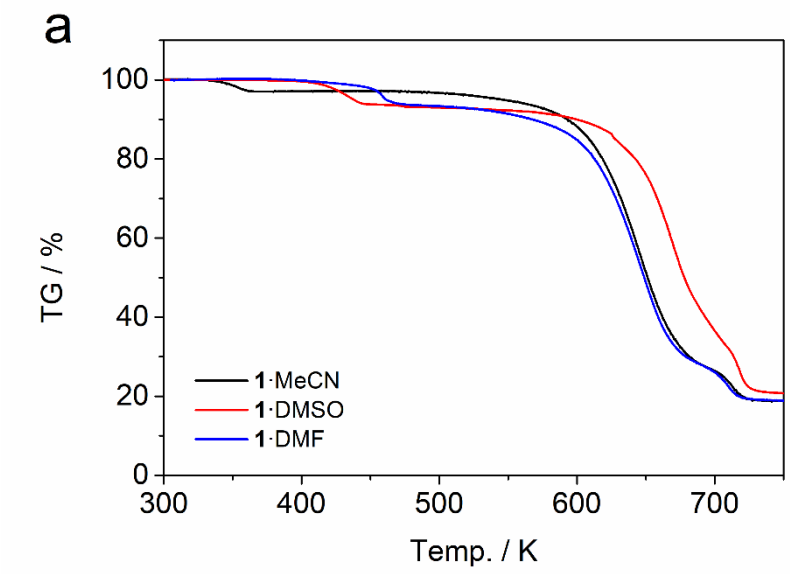

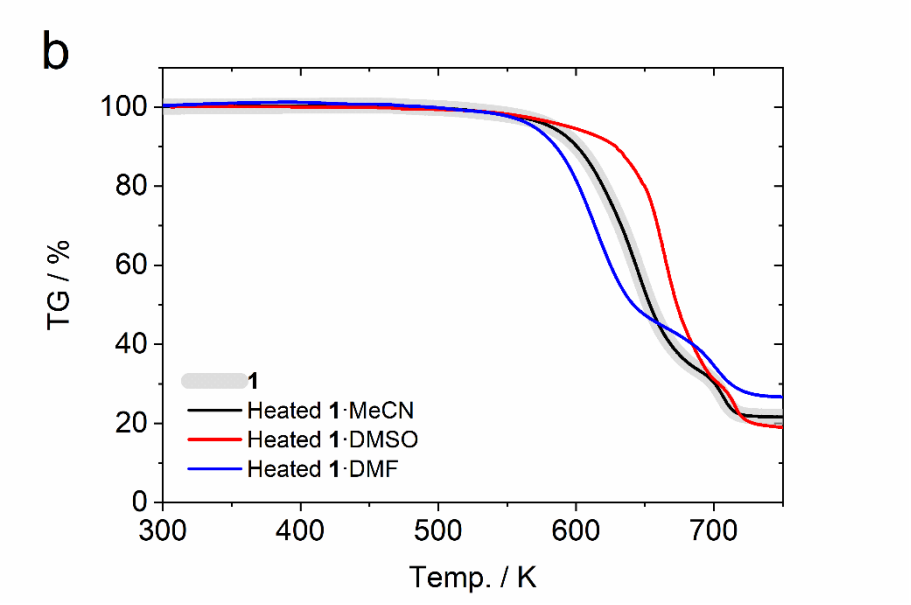

Fig. 3-2. TG curves of (a) as-synthesized **1**·MeCN, **1**·DMSO, and **1**·DMF, and (b) heated **1**·MeCN, **1**·DMSO, and **1**·DMF.

IR spectra of as-synthesized **1**, **1**·G, and heated **1**·G are shown in Fig. 3-3. The bands at 2274, 1020, and 1652 cm^{-1} observed in **1**·MeCN, **1**·DMSO, and **1**·DMF are assigned to the C-N vibration bands of MeCN nitrile group, the symmetric S-O vibration band of DMSO sulfonyl group, and the symmetric C-O vibration band of DMF amide group, respectively, and these peaks disappear after heating, indicating the complete removal of coordinated guest molecules. The positions of all IR bands including the asymmetric (1317 and 1354 cm^{-1}) and symmetric (1132 cm^{-1}) vibration bands of NTf_2^- sulfonyl group in all heated **1**·G are very similar with those in as-synthesized **1**, indicating that NTf_2^- anions in the heated **1**·G should weakly coordinate to copper ions as same as as-synthesized **1**, which is confirmed by a single-crystal XRD analysis.

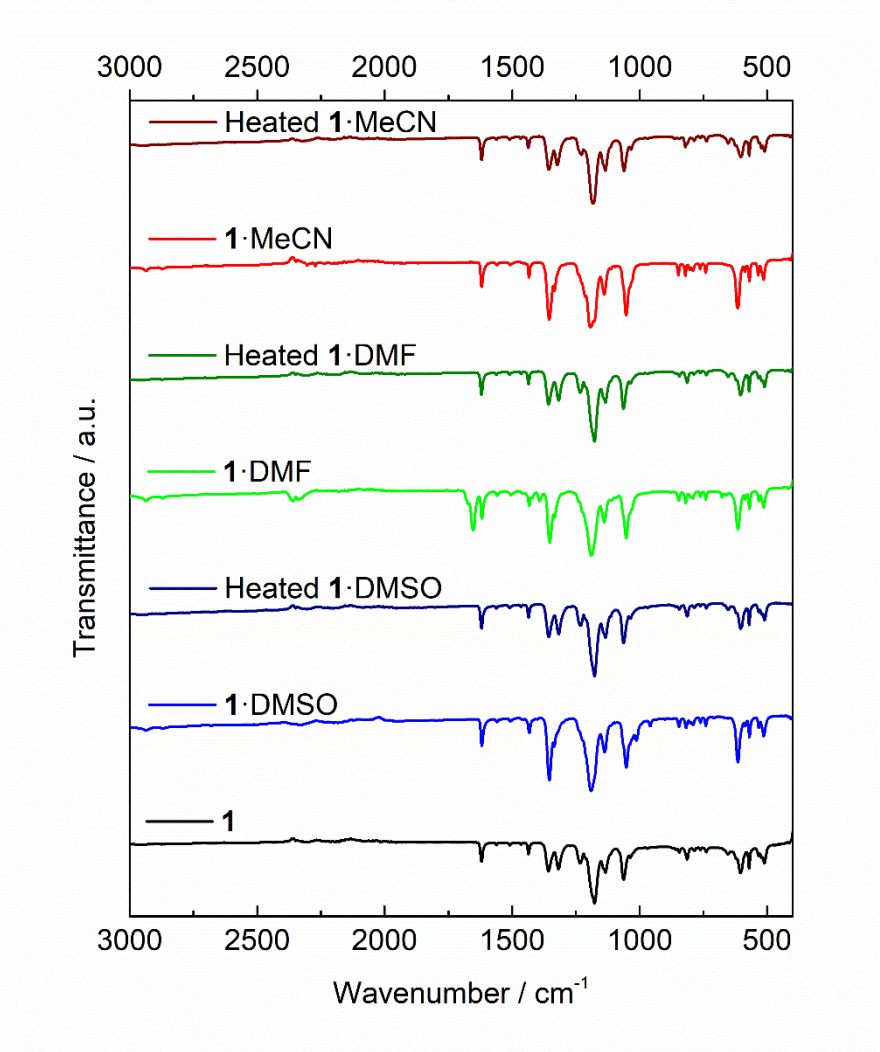

Fig. 3-3. IR spectra of as-synthesized **1**, **1**·MeCN, **1**·DMSO, **1**·DMF, and heated **1**·MeCN, **1**·DMSO, and **1**·DMF.

The powder X-ray diffraction (PXRD) patterns of as-synthesized **1**, **1**·MeCN, **1**·DMSO, **1**·DMF, and heated **1**·G are shown in Fig. 3-4. After removing coordinated guest molecules, the diffraction peaks are broadened. There are two possible reasons for the peak broadening: one is a decrease in a crystallinity and the other is a decrease in a crystallite size. In addition to the peak broadening, the overall PXRD patterns of heated **1**·G are slightly different from that of as-synthesized **1**, suggesting that heated **1**·G has slightly different one-dimensional and/or packing structures from as-synthesized **1**. There are three characteristic diffraction peaks at 7.1°, 10.1° and 21.7° corresponding to (010), (10-1) and (202) planes of crystal structure of CP **1** as shown

in Fig. 3-4(a). The (10-1) plane represents the plane built by neighboring one-dimensional chains in different quasi 2D layers, and the similar peaks are observed in heated **1**.At the same time, the (202) plane represents the quasi 2D layers constructed from 1D chains. The similar peaks were also observed in in heated **1**·G, at the same time, (010) plane represents the plane constructed by neighboring copper ions of one-dimensional chains, became very obscure in heated **1**·G.

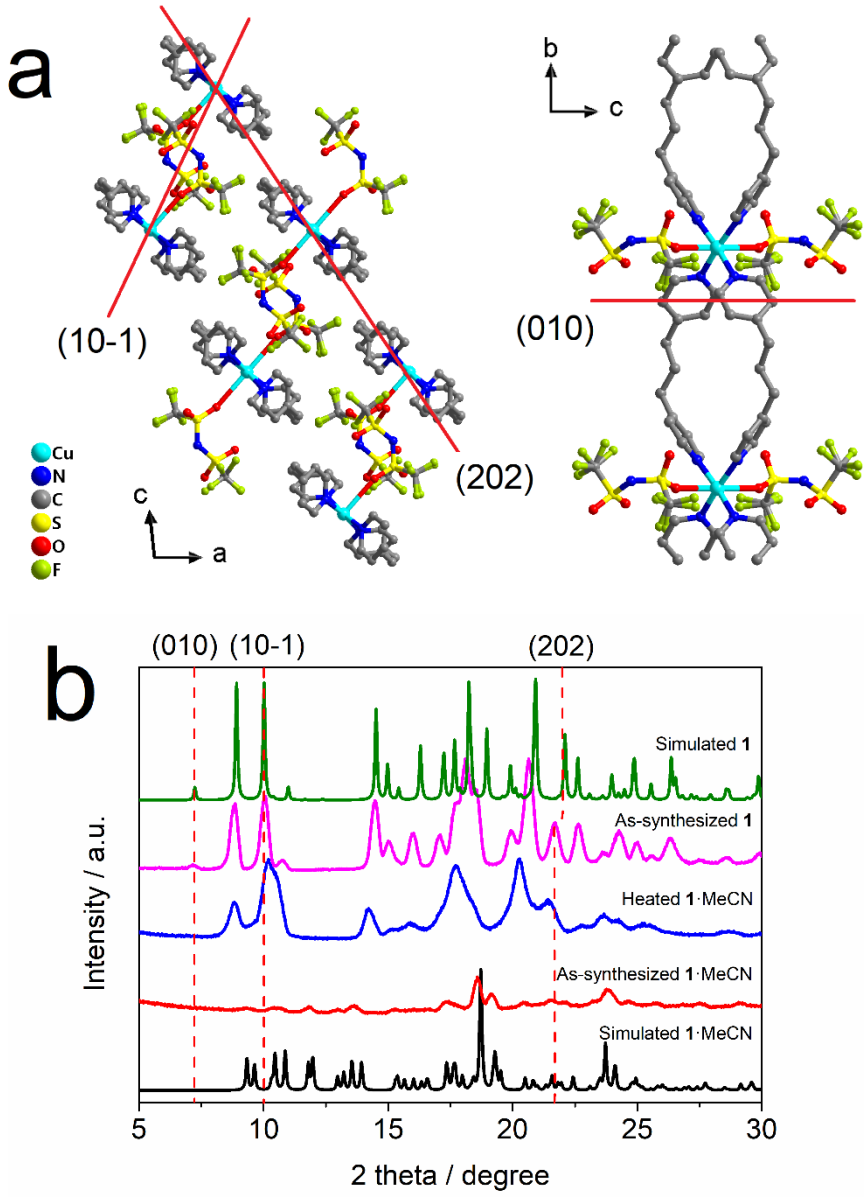

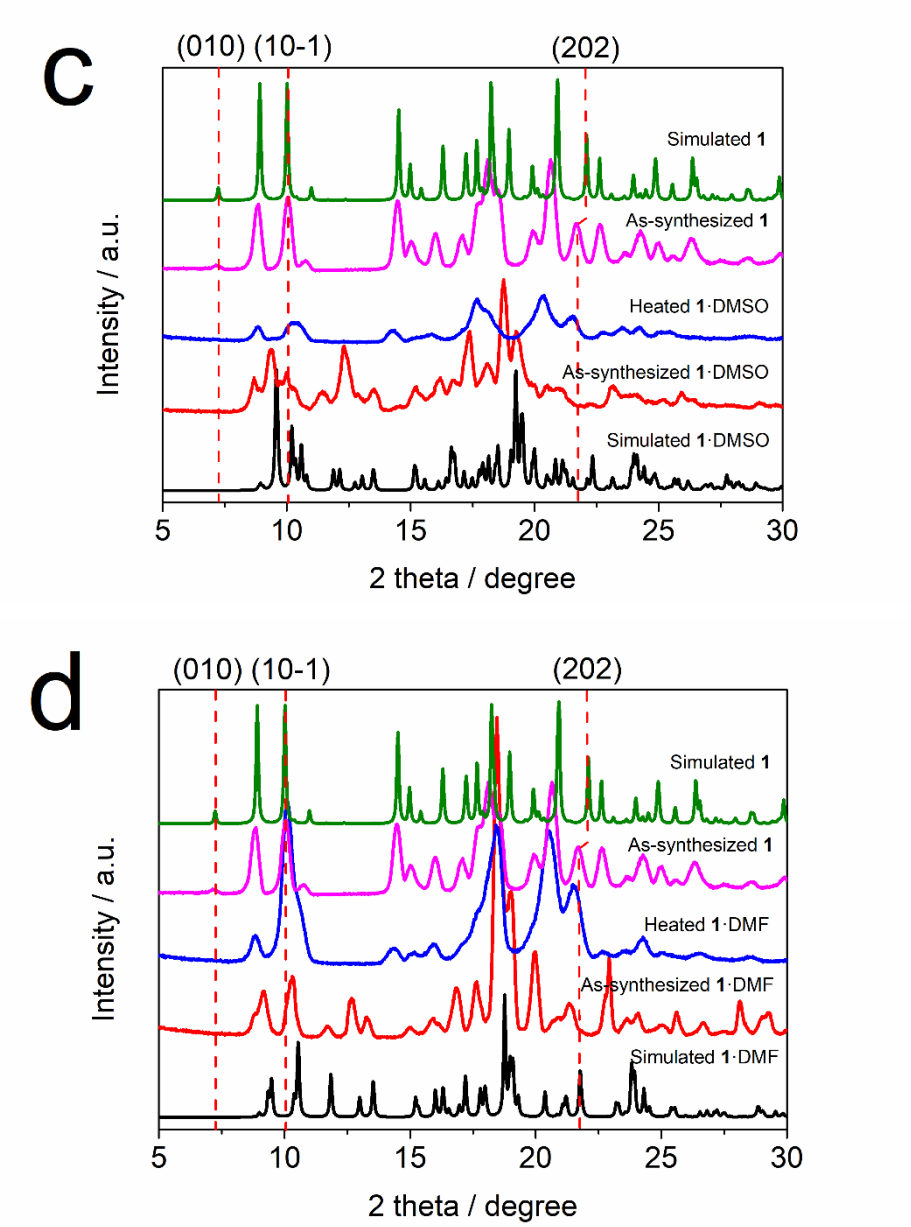

Fig. 3-4. (a) (010), (10-1) and (202) planes in **1**. (b-d) PXRD patterns of simulated and as-synthesized **1**, **1**·G and heated **1**·G ((b) G = MeCN, (c) G = DMSO, and (d) G = DMF).

The crystal morphologies and sizes of **1** and heated **1**·G were investigated by a scanning electron microscope (SEM) as shown in Fig. 3-5. The grain size of **1** is similar to that of heated **1**·MeCN and smaller than those of heated **1**·DMSO and **1**·DMF. However, in heated **1**·G, the observed grains look like aggregates of small rod-like crystallites. These SEM results demonstrate that the crystallites of heated **1**·G are

smaller than that of **1**, matching with the peak broadening of PXRD patterns in heated **1**·G.

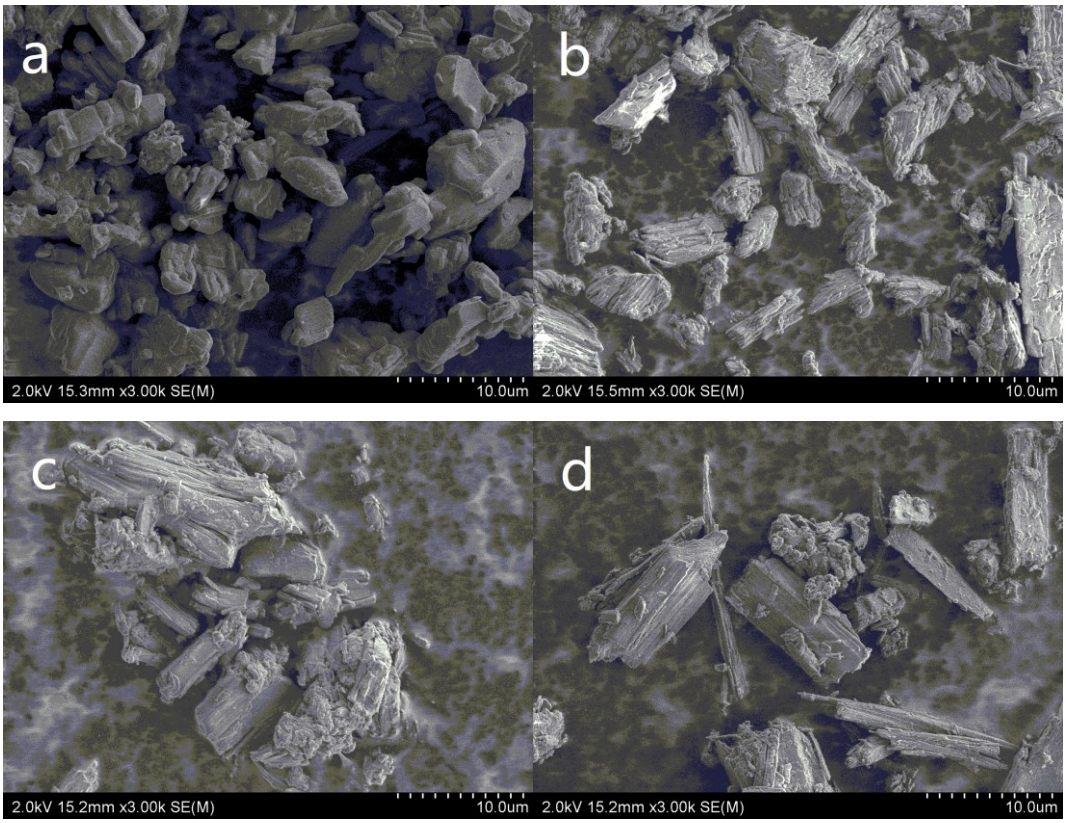

Fig. 3-5 SEM images of **1** (a) and heated **1**·G ((b) G = MeCN, (c) G = DMSO, and (d) G = DMF).

The effect of the difference in the structures of as-synthesized **1** and heated **1**·G were evaluated using CO_2 adsorption measurements at 195 K. Fig. 3-6(a) shows the CO_2 adsorption/desorption isotherms for the heated **1**·MeCN at 195 K. The typical gate-adsorption behavior is observed with P_g of 0.16 (relative pressure), lower than that in as-synthesized **1** (0.21). The second round of data measured using the same sample well overlaps the first one, indicating that the CO_2 uptake/release has less influence on the crystal structure and crystalline size, consistent with the results in Chapter 2. For as-synthesized **1**·DMSO and **1**·DMF, because they are thermally more stable than as-synthesized **1**·MeCN, I checked the CO_2 adsorption properties for them in addition to the heated **1**·DMSO and **1**·DMF. For as-synthesized **1**·DMSO, its CO_2 adsorption amount is near 15 cm^3 (STP)·g^{-1} at P/P_0 = 0.99, while as-synthesized **1**·DMF has small

CO_2 adsorption amount as shown in Fig. 3-6(b). After removing coordinated guest molecules, the clear gate-adsorption behaviors are found for both as shown in Fig. 3-6(b). The positions of P_g for the heated **1**·DMSO (0.17) and **1**·DMF (0.18) are lower than that of as-synthesized **1** and similar to that of **1**·MeCN as shown in Fig. 3-6(c).

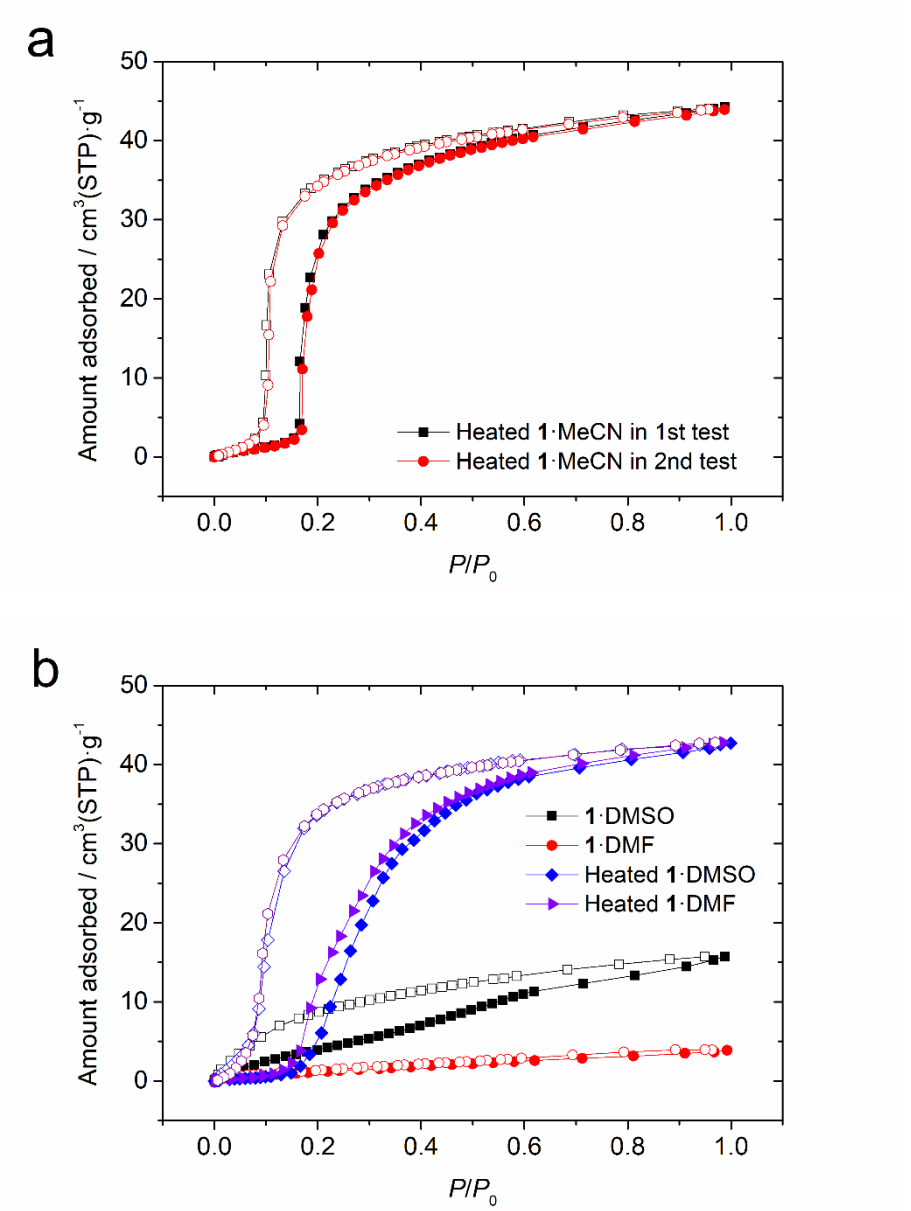

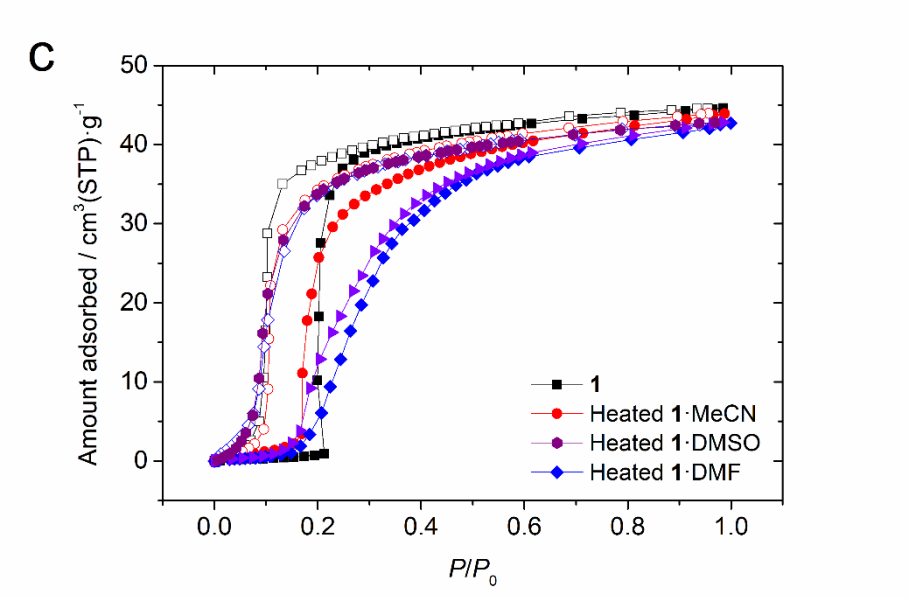

Fig. 3-6. CO_2 adsorption (closed symbols)/desorption (open symbols) isotherms of (a) desolvated **1**·MeCN, (b) as-synthesized and desolvated **1**·DMSO and **1**·DMF, (c) as-synthesized **1** (black), desolvated **1**·MeCN (red), desolvated **1**·DMSO (green) and desolvated **1**·DMF at 195 K.

3-3. Conclusions

Three kinds of one-dimensional CP, **1**·G were synthesized similar to **1**, but their copper ions partially coordinate with solvent molecules including MeCN, DMSO and DMF. After removing the coordinated solvent molecules, copper ions should weakly coordinate with two NTf_2^- renewably proved by IR spectra. Furthermore, the one-dimensional chains in desolvated **1**·G should be in jagged arrangement compared with **1**, although their packing structures are almost as same as **1** that were observed from PXRD pattern. The conversion from monocrystalline state to polycrystalline state noticeably reduced the inter-molecule interactions and made the gate-opening process be more prone to occur at lower pressure as shown in Fig. 3-6 without any loss of adsorption capacity for CO_2.

3-4. Experimental section

3-4-1. Materials

Commercially available reagents were used as received without further purification. $Cu(NTf_2)_2$ was synthesized using a previously described procedure.[15]

3-4-2. Syntheses of {[Cu (bpp)$_2$(G)]·2NTf$_2$} (1·G)

Single-crystal samples of **1**·G (G = MeCN, DMSO and DMF) were prepared by using a diffusion method in the straight glass tube containing a bottom layer of 0.1 M aqueous $Cu(NTf_2)_2$, a middle layer of 1:1 water and respective solvents, and a top layer of 0.2 M bpp in respective solvents. After 2 weeks, the formed transparent and plate like blue single crystals were separated by filtration, washed with water, and dried in the atmosphere.

3-4-3. FT-IR spectra

FT-IR spectra were measured using a Nicolet iS10 FT-IR (Thermo Scientific) equipped with a GladiATRTM accessory with a resolution of 4 cm^{-1} at room temperature.

3-4-4. TG analysis

TG curves were measured using a ThermoPlus2/TG-DTA8129 (Rigaku Corp.) in the temperature range from room temperature to 773 K under N_2 flow of 100 $mL \cdot min^{-1}$ at a heating rate of 10 $K \cdot min^{-1}$.

3-4-5. PXRD measurement

PXRD patterns were measured by RINT-Ultima Ⅲ diffractometer (Rigaku) under Cu Kα resource (λ = 1.54184 Å).

3-4-6. Gas adsorption isotherm experiments

CO_2 (195 K) adsorption/desorption isotherms were measured by using a BELSORP-

max (MicrotracBEL Corp.). Before the measurement, the samples were heated at 373 K in a vacuum for 20 h for activation by BELPREP-vac (MicrotracBEL Corp.).

3-4-7. Crystal structure determination

Structural analysis of **1·G** was performed using a Rigaku Micro Max-007 HF diffractometer and a Pilatus 200 K detector with Cu Kα radiation (λ = 1.54184 Å). Multi scan adsorption correction was applied to the reflection data of the crystals. A single crystal was mounted on a Micro Mounts^{TM} tip (MiTeGen) with Paratone 8277 (Hampton Research). The initial structure was solved using SHELXT, and structural refinement was performed by full-matrix least-squares techniques on F^2 using Olex2. Anisotropic refinement was applied to all atoms except hydrogen atoms. The crystallographic data of **1 G** are shown in Table 3-1.

Table 3-1. The crystallographic data of **1 G**.

	1·MeCN	**1**·DMSO	**1**·DMF
Chemical Formula	{[Cu(bpp)$_2$(MeCN)]·2NTf$_2$}	{[Cu(bpp)$_2$(DMSO)]·2NTf$_2$}	{[Cu(bpp)$_2$(DMF)]·2NTf$_2$}
Empirical formula	$C_{32}H_{31}CuF_{12}N_7O_8S_4$	$C_{32}H_{34}CuF_{12}N_6O_9S_5$	$C_{33}H_{35}CuF_{12}N_7O_9S_4$
Formula weight	1061.421	1098.504	1093.463
Crystal system	Triclinic	Triclinic	Monoclinic
Space group	*P*-1	*P*-1	*C*2/*c*
Temperature / K	173	173	173
a / Å	10.8986(3)	10.872(5)	11.6922(3)
b / Å	11.3463(5)	11.034(5)	18.9032(4)
c / Å	19.6465(7)	19.931(7)	19.8767(4)
α / °	94.566(3)	91.075(9)	90
β / °	95.548(3)	96.201(13)	98.875(2)
γ / °	116.760(4)	114.989(15)	90
V / Å^3	2133.90(13)	2148.95(16)	4340.55(17)
Z	2	2	4
GOF on F^2	1.030	1.111	1.106
R_1 [$I > 2\sigma(I)$][a]	0.0673	0.0926	0.0534
R_w [$I > 2\sigma(I)$][b]	0.1855	0.2548	0.1571

[a]$R_1 = \sum||F_o| - |F_c||/\sum|F_o|$. [b]$R_w = [(\sum w(|F_o|^2 - |F_c|^2)^2)/\sum w(F_o^2)^2]^{1/2}$.

3-4-8. Scanning electron microscope (SEM)

The morphology of sample particles was observed by a field-emission scanning electron microscope using Hitachi S-4800 at an acceleration voltage of 2.0 kV.

References

1. A. Schneemann, *et al.*, Flexible metal–organic frameworks *Chem. Soc. Rev.* **2014**, *43*, 6062.
2. G. Ferey & C. Serre. Large breathing effects in three-dimensional porous hybrid matter: facts, analyses, rules and consequences *Chem. Soc. Rev.* **2009**, *38*, 1380.
3. C. Serre , *et al.*, Very Large Breathing Effect in the First Nanoporous Chromium(III)-Based Solids: MIL-53 or $Cr^{III}(OH)\cdot\{O_2C\text{-}C_6H_4\text{-}CO_2\}\cdot\{HO_2C\text{-}C_6H_4\text{-}CO_2H\}_x\cdot H_2O_y$ *J. Am. Chem. Soc.* **2002**, *124*, 13519.
4. C. Mellot-Draznieks, et al. Very Large Swelling in Hybrid Frameworks: A Combined Computational and Powder Diffraction Study *J. Am. Chem. Soc.* **2005**, *127*, 16273.
5. J. Seo, *et al.*, A Pillared-Layer Coordination Polymer with a Rotatable Pillar Acting as a Molecular Gate for Guest Molecules *J. Am. Chem. Soc.* **2009**, *131*, 12792.
6. S. Horike, *et al.*, Soft Porous Crystals *Nat. Chem.* **2009**, *1*, 695.
7. R. Kitaura, *et al.*, Porous Coordination-Polymer Crystals with Gated Channels Specific for Supercritical Gases *Angew. Chem., Int. Ed.*, 2003, **42**, 428.
8. S. Noro, *et al.*, Porous Coordination Polymer Polymorphs with Different Flexible Pores Using a Structurally Flexible and Bent 1,3-Bis(4-pyridyl)propane Ligand *Inorg. Chem.* **2013**, *52*, 4229.
9. M. L. Foo, *et al.*, An Adsorbate Discriminatory Gate Effect in a Flexible Porous Coordination Polymer for Selective Adsorption of CO_2 over C_2H_2 *J. Am. Chem. Soc.* **2016**, *138*, 3022.
10. N. Yanai, *et al.*, Gas Detection by Structural Variations of Fluorescent Guest Molecules in a Flexible Porous Coordination Polymer *Nat. Mater.* **2011**, *10*, 787.
11. Y. Cheng, *et al.*, Reversible Structural Change of Cu-MOF on Exposure to Water and Its CO2 Adsorptivity *Langmuir* **2011**, *27*, 6905.
12. H. Miura, *et al.*, Tuning the gate-opening pressure and particle size distribution of the switchable metal-organic framework DUT-8(Ni) by controlled nucleation

in a micromixer. *Dalton Trans.*, **2017**, *46*, 14002.

13. Y. Sakata, *et al.*, Shape-memory Nanopores Induced in Coordination Frameworks by Crystal Downsizing *Science*, **2013**, *339*, 193.
14. S. Watanabe, *et al.*, Synthesis of zeolitic imidazolate framework-8 particles of controlled sizes, shapes, and gate adsorption characteristics using a central collision-type microreactor *Chem. Eng. J.* **2017**, *313*, 724.
15. Fujii, K. *et al.*, Conformational Equilibrium of Bis(trifluoromethanesulfonyl) Imide Anion of a Room-Temperature Ionic Liquid: Raman Spectroscopic Study and DFT Calculations. *J. Phys. Chem. B* **2006**, *110*, 8179.

Chapter 4

A synchronous change in fluid space and encapsulated anions in a crystalline polymethylene unit containing coordination polymer

Abstract

Porous materials possessing fluid spaces are of great interest in the field of material science because they have the capability of undergoing unique, external stimuli-promoted and guest uptake/release-responsive changes in shapes and sizes. Polymethylene chains are postulated to be important components in coordination polymers (CPs) enabling them to possess fluid spaces. The three-dimensional (3D) cationic CP, $[Cu(bib)_{2.5}]$ (bib = 1,4-bisimidazole butane), which contains organic bridging ligands with conformationally flexible tetramethylene ($(CH_2)_4$) units, was designed to assess this proposal. The combined results of DSC measurements, single-crystal X-ray diffraction analysis and impedance spectroscopy demonstrate that this CP encapsulating bis(trifluoromethylsulfonyl)imide (NTf_2^-) anions contains fluid space and that it undergoes a crystal-to-crystal transition in association with a synchronous change in the conformations of both the bib ligand, caused by C-C bond rotation, and the NTf_2^- anion stemming from rotation about the N-S bond.

4-1. Introduction

Materials containing fluid space, which undergo size and shape changes of space in response to guest uptake/release or external stimuli such as light, heat, magnetic field and mechanical force (Fig. 4-1), not only have interesting guest-recognition and transport properties but also are useful for exploring the unique dynamics of encapsulated molecules and substituents.[1-9] CPs are fluid space containing materials because they can have multiple constitutions arising from diverse of organic ligands as well as inorganic metal nodes. This constitutional complexity enables CPs to have frameworks that contain a variety of movable units which exhibit rotation and extension/shrinkage, as well as changes in coordination bond distances/angles.[1,2] For example, Fischer, et al. reported that pillared-layered CPs containing 2-methoxyethoxy substituents undergo heat induced reversible structural transitions from less porous narrow pore forms to expanded more porous large pore forms, caused by enhanced movement of the encapsulated 2-methoxyethoxy substituents.[8] In addition, Inukai, et al. found that rotation of pyridyl and methylbenzene ring rotors embedded in an interdigitated two-dimensional CP triggers the expansion of pore windows and consequent CO_2 adsorption.[9]

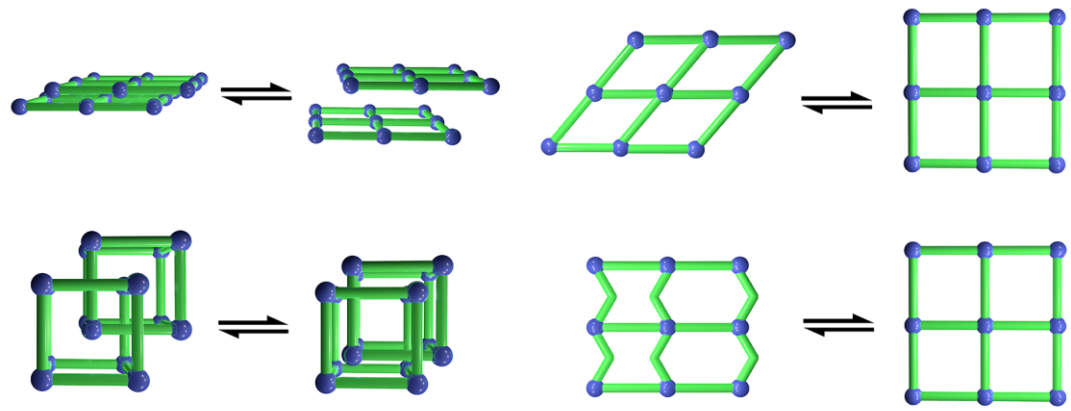

Fig. 4-1. Schematic description of CP based fluid space. The blue spheres and green rods represent metal ions and organic ligands, respectively.

Recent investigations have explored an approach for installing fluid space in materials that is based on the incorporation of a polymethylene ($(CH_2)_n$) chain. This

strategy is based on the consideration that rotation about C-C bonds interconverting *gauche* (*G*) and *trans* (*T*) conformations can lead to formation of a variety of different shapes of the polymethylene chains. In one effort, Ciani at al. investigated the crystal structures of Ag CPs possessing $NC(CH_2)_nCN$ type bridging ligands that exist in different conformations depending on the nature of encapsulated counter anions.[10-13] For example, the ligand in $\{[Ag(NC(CH_2)_7NC)_2]\cdot BF_4\}$ exists in two conformations, *GTTTTG* and *TTTTTG*, in the crystalline state, while its analogs $\{[Ag(NC(CH_2)_7NC)_2]\cdot A\}$ (A = ClO_4, PF_6, AsF_6, and SbF_6) exist in two different ligand conformations including *GTTTGT* and *GTTTG'T*.[11] Moreover, the one-dimensional CP $\{[Mn(1,10\text{-phenanthroline})_2(O_2C(CH_2)_6CO_2)]_2\cdot(HO_2C(CH_2)_6CO_2H)\cdot 8H_2O\}$, described by Zheng et al., exists in two types of ligand conformations including *TTTTT* and *GTTTG'*.[14]

It is anticipated that CPs possessing polymethylene chain containing organic bridging ligands as fluid spacers could display interesting external stimuli responsive properties. It is noteworthy that materials of this type have been relatively unexplored to date. In a recent study, the results of which are described below, I prepared the 3D flexible cationic CP, $[Cu(bib)_{2.5}]$, which contains a $(CH_2)_4$ spacers. As anticipated, I observed that this CP encapsulates NTf_2^- anions to form $\{[Cu(bib)_{2.5}]\cdot 2NTf_2\}$ (**3**), which undergoes a reversible heat-induced phase transition in the crystalline state associated with synchronous changes in the conformations of the $(CH_2)_4$ spacer and NTf_2^- anions.

4-2. Results and discussion

The new CP **3** was produced by reacting $Cu(NTf_2)_2$ with bib in a mixture of H_2O and DMSO. Elemental and powder X-ray diffraction (PXRD) analysis showed that this substance has the same atomic composition and structure as those determined by using single-crystal X-ray diffraction analysis (Fig. 4-2), indicating high purity.

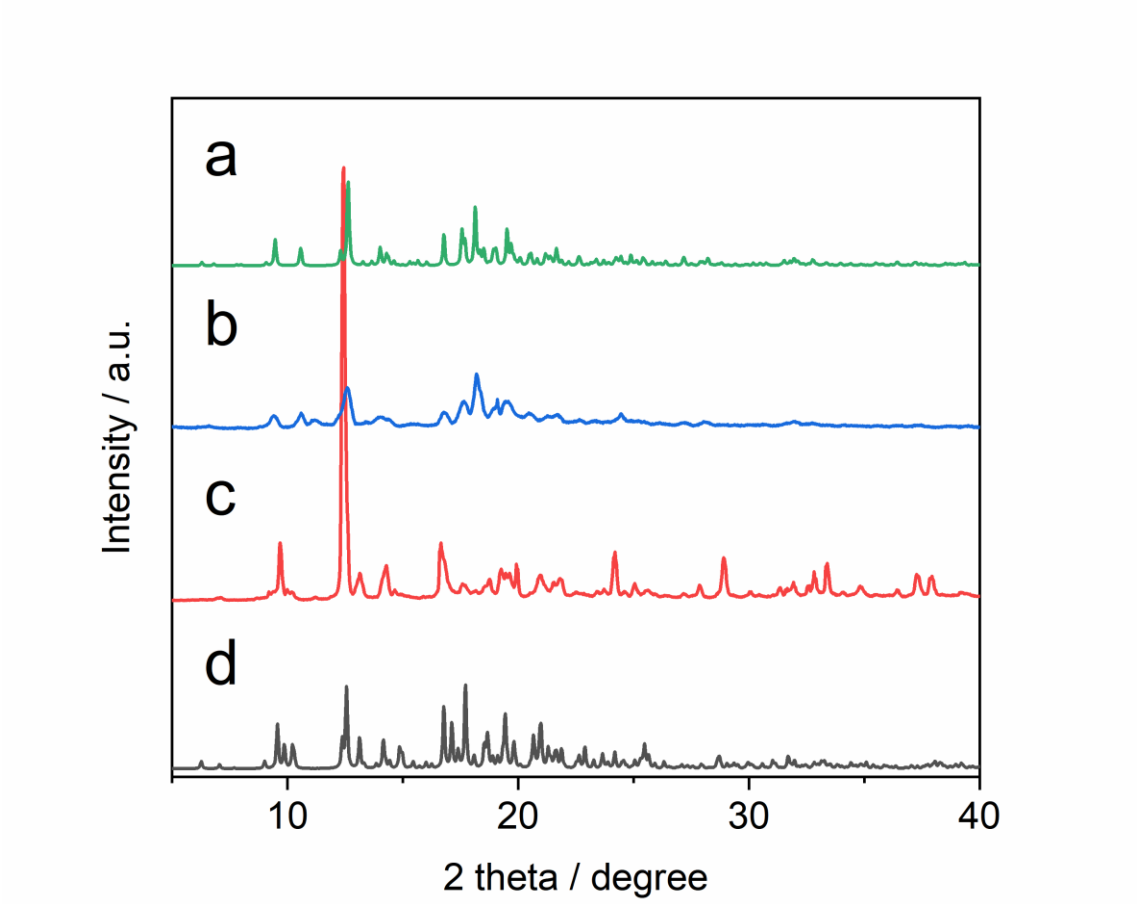

Fig. 4-2. PXRD patterns of (a) simulated **3** at 298 K, (b) as-synthesized **3** at 298 K, (c) as-synthesized **3** at 248 K, and (d) simulated **3** at 248 K.

Differential scanning calorimetry (DSC) measurements were performed to elucidate the phase transition behavior of **2**. The results show that in the first heating step from 173 K to 373 K, a sharp endothermic peak occurs at 281 K with $\Delta H = 6.7$ kJ·mol^{-1} and $\Delta S = 24.0$ J·mol^{-1}·K^{-1} (Fig. 4-3). In addition, in the first cooling process, a sharp exothermic peak occurs at 279 K with $\Delta H = 6.8$ kJ·mol^{-1} and $\Delta S = 24.4$ J·mol^{-1}·K^{-1}. Furthermore, an endothermic peak arises in the second heating process at the same temperature and with the same ΔH and ΔS as those in the first heating process,

indicating that the phase transition process taking place is reversible.

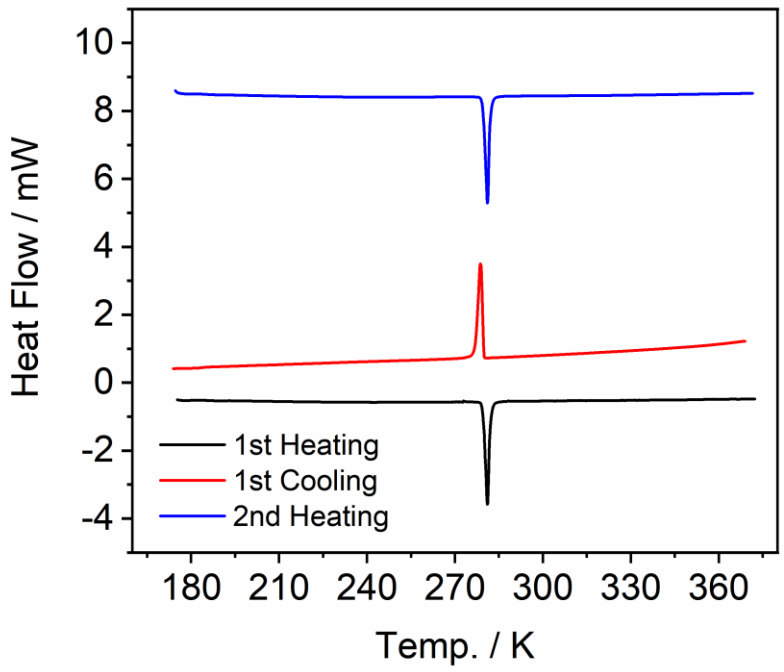

Fig. 4-3. DSC curves of **3** between 173 K and 373 K.

Crystal structures of **3** before and after the occurrence of the reversible phase transition were determined by using single-crystal X-ray diffraction analysis.[14] Single-crystal to single-crystal phase transition is useful for understanding its phenomenon in detail using standard single-crystal X-ray diffraction analysis.[15] The structure of **3** at 173 K (denoted **3-lp**, Fig. 4-4) has a cationic framework comprised of pentagonally coordinated Cu^{2+} ions with a τ value of 0.53 and bridging bib ligands (Fig. 4-4(a)), indicating that the coordination geometry lies between an ideal square-pyramid and trigonal-bipyramid.[16] One Cu-N distance is 2.199(1) Å and the other four are in the 2.000(2)-2.041(2) Å range, which are similar to those in coordination compounds comprised of Cu^{2+} ions and imidazole-containing ligands.[17-20] Three types of bib ligands with the *GTG'*, *TTT* and *GTT* conformations exist in **3-lp**, and these ligands bridge the Cu^{2+} centers to form a 2D non-flat $[Cu(bib)_2]$ layer (Fig. 4-4(b)). Each 2D layer is bridged by other bib pillar ligands that have a *GTG'* conformation, resulting in a 3D cationic $[Cu(bib)_{2.5}]$ framework with a quasi-diamond (dia) like topology (Fig. 4-

4(c)). Interestingly, the 3D cationic framework possesses a large void with a void space of 40.8% calculated using MERCURY software (probe radius = 1.2 Å, approximate grid spacing = 0.7 Å, these parameters were used to calculate the void space).[21] Additionally, two types of NTf_2^- anions having *trans* conformations exist in and fully occupy the void space of **3-lp** (Fig. 4-4(d)). One of the NTf_2^- anions (**A1**) participates in weak hydrogen-bonding with the bib ligand, in which an oxygen of NTf_2^- anion interacts with an imidazole ring hydrogen with respective O•••H and O•••C distances of 2.369(2) and 3.188(4) Å, and an O•••H-C angle of 146.8(2)°. Moreover, this anion is located around the unoccupied site of the five-coordinated Cu^{2+} center, but no coordinative interaction occurs between the oppositely charged moieties and the closest Cu•••F distance is 3.698(2) Å. The other NTf_2^- anion, **A2**, weakly hydrogen-bonds with an imidazole ring hydrogen in the bib ligand, with respective O•••H and O•••C distances of 2.366(3) and 3.149(4) Å, and an O•••H-C angle of 141.7(2)°.

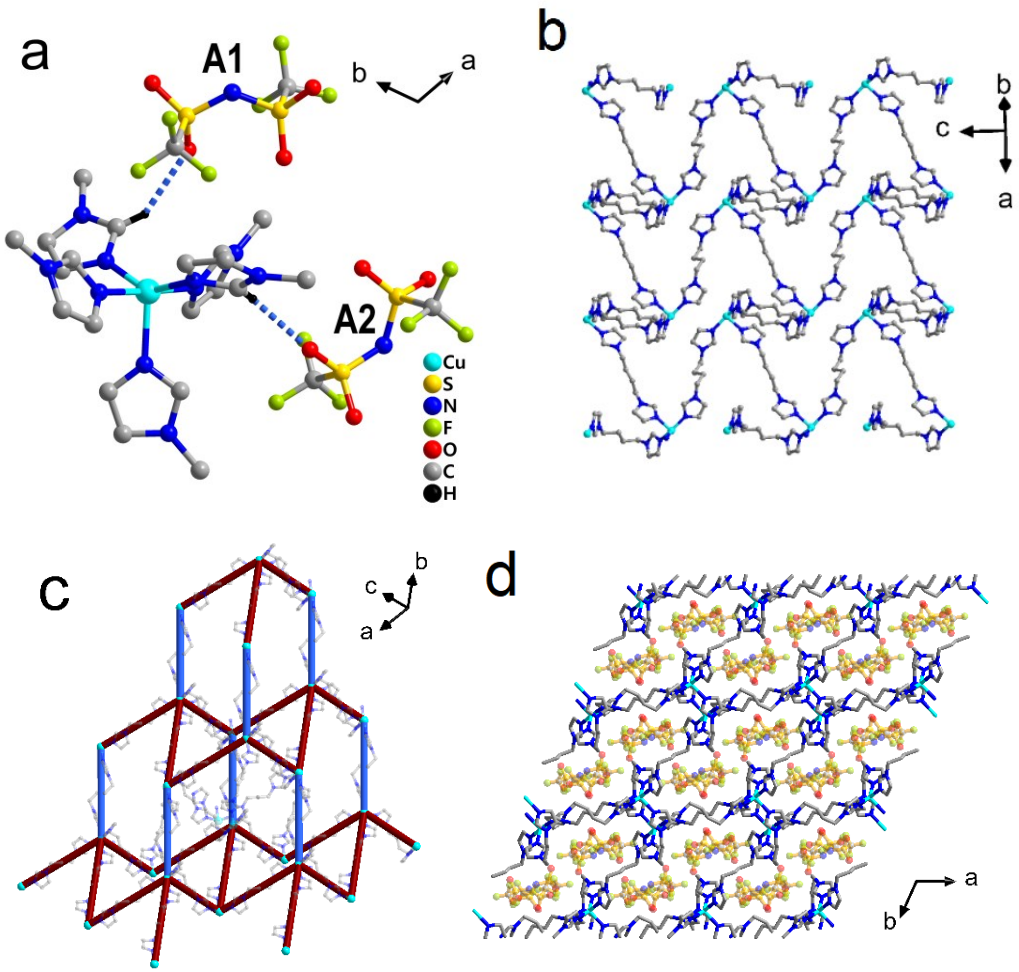

Fig. 4-4. Crystal structure of **3-lp** at 173 K. (a) Coordination environment around the Cu^{2+} center and view of the weak hydrogen-bonding interactions between NTf_2^- anions **A1** and **A2** with bib ligands. (b) view of the 2D non-flat [$Cu(bib)_2$] layer in **3** at 173 K. (c) 3D quasi-diamond network comprised of 2D non-flat [$Cu(bib)_2$] layers (represented by sky blue spheres and red sticks) and bib pillars (blue sticks). NTf_2^- anions are omitted. (d) packing structure, in which NTf_2^- anions are added to the void spaces.

Clear structural changes take place when the crystal **3** is heated to 298 K. The high temperature phase, denoted as **3-hp**, has a 3D cationic framework and quasi-dia topology that are analogous to those of **3-lp**. Also, Cu^{2+} ions in **3-hp** are in a similar five-coordinated environment with a τ value of 0.56 (Fig. 4-5(a)), and with one Cu-N distance being 2.175(3) Å and the other four falling in the 1.999(5)-2.044(4) Å range. Although, the 3D cationic [$Cu(bib)_{2.5}$] framework in **3-hp** is composed from 2D undulated [$Cu(bib)_2$] layers (Fig. 4-5(b)) and pillar bib ligands, the same way as in **3-lp**, the distance between coordinated N atoms of pillar bib ligand of 10.1 Å in **3-hp** is significantly longer than 8.9 Å in **3-lp** as a consequence of a conformational change of the bib ligand from *GTG'* in the former to *TTT* in the latter (Fig. 4-5(c) and 4-5(d)). The void space in the cationic framework of **3-hp** was calculated to be 43.5% using MERCURY, a value that is larger than the void space in **3-lp**. Moreover, NTf_2^- anions fully occupy the void space in the 3D cationic framework. It should be noted that heating **3** to 298 K also causes a significant structural change in the NTf_2^- anions (Fig. 4-5(b) and 4-5(c)). Specifically, one of these anion, **A1**, retains a *trans* conformation and participates in hydrogen bonding with the hydrogen of an imidazole ring in bib via O•••H and O•••C distances of 2.484(9) and 3.21(1) Å, respectively, and a O•••H-C angle of 135.5(5)° (Fig 4-5(a)). Moreover, no coordinative interaction exists between encapsulated NTf_2^- anions and Cu^{2+} ions and the shortest Cu•••F distance is 4.01(1) Å, which is longer than that in **3-lp**. Significantly, the other anion, **A2**, exists in a *cis* conformation and does not participate in hydrogen bonding with the cationic framework. Because both phases have no enough space to allow conformational changes, the

changes in the conformations of both bib ligand and NTf_2^- anion should occur synchronously.

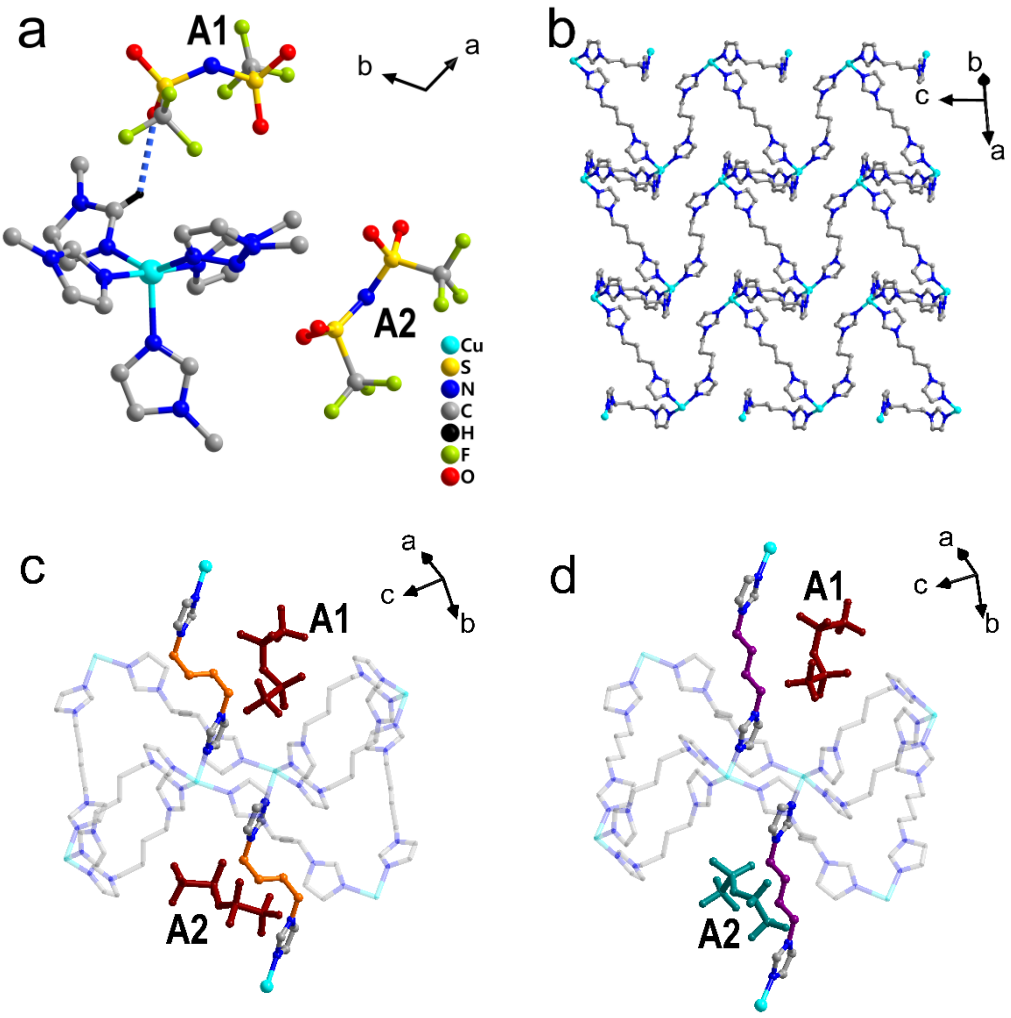

Fig. 4-5. (a) Coordination environment surrounding the Cu^{2+} center in **3-hp** and view of the weak hydrogen-bonding interaction between the NTf_2^- anion **A1** and bib ligand. (b) View of the 2D non-flat $[Cu(bib)_2]$ layer in **3-hp**. (c and d) Comparison of ligand and anion conformations in (c) **3-lp** and (d) **3-hp**.

The observations described above clearly show that the thermal phase transition of **3** takes place in association with a synchronous change in conformations of the NTf_2^- anions and bib ligands. Importantly, this is the first time the *trans-cis* isomerization of NTf_2^- anion in the solid state has been detected. Temperature-dependent X-ray diffraction analysis was performed to determine changes that take place in cell

parameters. Between 273 K and 298 K, the *b* axis, corresponding to the long axis direction of the pillar ligand, increases by 3.8%, while both the *a* and *c* axes remain nearly unchanged (Fig. 4-6(a)). At the same time, the α and β angles decrease by 4.2 and 4.0%, respectively, but the γ angle remains nearly unchanged (Fig. 4-6(b)). As a result of these alterations and consistent with observations made in the DSC studies, the unit cell volume of the crystal of **3** undergoes a noticeable 2.2% enlargement when the temperature is increased from 273 K to 298 K.

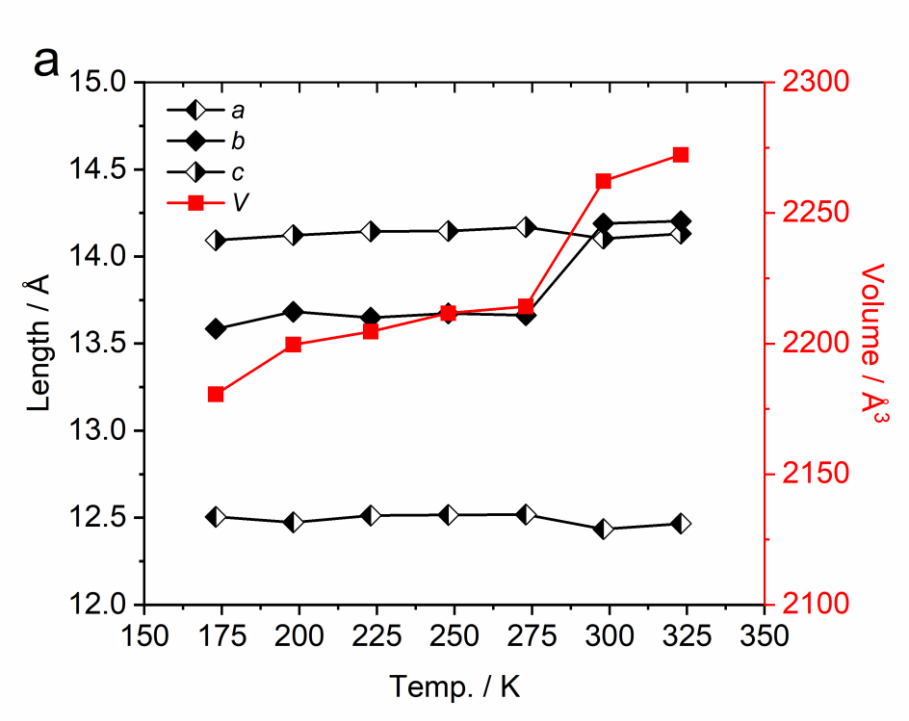

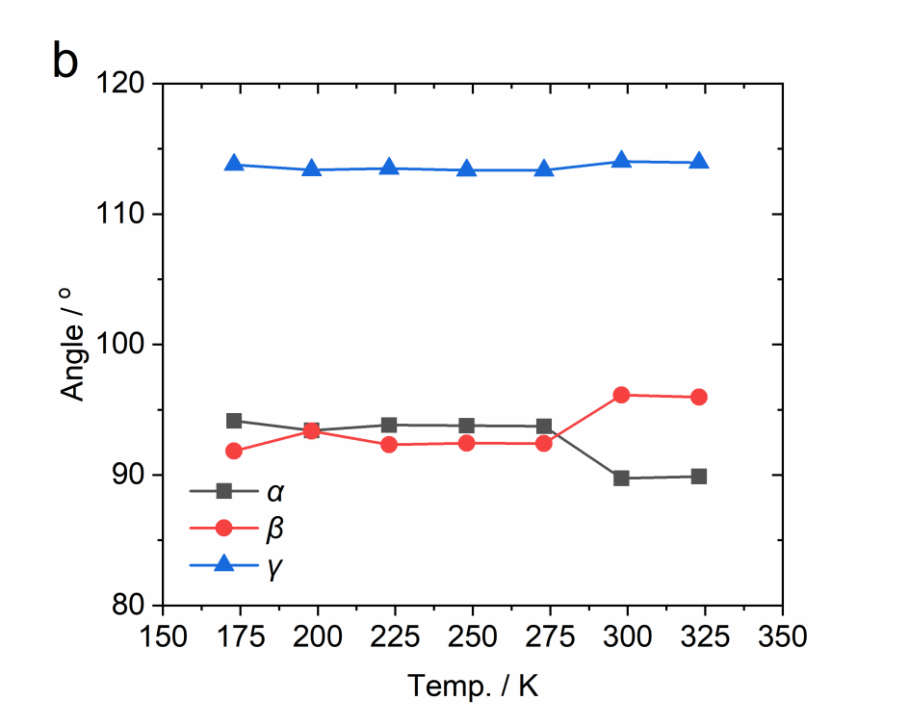

Fig. 4-6. Temperature-dependent cell parameters ((a) *a*, *b*, *c* and *V*; (b) *α*, *β* and *γ*) in **3**.

The results arising from single-crystal X-ray diffraction analysis demonstrate that the reversible phase transition observed by using DSC, associated with changes in the conformation of the NTf_2^- and bib moieties, occurs by a first order, crystal-to-crystal pathway with a ΔH of 6.7 kJ·mol^{-1}. The ΔH for the *trans* to *cis* conformational change in NTf_2^- anions in the liquid state is reported to be in the range 3.4-7.3 kJ·mol^{-1},[22] while the ΔHs for rotation around C-C σ-bonds in alkyl chains in the crystalline states of a *n*-butyl linked Co complex and $CO_2(CH_2)_3CH_3$ containing estradiol 17*β* valerate are 2.6 and 4.5 kJ·mol^{-1}, respectively.[23,24] It is expected that the ΔH for a process in which changes in the conformation of both the bib ligand and NTf_2^- anion are taking place synchronously would be smaller than a simple sum of the ΔHs for each change occurring independently. Considering that the ΔH value for the NTf_2^- anion corresponds to the liquid state, the experimental ΔH for the crystal-to-crystal phase transition of **3** appears to indicate that synergetic motion of the bib and NTf_2^- components takes place.

In the final phase of this effort, thermally induced structural changes occurring in **3** were evaluated using impedance spectroscopy. The spectra of the real and imaginary

components of the dielectric permittivity (ε' and ε'', respectively) of **3** at temperatures in the 294-266 K range, which cover those that cause the crystal-to-crystal phase transition, are shown in Fig. 4-7(a) and (b). An obvious change in ε' takes place between 277 and 282 K, but no significant difference in ε'' occurs in this temperature range. Furthermore, alternating current conductivity (σ_{ac}) remains nearly unchanged and its value is $<10^{-9}$ S·cm^{-1} at 294 K as shown in Fig. 4-7(c). Because the NTf_2^- anion is more polar than the $(CH_2)_4$ moiety, the observed impedance changes should only reflect structure changes of the NTf_2^- anions. Generally, a molecule having a large permanent dipole moment has a larger ε' than one having a small dipole moment.[25,26] Because the dipole moment of the *cis* conformation of the NTf_2^- anion (4.4-5.4 D) is larger than that of its *trans* counterpart (0.2-0.4 D),[27] the rapid rise in ε' seen when the temperature exceeds 282 K is a reasonable indicator of the occurrence of this conformational change. These results suggest that the NTf_2^- anions in the crystal of **3** do not undergo significant translational motion within the framework in the measured temperature range but that they do experience twisting within the fluid space of the 3D cationic framework.

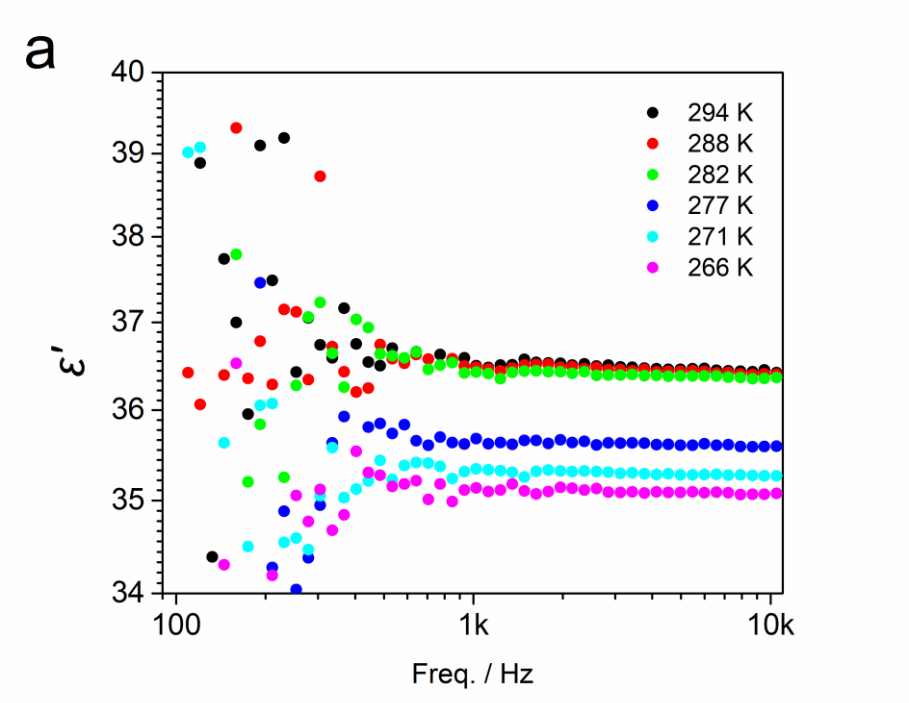

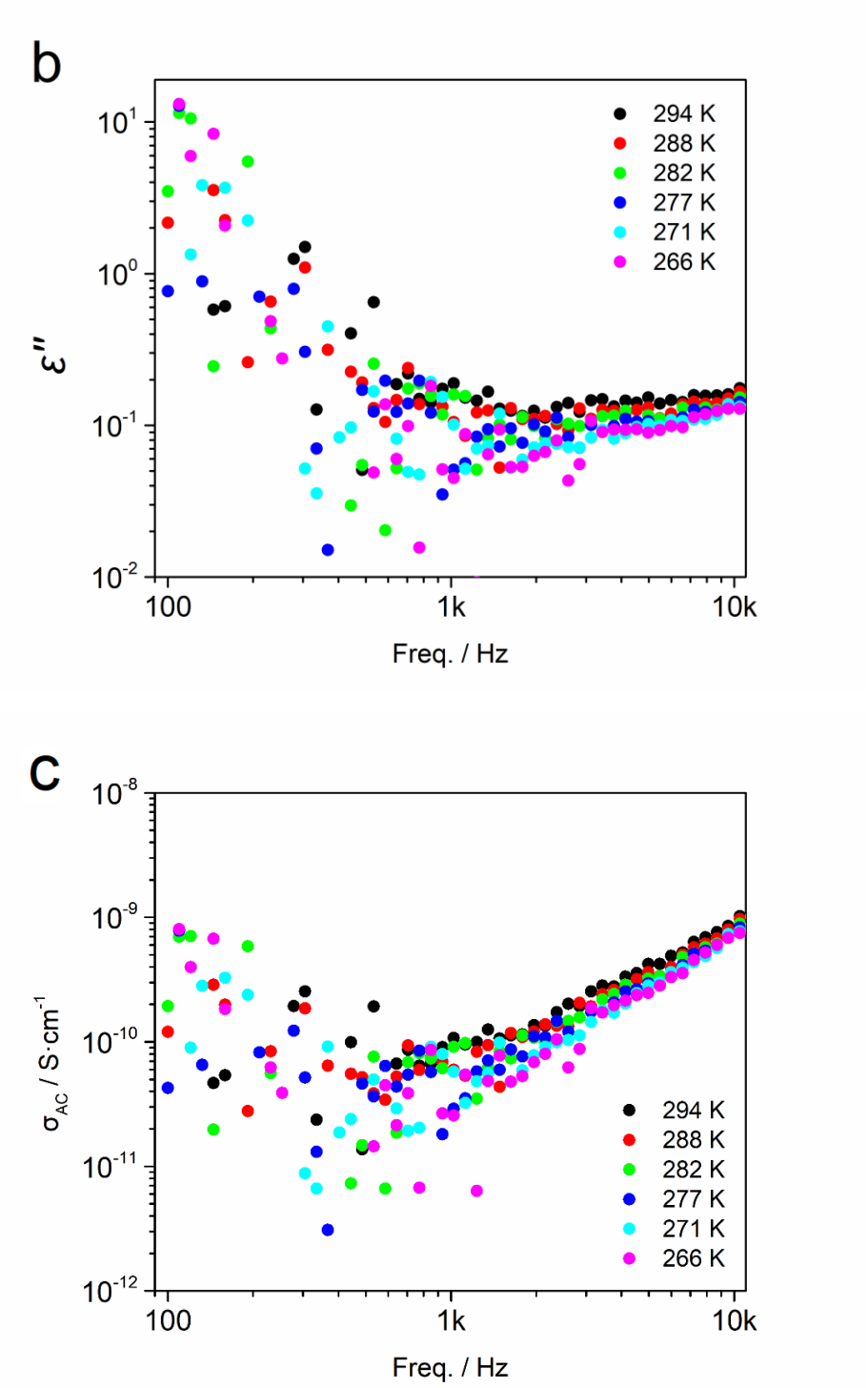

Fig. 4-7. Frequency and temperature dependent real (a), imaginary components (b) dielectric constants and (c) AC conductivities of **3** in the cooling process.

4-3. Conclusion

In the investigation described above, I designed and explored a novel CP that has unique properties associated with the presence of fluid space and the occurrence of a thermally induced crystal change. The CP contains a conformationally flexible tetramethylene chain in organic bridging ligands and NTf_2^- anions. The combined results of DSC measurements, single-crystal X-ray diffraction analysis and impedance spectroscopy demonstrate that the crystal-to-crystal transition occurring in this CP is associated with a synchronous change in the conformations of both the bib ligand, caused by C-C bond rotation, and the NTf_2^- anion stemming from rotation about the N-S bond. The findings suggest that the novel strategy of using polymethylene chain spacer units for creating fluid space is viable and it could serve as the foundation for the design of a variety of porous materials that have interesting stimuli-responsive adsorption, separation, ion conducting, and catalytic properties.

4-4. Experimental section

4-4-1. Materials

Commercially available reagents were used as received without further purification. $Cu(NTf_2)_2$ and 1,4-bisimidazole butane (bib) were synthesized using previously described procedures.[30,31]

4-4-2. Synthesis of {$[Cu(bib)_{2.5}]\cdot 2NTf_2$} (3)

A single-crystal **3** was prepared using a diffusion method in the straight glass tube containing a top layer of 0.1 M aqueous $Cu(NTf_2)_2$, a middle layer of 1:1 water and DMSO, and a bottom layer of 0.2 M bib in DMSO. After 2 weeks, the transparent and plate like blue single crystals were obtained. The crystals were separated by filtration, washed with water, and dried in the atmosphere. Elemental analysis was used to confirm the atomic composition and purity of the as-synthesized single crystals. Elemental analysis (%) calcd for $C_{29}H_{35}CuF_{12}N_{12}O_8S_4$: C 31.68, H 3.21, N 15.29, F 20.74, S 11.66. Found: C 30.73, H 3.13, N 14.46, F 20.80, S 12.85.

4-4-3. Elemental analysis

Elemental analysis was measured in Global Facility Center, Hokkaido University, using MICRO CORDER JM10 (J-SCIENCE LAB) and DX-500 (Dionex).

4-4-4. DSC

DSC measurement was carried out with a Q2000 differential scanning calorimeter (TA Instruments) in the temperature range 173-373 K at a heating rate of 10 $K\cdot min^{-1}$ and a cooling rate of 5 $K\cdot min^{-1}$ under a flow of N_2 gas (flow rate 50 $mL\cdot min^{-1}$).

4-4-5. Dielectric measurement

Temperature- and frequency-dependent dielectric constants were measured using a two-probe alternating current (AC) impedance method at a frequency range of 10^3 to 10^4 Hz (an Agilent precision impedance analyzer, 4294A). Ground crystals of **3** were

sandwiched between ITO electrodes to form an arrangement with an electrode area and gap of 50 mm^2 and 1.49 mm, respectively. The sample sandwiched by ITO electrodes was installed in cryostat and temperature was controlled by an ethanol bath with a handy cooler (model 202TCN, As one). The AC conductivities were calculated using the following equation:

$$\sigma_{AC} = \varepsilon_0 \times 2\pi f \times \varepsilon'' / 100.$$

in which ε_0 is a vacuum permittivity, f is a frequency and ε'' is an imaginary-part dielectric constant.

4-4-6. PXRD measurements

PXRD patterns were measured by RINT-Ultima III diffractometer (Rigaku) under Cu Kα resource (λ = 1.54184 Å). Variable-temperature PXRD patterns measured with a TTK 450 chamber (Anton Paar).

4-4-7. Crystal structure determination

Temperature-dependent structural analysis of **3** was performed using a Rigaku Micro Max-007 HF diffractometer and a Pilatus 200 K detector with Cu Kα radiation (λ = 1.54184 Å). Multi scan adsorption correction was applied to the reflection data of the crystals **3-lp** and **3-hp**. A single crystal was mounted on a Micro Mounts™ tip (MiTeGen) with Paratone 8277 (Hampton Research). The initial structure was solved using SHELXT,[28] and structural refinement was performed by full-matrix least-squares techniques on F^2 using Olex2.[29] Anisotropic refinement was applied to all atoms except hydrogen atoms. The crystallographic data of **3-lp** and **3-hp** are shown in Table 4-1, and lattice parameters of **3** at different temperatures are shown in Table 4-2.

Table 4-1. The crystallographic data of the crystals **3-lp** and **3-hp**.

	3-lp	**3-hp**
Chemical Formula	$C_{29}H_{35}CuF_{12}N_{12}O_8S_4$	$C_{29}H_{35}CuF_{12}N_{12}O_8S_4$
Formula weight	1099.455	1099.455
Crystal system	Triclinic	Triclinic
Space group	*P* -1	*P* -1
Temperature / K	173	298
a / Å	12.509(3)	12.4586(2)
b / Å	13.585(3)	14.1893(3)
c / Å	14.0972(18)	14.1036(3)
α / °	94.2032(10)	89.7491(18)
β / °	91.887(7)	96.139(2)
γ / °	113.899(7)	114.018(2)
V / Å^3	2179.2(7)	2262.18(9)
Z	2	2
d / g·cm^{-3}	1.675	1.614
μ (Cu Kα), cm^{-1}	3.528	3.401
Reflections measured	26034	27919
Independent reflections	8304	8613
Reflections used	8304	8613
GOF on F^2	1.090	1.558
R_1 [$I > 2\sigma(I)$][a]	0.0663	0.1101
R_w [$I > 2\sigma(I)$][b]	0.1923	0.3441

[a] $R_1 = \sum||F_o| - |F_c||/\sum|F_o|$. [b] $R_w = [(\sum w(|F_o|^2 - |F_c|^2)^2)/\sum w(F_o^2)^2]^{1/2}$.

Table 4-2. Lattice parameters of **3** at different temperatures.

Temperature / K	**173**	**198**	**223**	**248**
Crystal system	Triclinic	Triclinic	Triclinic	Triclinic
Space group	*P* -1	*P* -1	*P* -1	*P* -1
a / Å	12.509(3)	12.4729(7)	12.5125(3)	12.5156(2)
b / Å	13.585(3)	13.6832(6)	13.6496(2)	13.6733(4)
c / Å	14.0972(18)	14.1223(2)	14.1440(3)	14.1464(4)
α / °	94.2032(10)	93.421(3)	93.8269(17)	93.780(2)
β / °	91.887(7)	93.373(3)	92.333(2)	92.436(2)
γ / °	113.899(7)	113.371(5)	113.488(2)	113.347(2)
V / Å^3	2179.2(7)	2199.58(18)	2204.58(8)	2211.58(10)

Temperature / K	**273**	**298**	**323**
Crystal system	Triclinic	Triclinic	Triclinic
Space group	*P* -1	*P* -1	*P* -1
a / Å	12.5183(3)	12.4586(2)	12.4665(2)
b / Å	13.6632(5)	14.1893(3)	14.2034(3)
c / Å	14.1695(3)	14.1036(3)	14.1313(3)
α / °	93.731(2)	89.7491(18)	89.889(2)
β / °	92.403(2)	96.139(2)	95.961(2)
γ / °	113.351(3)	114.018(2)	113.944(2)
V / Å^3	2214.24(11)	2262.18(9)	2272.26(8)

4-5. References

1. S. Kitagawa, *et al.*, Functional porous coordination polymer. *Angew. Chem., Int. Ed.* **2004**, *43*, 2334.
2. A. Schneemann, *et al.*, Flexible metal–organic frameworks. *Chem. Soc. Rev.* **2014**, *43*, 6062.
3. K. Biradha, *et al.*, Crystal-to-Crystal Sliding of 2D Coordination Layers Triggered by Guest Exchange. *Angew. Chem., Int. Ed.* **2002**, *41*, 3395.
4. N. Yanai, *et al.*, Guest-to-Host Transmission of Structural Changes for Stimuli-Responsive Adsorption Property. *J. Am. Chem. Soc.* **2012**, *134*, 4501.
5. L. Vanduyfhuys, *et al.*, Thermodynamic insight into stimuli-responsive behaviour of soft porous crystals. *Nat. Commun.* **2018**, *9*, 204.
6. M. X. Wu & Y. W. Yang, Metal-Organic Framework (CP)-Based Drug/Cargo Delivery and Cancer Therapy. *Adv. Mater.* **2017**, *29*, 1606134.
7. L. R. Redfern & O. K. Farha, Mechanical properties of metal–organic frameworks. *Chem. Sci.* **2019**, *10*, 10666.
8. S. Henke, *et al.*, Directing the Breathing Behavior of Pillared-Layered Metal–Organic Frameworks via a Systematic Library of Functionalized Linkers Bearing Flexible Substituents. *J. Am. Chem. Soc.* **2012**, *134*, 9464.
9. M. Inukai, *et al.*, Storage of CO_2 into Porous Coordination Polymer Controlled by Molecular Rotor Dynamics. *Angew. Chem., Int. Ed.* **2018**, *57*, 8687.
10. L. Carlucci, *et al.*, Complex Interwoven Polymeric Frames from the Self-Assembly of Silver(I) Cations and Sebaconitrile. *Chem. Eur. J.* **1999**, *5*, 237.
11. L. Carlucci, *et al.*, Three Novel Interpenetrating Diamondoid Networks from Self-Assembly of 1,12-Dodecanedinitrile with Silver(I) Salts. *Chem. Eur. J.* **2002**, *8*, 1520.
12. L. Carlucci, *et al.*, Coordination networks from the self-assembly of silver salts and the linear chain dinitriles $NC(CH_2)_nCN$ (n = 2 to 7): a systematic investigation of the role of counterions and of the increasing length of the spacers. *CrystEngComm* **2002**, *4*, 413.

13. D. Depuydt, *et al.*, Silver-Containing Ionic Liquids with Alkylamine Ligands. *ChemPlusChem* **2013**, *78*, 578.
14. Y. Q. Zheng, *et al.*, Syntheses and crystal structures of new suberato-bridged Mn(II) phen complexes: $\{[Mn(phen)_2]L_{2/2}\}\cdot 2H_2L\cdot 8H_2O$, $\{[Mn(phen)(H_2O)_3]_2L\}L\cdot 2H_2L\cdot 4H_2O$ and $\{[Mn(phen)_2(HL)]_2L\}\cdot H_2L$ (H_2L = $HOOC(CH_2)_6COOH$). *Polyhedron*, **2003**, *22*, 2699.
15. W.-W. He, *et al.*, Liquid-free single-crystal to single-crystal transformations in coordination polymers. *Inorg. Chem. Front.* **2018**, *5*, 279.
16. A. Addison, *et al.*, Synthesis, structure, and spectroscopic properties of copper(II) compounds containing nitrogen-sulphur donor ligands; the crystal and molecular structure of aqua[1,7-bis(N-methylbenzimidazol-2′-yl)-2,6-dithiaheptane]copper(II) perchlorate. *J. Chem. Soc., Dalton Trans.* **1984**, 1349.
17. W. Clegg, *et al.*, Structures of four complexes of copper with N-methylimidazole and chloro ligands. *Acta. Cryst.* **1988**, *C44*, 453-.
18. T. Glowiak & I. Wnek, Pentakis(imidazole)copper(II)Monophenyl Phosphate Tetrahydrate, $[Cu(C_3H_4N_2)_5][P(C_6H_5O)O_3].4H_2O$. *Acta Cryst.* **1985**, *C41*, 324.
19. A. L. Abuhijleha & C. WoodsMononuclear copper (II) salicylate imidazole complexes derived from copper (II) aspirinate. Crystallographic determination of three copper geometries in a unit cell. *Inorg. Chem. Commun*. **2001**, *4*, 119.
20. H. Wang, *et al.*, Bis[pentaimidazolecopper(II)] naphthalene-1,4,5,8-tetracarboxylate trihydrate. *Acta Cryst.* **2006**, *E62*, m2621.
21. C. F. Macrae, *et al.*, Mercury 4.0: from visualization to analysis, design and prediction. *J. Appl. Cryst.* **2020**, *53*, 226.
22. A. Martinelli, *et al.*, Conformational evolution of $TFSI^-$ in protic and aprotic ionic liquids. *J. Raman Spectrosc*. **2011**, *42*, 522.
23. S. Su, *et al.*, Assembling an alkyl rotor to access abrupt and reversible crystalline deformation of a cobalt(II) complex. *Nat. Commun.* **2015**, *6*, 8810.
24. J. Ellena, *et al.*, Temperature-Driven Isosymmetric Reversible Phase Transition of the Hormone Estradiol 17β Valerate. *Cryst. Growth Des.* **2014**, *14*, 5700.

25. C. P. Li & M. Du Role of solvents in coordination supramolecular systems. *Chem. Commun.* **2011**, *47*, 5958.

26. W. Y. Zhang *et al.*, Precise Molecular Design of High-Tc 3D Organic-Inorganic Perovskite Ferroelectric: [MeHdabco]RbI_3 (MeHdabco = N-Methyl-1,4-diazoniabicyclo[2.2.2]octane). *J. Am. Chem. Soc.* **2017**, *139*, 10897.

27. T. V. Hoogerstraete, *et al.*, Crystal structures of low-melting ionic transition-metal complexes with N-alkylimidazole ligands. *CrystEngComm*. **2012**, *14*, 4902.

28. G. M. Sheldrick, *SHELXT* – Integrated space-group and crystal-structure determination. *Acta Crystallogr. Sect. A* **2015**, *71*, 3.

29. O. V. Dolomanov, *et al.*, *OLEX2*: a complete structure solution, refinement and analysis program. *J. Appl. Crystallogr*. **2009**, *42*, 339.

30. K. Fujii, *et al.*, Conformational Equilibrium of Bis(trifluoromethanesulfonyl) Imide Anion of a Room-Temperature Ionic Liquid: Raman Spectroscopic Study and DFT Calculations. *J. Phys. Chem. B* **2006**, *110*, 8179.

31. C. Li, *et al.*, Self-assembly of [2]pseudorotaxanes based on pillar[5]arene and bis(imidazolium) cations. *Chem. Commun.* **2010**, *46*, 9016.

Chapter 5

Enhancement of ionic conductivity by amorphization of three-dimensional coordination polymer

Abstract

Recently, researches on coordination polymer (CP) glasses are changing the impressions that CPs are crystalline solids with high frangibility and low processability. In this work, I report a three-dimensional (3D) CP, $[Cu(NTf_2)_2(bib)_{2.5}]$ (**3**), not only owns reversible crystal-crystal phase transition at low temperature but also shows irreversible solid-liquid and reversible glass-liquid phase transitions at high temperature. **3** has the lowest melting points (T_m) and glass transition temperature (T_g) among all 3D CPs that can melt without decomposition, and they benefit from flexible cationic and anionic skeletons and NTf_2 fluorine atoms. The glass state of **3** (**3g**) shows higher ionic conductivity than **3** in crystalline state.

5-1. Introduction

Coordination polymers (CPs) or metal-organic frameworks (MOFs) are burgeoning in recent two decades through their multiple combinations from the diversity of organic ligands as well as a variety of inorganic metal nodes and tunable structures from dense packing structures to highly porous structures.[1] They have revealed potential applications such as gas adsorbents, heterogeneous catalysts, conductive and magnetic materials.[2-5] Although most CPs are fragile crystalline solids in ambient temperature and pressure,[6] recently CP liquids and glasses have been synthesized by thermal or non-thermal methods.[7] CP glasses may provide another development direction including drug delivering, nuclear waste trapping, proton conduction and gas separation.[8-11]

A melt-quenching method is widely adopted for industrial production of non-metallic glasses, bulk metallic glasses, and polymer glasses.[12] However, CPs that can show the solid-liquid phase transition by a thermal method without decomposition are severely limited, because of the weakness of coordination structures and the vulnerability of organic building units. Zhang el al. synthesized two one-dimensional (1D) CP isomers, α-[Cu(ipim)] and β-[Cu(ipim)] (ipim = 2-isopropylimidazolate), with the melting points (T_m) of 458 K and 419 K, respectively.[13] Horike et al. reported a two-dimensional (2D) Zn CP constructed from the triazolate and phosphate ligands. This CP with T_m = 453 K can convert to a glass by the melt-quenched method.[14] Bennett et al. reported that the glasses of three-dimensional (3D) zeolitic imidazolate frameworks (ZIFs) can be obtained using the melt-quenched method due to their analogous tetrahedral primary building units of SiO_2 and the Zachariasen's Rule.[15] It seems that T_m of CPs increases with increasing the dimensionality of CPs, and the similar rule is found in some nanocrystal systems such as inorganic nanoparticles.[16] At the same time, a majority of 3D CPs that can melt without decomposition is ZIFs and Henke et al. provided a strategy of adjusting the molar ratio of organic ligands in ZIFs to lower T_m, but the effect is limited and T_m is still over 640 K.[17]

Here, I tried to explore a new kind of 3D CP that can be processed into a glass at normal pressure by the melt-quenched method by constructing a 3D CP through flexible

subassemblies. Thanks to highly delocalized charges in fluorinated NTf_2^- anions and the flexibility of both NTf_2^- anions and bib ligands, the cationic 3D CP, $[Cu(NTf_2)_2(bib)_{2.5}]$ (**3**), shows a conversion from crystalline state to glass state by the melt-quenched method, the lowest T_g and T_m among 3D CPs, and higher ionic conductivities compared with the poly-ionic liquids containing the same NTf_2^- anions under the same temperature.[18] Furthermore, this compound provides a new direction for people to design more CP glasses.

5-2. Results and discussion

In order to elucidate the phase transition behaviors of **3**, TG-DTA and DSC measurements were adopted. In the TG-DTA curves (Fig. 5-1(a)), an obvious endothermic peak was observed at DTA curve at 445 K, while no weight loss is found at this temperature. The DSC curve of **3** in the first heating process exhibits an endothermic peak at 445 K with $\Delta H = 40.1$ kJ·mol^{-1} and the T_m is calculated to be 438 K by extrapolated peak onset temperature as shown in Fig. 5-1(b). In the first cooling process, a shift of baseline is observed around 303 K and in the second heating process a concave is found at 309 K, suggesting a typical glass transition.[19] T_g can be calculated from DSC curves and its value is 303 K as shown in Fig. 5-1(b).[20] A glass-forming ability (GFA) can be evaluated using the parameter T_g/T_m and this value is 0.69 for **3**,[21] following the *2/3 law* in the molecular glass formers found by Kauzmann.[22] Furthermore, T_m and T_g are far below than those of 3D ZIF-4, [Zn($C_3N_2H_3$)$_2$] and its derivatives.[23] Furthermore, T_m of **3** is comparable with the 1D CP with the same anion constructed from similar components, {[Ag(en)]·NTf_2} (en = ethylenediamine), whose T_m is 444 K.[24] Therefore, our strategy to encapsulate flexible components into the flexible framework successfully breaks the law that CPs with high structural dimensionality should have high T_m.

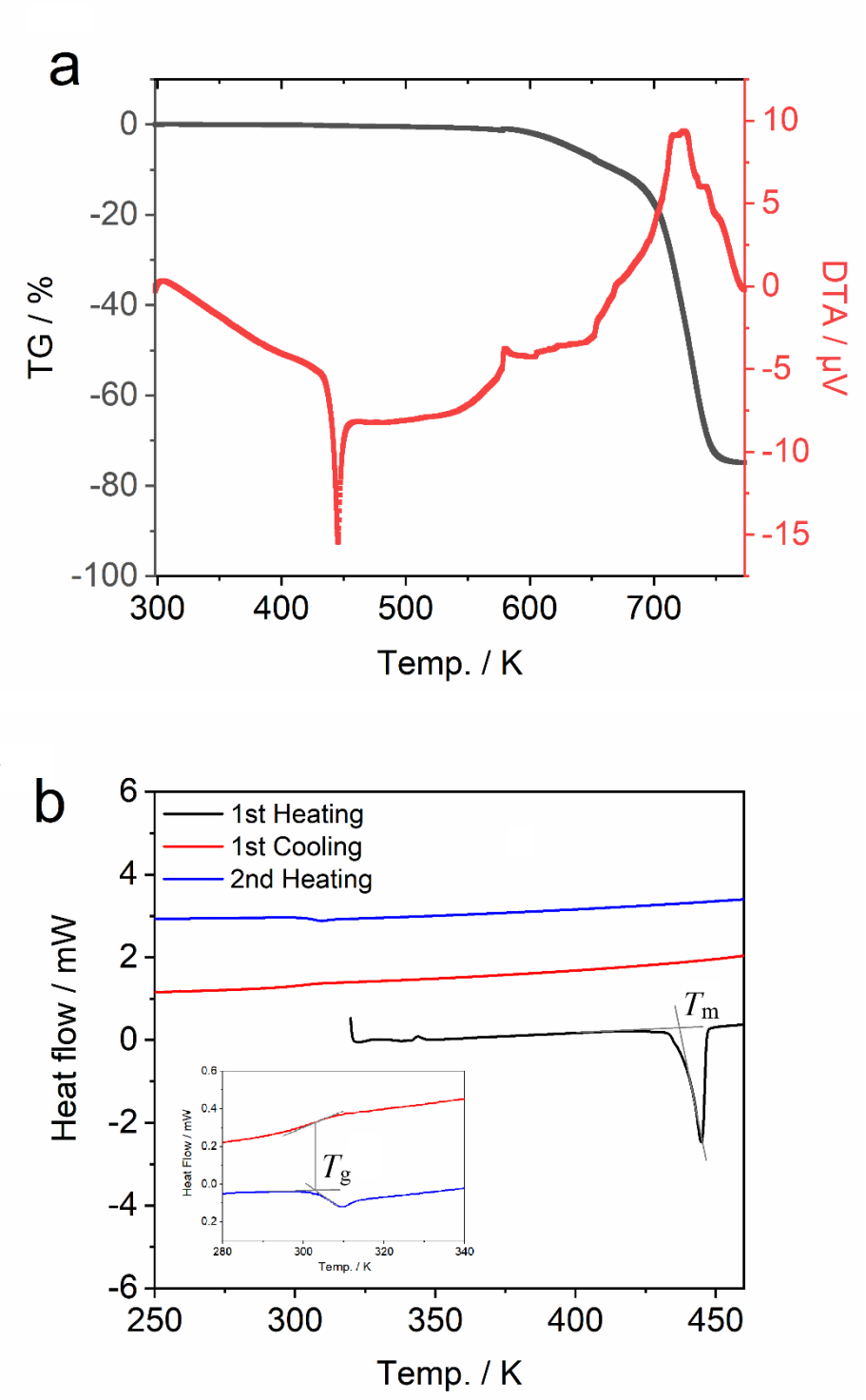

Fig. 5-1. (a) TG-DTA and (b) DSC curves of **3**.

Next, temperature-dependent PXRD patterns were measured to check the assembled structure of **3**. T_m determined by DSC is 438 K, while no diffraction peak is found from the PXRD pattern of **3** at 446 K, implying the melting of crystalline **3**. T_g of **3**

determined by DSC is 303 K, and no diffraction peak is found at 298 K, indicating the formation of CP glass by the melt-quenched method. Therefore, I conclude that the crystalline CP can irreversibly convert to a liquid (denoted as **3l**) on heating and then the reversible liquid-glass phase transition occurs (hereafter, the glass of **3** is denoted as **3g**).

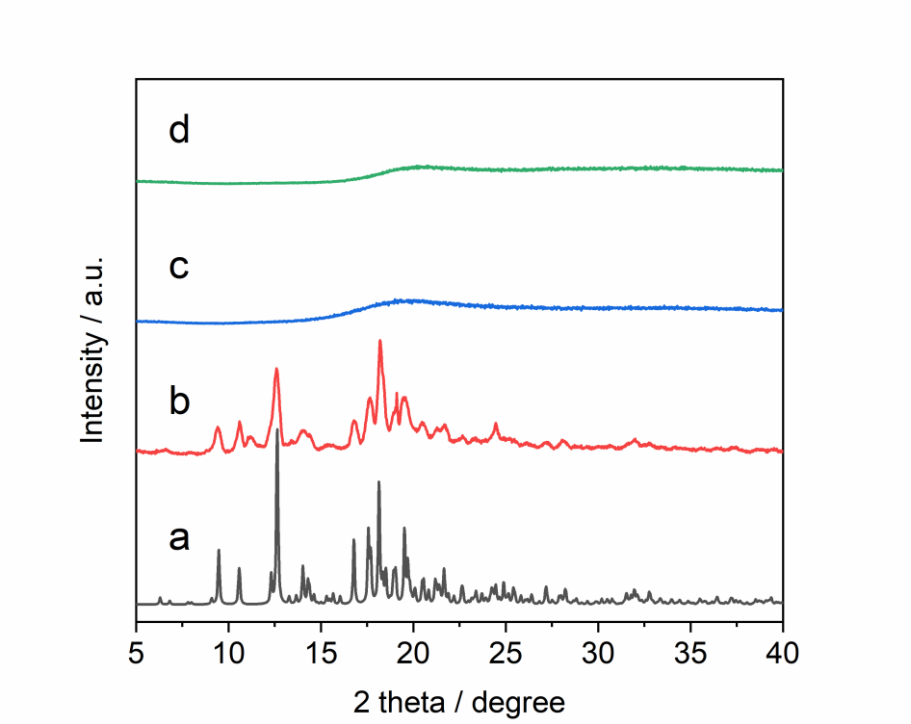

Fig. 5-2. PXRD patterns of (a) simulated **3** at 298 K, (b) as-synthesized **3** at 298 K, (c) **3** after melting at 446 K, and (d) **3g** at 298 K.

FT-IR spectra were employed to investigate whether the NTf_2^- anion and bib ligand in **3** decompose or not after the melt-quenched process. The band at 1351 cm^{-1} is assigned to the asymmetric vibration bands of the NTf_2^- sulfonyl group, while the band at 1130 cm^{-1} is assigned to the symmetric vibration band of the NTf_2^- sulfonyl group. The band at 1170 cm^{-1} is assigned to the symmetric vibration band of the NTf_2^- trifluoromethyl group. The weak peaks at 1460 cm^{-1} and 1610 cm^{-1} are attributed to the C-C and C=C stretching bands of bib ligands, respectively. The peak at 1285 cm^{-1} is attributed to the C-N stretching band of bib ligands. The FT-IR spectra of **3** and **3g** are almost same, reflecting that the bib ligands and NTf_2^- anions remain stable after the

melt-quenching process.

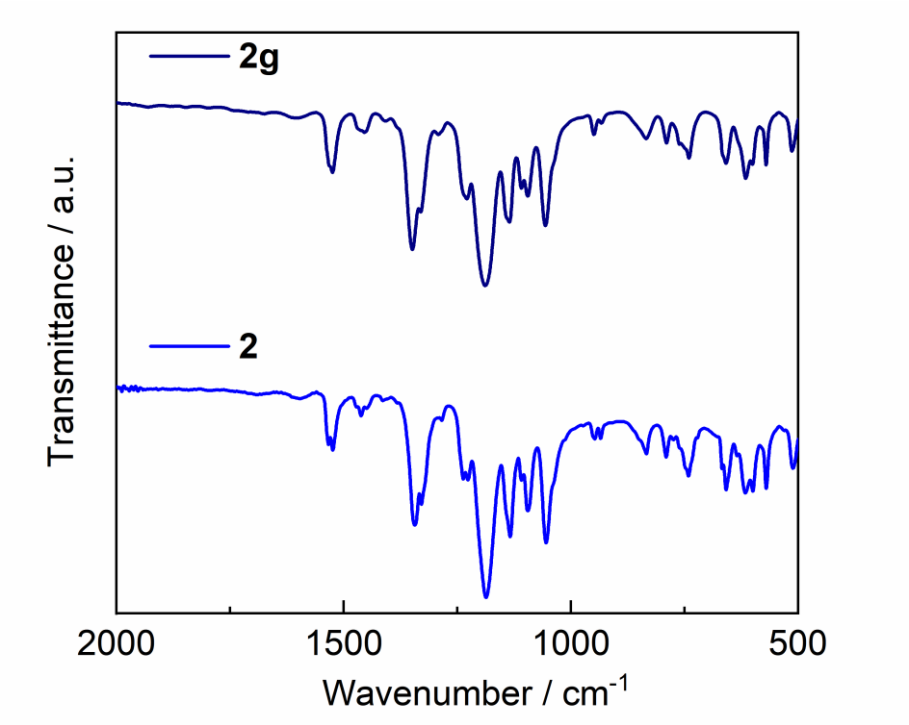

Fig. 5-3. FT-IR spectra of **3** and **3g** at 298 K.

3 and **3g** were investigated by UV-vis spectra to clarify the origin of their distinctly different colors as shown in Fig. 5-4. Broad asymmetric bands are observed around 685 nm in both **3** and **3g** originated from the coordinated Cu(II) ions. This means that the Cu(II) coordination environments of **3** and **3g** are similar to each other. A significant hyperchromic effect is found between **3** and **3g**, in which the absorbance of **3g** around 450 nm is larger than that of **3**. This hyperchromic effect can be explained by the following reason: the NTf_2^- anions are in free form and no longer have weak hydrogen-bonding interactions with the framework.

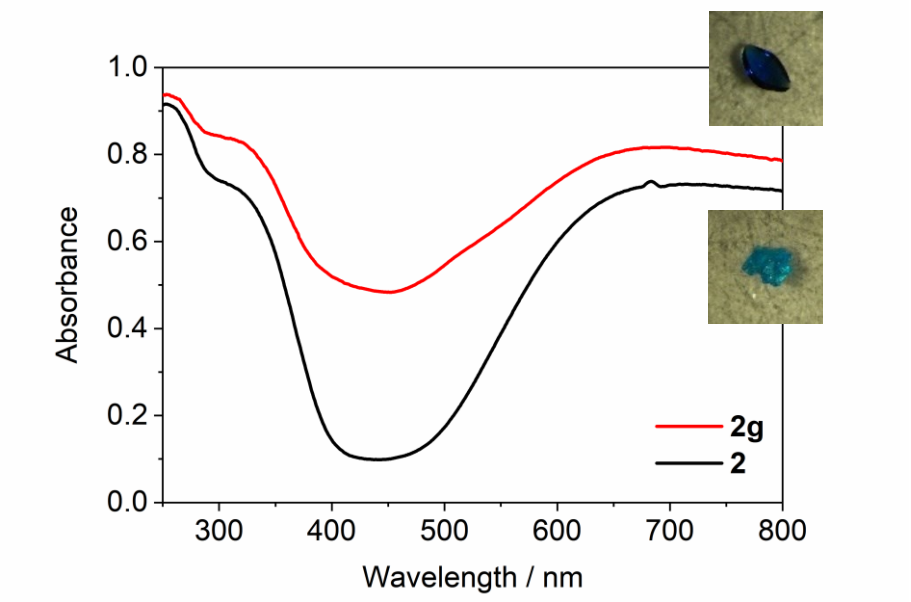

Fig. 5-4. UV-vis spectra of **3** and **3g** in the solid state at 298 K.

XANES spectra are very sensitive to the electronic state and atomic arrangement as shown in Fig. 5-5(a). A shoulder at 8987 eV and an intense band around 8996-9000 eV indicate that only Cu(II) species exists in both **3** and **3g**.[25] Furthermore, the band around 8996-9000 eV splits to two bands due to an unsymmetrical metal-to-ligand bonding.[26] XANES spectra of **3** and **3g** are highly overlapped, implying that **3g** should own the similar to **3** which has unsymmetrical five-coordinated structure. The Cu *K*-edge EXAFS oscillation structures for **3** and **3g** are shown in Fig. 5-5(b). Clear oscillations are observed in the *k* range until 14.0 $Å^{-1}$ for both **3** and **3g**. Almost the same peak positions in **3** and **3g** suggest that the atoms (C and N) around Cu ions in **3** and **3g** should be almost same. At the same time, backscattering amplitudes of EXAFS spectra for **3** and **3g** are highly overlapped, indicating copper ions in **3g** should also coordinate with bib nitrogen atoms. Based on the XANES and EXAFS spectra, I can conclude that the melt-quenched CP glass **3g** owns the same coordination environment around the copper ion (coordination number, distances of coordination bonds, and a kind of coordinated atoms) as **3**. Considering the same coordination environment around the copper ion in **3** and **3g**, flexible polymethylene units in bib ligands and flexible NTf_2^- anions should change their conformations in **3g**.

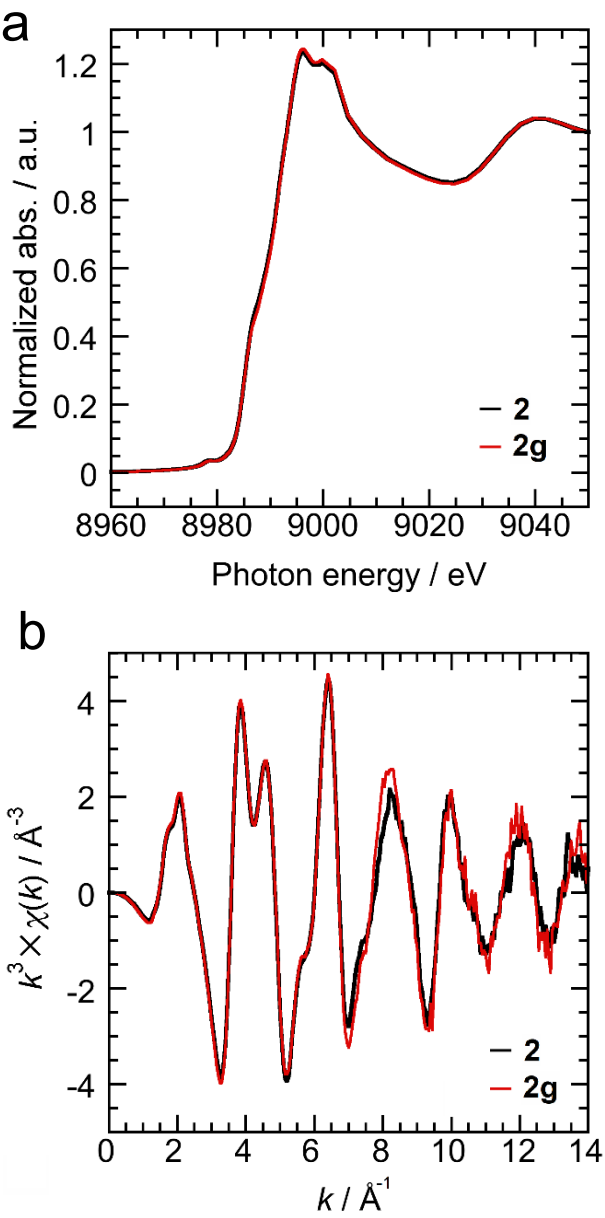

Fig. 5-5. (a) Cu K-edge X-ray adsorption spectra of **3** (black) and **3g** (red) in the X-ray adsorption near edge structure (XANES) region. (b) Extended X-ray adsorption fine structure (EXAFS) oscillations of **3** (black) and **3g** (red).

Thermally induced phase changes occurring in **3** are evaluated using the impedance spectroscopy. The temperature- and frequency-dependent spectra of ε', ε'' from 305 K to 450 K for **3** are shown in Fig. 5-6, and this temperature range involves the crystal-to-liquid phase transition and liquid cooling processes of **3**. In the heating process, ε' and ε'' increase steeply between 431 K and 441 K and reach plateau at the temperature

above 441 K where **3** starts to melt. In the cooling process, both ε' and ε'' gradually decreases with decrease in temperature as shown in Fig. 5-7.

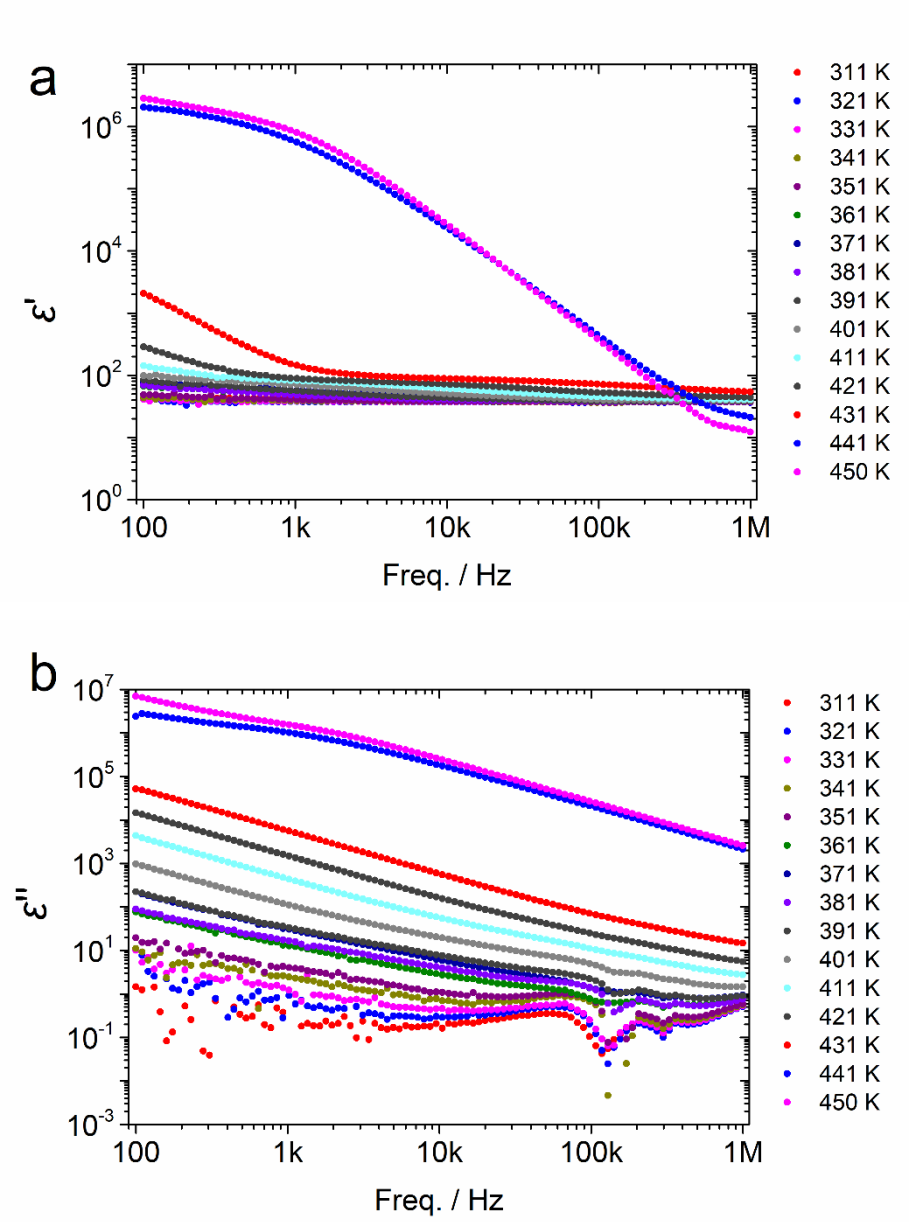

Fig. 5-6 Frequency and temperature dependent real (a) imaginary components (b) dielectric constants of **3** in crystal-to-liquid phase transition.

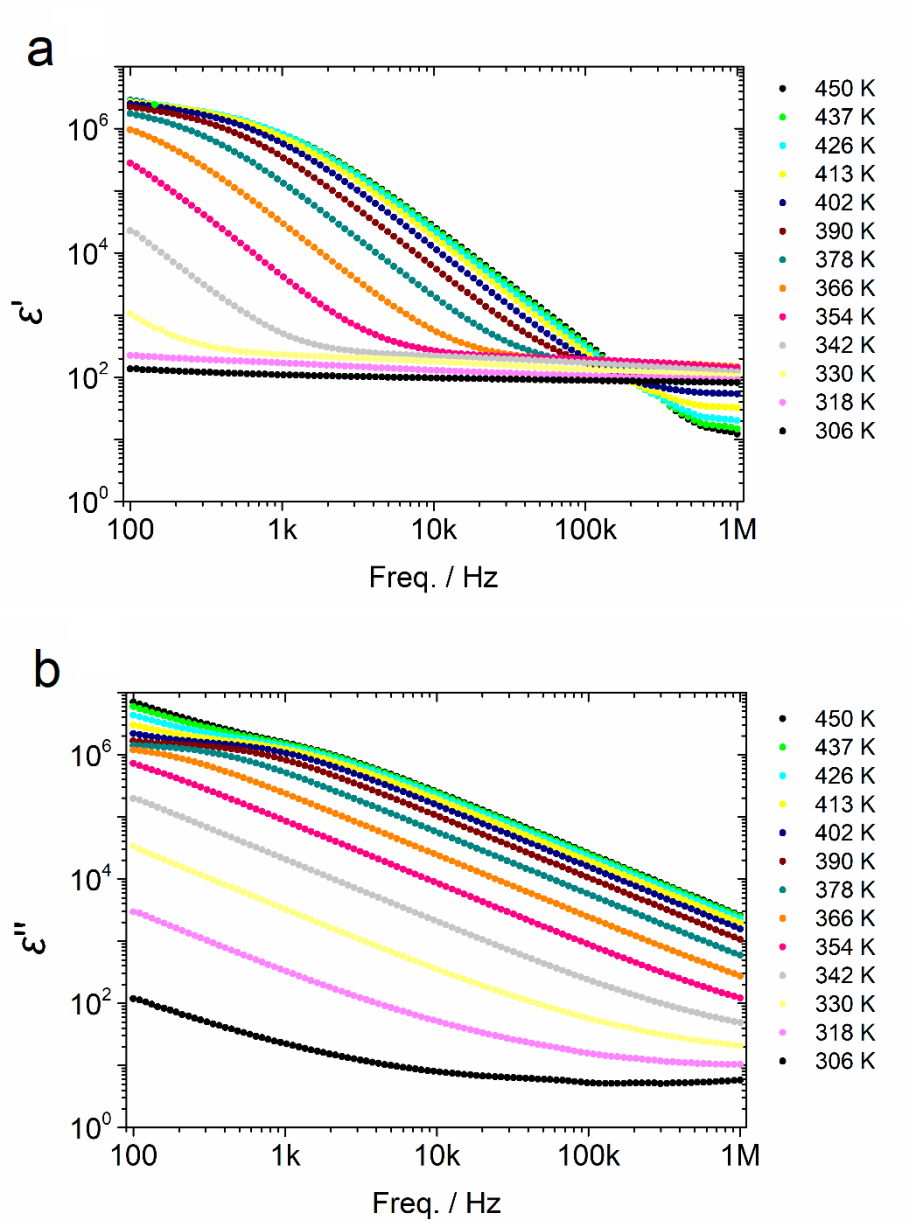

Fig. 5-7 Frequency and temperature dependent real (a), imaginary components (b) dielectric constants of **3** in the cooling process.

Temperature-dependent alternating current conductivity (σ_{ac}) is shown in Fig. 5-8. The σ_{ac} of **3l** is 1.44 mS·cm^{-1} at 450 K, near three orders of magnitude higher than that in crystalline state before melting (3.16 μS·cm^{-1}) at 431 K. Over 441 K, at which **3** melts, σ_{ac} is almost constant at high-frequency region. In the cooling process, σ_{ac} decreases gradually with temperature decreasing.

The dielectric modulus *M*, which is the inverse of the dielectric constant provides

another way to analyze the electrical response of materials, especially to analyze ionic conductivities.[27] Fig. 5-8(c) and (d) show the frequency dependent curves of the imaginary part of dielectric modulus M'' during the heating and cooling processes between 305 K and 450 K.

$$M'' = \frac{\varepsilon''}{\varepsilon'^2 + \varepsilon''^2}$$

One obvious peak is observed at each temperature, and the peak moves to high frequency with temperature increasing, indicating that the NTf_2^- anion result in the ionic conductivity. The peak height of M'' is proportional to the inverse of capacitance (C^{-1}), and the capacitance of **3l** is almost twice higher than that of **3**.

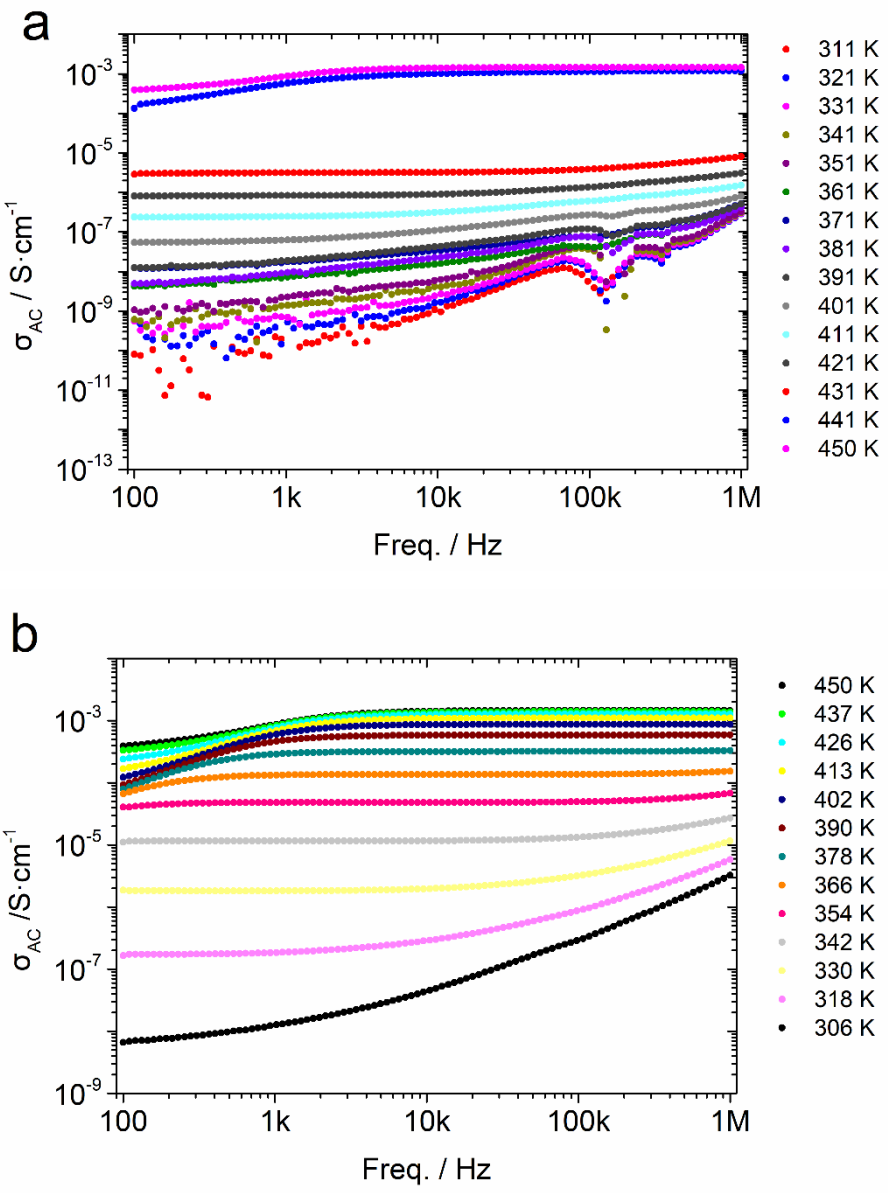

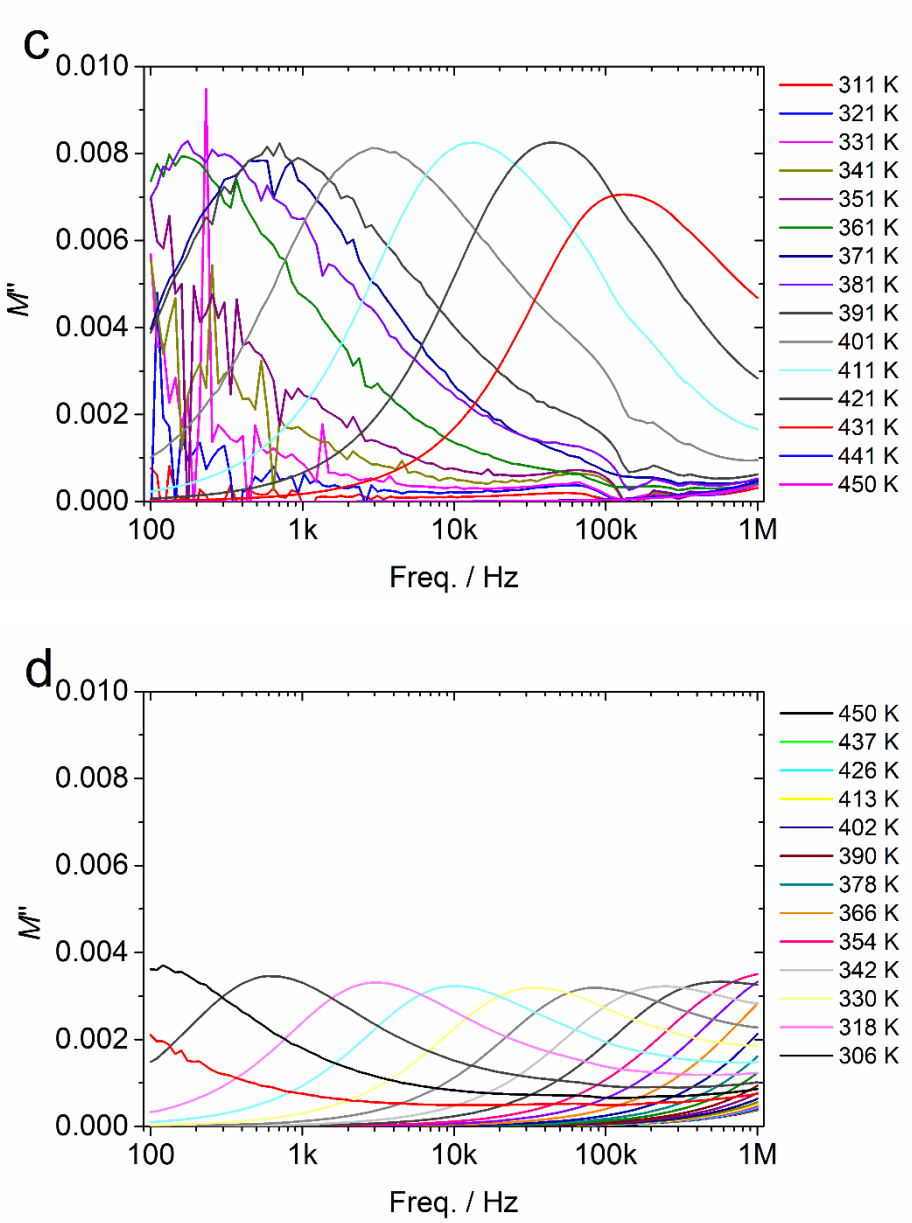

Fig. 5-8. Frequency and temperature dependent σ_{ac} of **3** in (a) crystal-to-liquid phase transition and (b) liquid cooling process. Frequency and temperature dependent M'' of of **3** in (c) crystal-to-liquid process and (d) liquid cooling process

Temperature dependent σ_{ac} is shown in Fig. 5-9(a), and the data are non-Arrhenius distinctly. Vogel-Fulcher-Tamman (VFT) equation is a proper approach to fit the curve shown as following,

$$\sigma_{AC}(T) = Ae^{-\frac{B}{T-T_0}}$$

A is proportional to the concentration of the carrier ions, B is the pseudo activation

energy for the ion conduction, and T_0 is the ideal glass transition temperature, which is an asymptotic value of T_g when heating rate is infinitely tend to zero. T_0 is calculated to be 276 K, lower than T_g calculated by DSC curves.[29]

The activation energy E_a of **3** and **3l** were calculated based on the frequency dependent plots of M'' using the Arrhenius equation shown as the following:

$$f_{\text{top}} = f_0 e^{-\frac{E_a}{k_B T}}$$

where f_{top} is the frequency at the peak of frequency dependent M'', f_0 is a constant related to frequency, E_a is the activation energy of NTf_2^- anions, k_B and T are Boltzmann constant and temperature in kelvin scale, respectively. The calculated activation energies of 1.84 eV and 1.80 eV in **3** and **3l** obtained from the slope of $ln(f_{\text{top}})$ vs. $1000/T$ plots. This result indicates that the mobility of NTf_2^- anions in **3l** is little higher than in crystalline **3**.

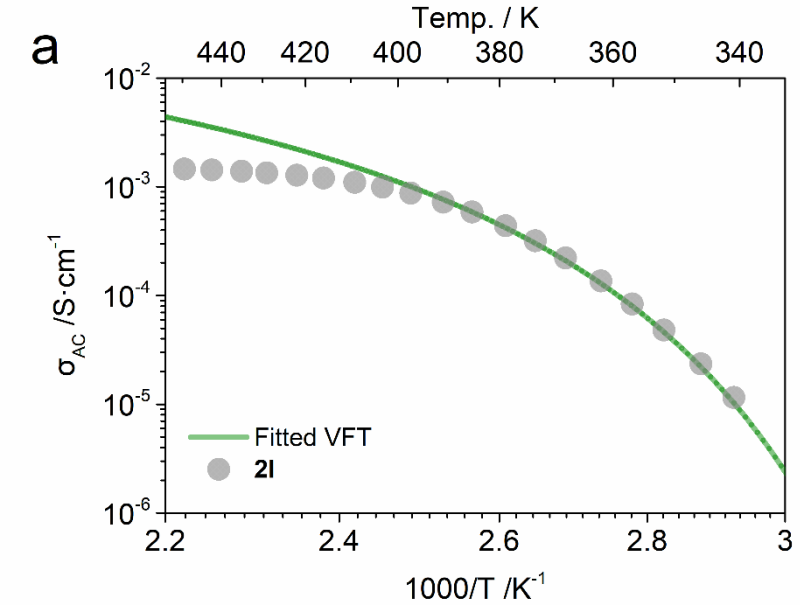

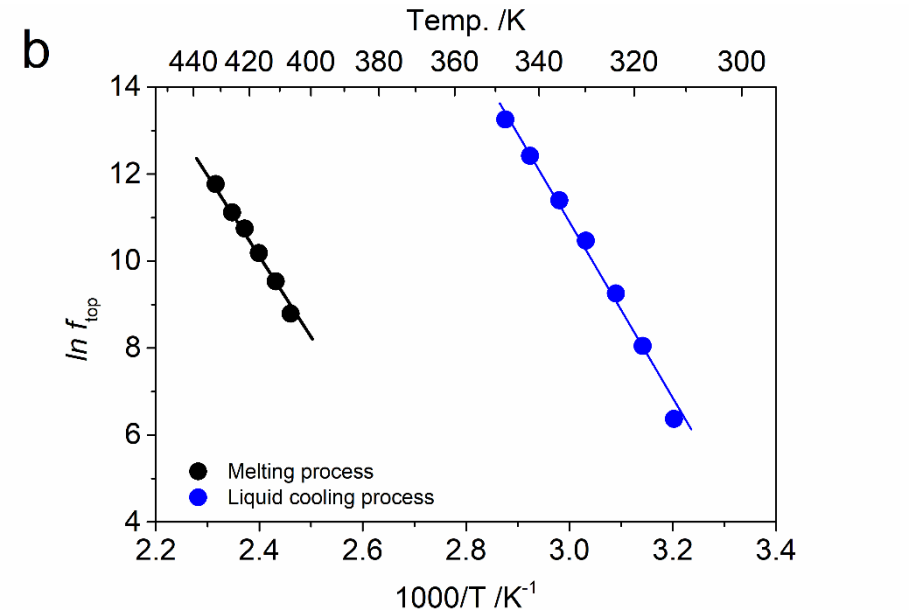

Fig. 5-9. Spectra of temperature-dependent σ_{ac} (a) and $ln(f_{top})$ (b) based on dielectric modulus.

The dielectric properties were also compared between crystalline **3** and **3g**. As shown in Fig. 5-10(a), an obvious gap between 280 K and 290 K is observed from the spectra of the real part of the dielectric permittivity of **3** due to the conformation change of NTf_2^- anions,[30] and no dielectric relaxation is observed in the measured temperature and frequency range (Fig. 5-10(b)), implying that both of bib ligands and NTf_2^- anions cannot move in this frequency range. No dielectric relaxation is observed with temperature higher than 282 K in the measured frequency range, while a dielectric relaxation appears with at the temperature lower than 272 K. This result matched with the ideal glass transition temperature T_0 at 276 K calculated by the VTF equation based on the cooling process of **3l**.

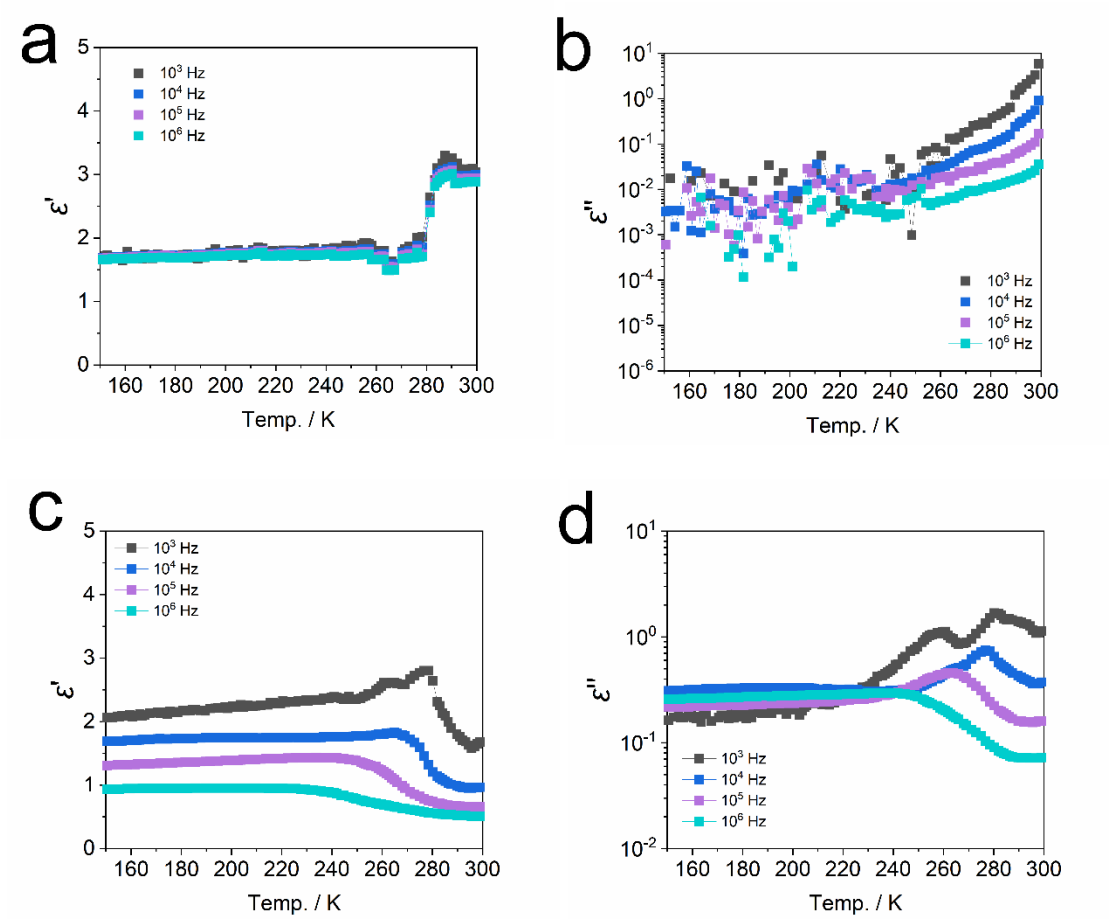

Fig. 5-10. Frequency and temperature dependent real (a), imaginary components (b) dielectric constants of **3**. Frequency and temperature dependent real (c), imaginary components (d) dielectric constants of **3g**.

Ionic conductivity of **3** and **3g** are shown in Fig. 5-11. It is obvious that the ionic conductivity of **3g** is an order of magnitude higher than that of **3** in the same frequency and temperature region. The essential question is what the origin of this significant enhancement of ionic conductivity after amorphization from **3** to **3g**. Based on the characterizations introduced above, I tried to answer this question. The single-crystal structures of **3** have been described in chapter 4: NTf_2^- anions filled in the 3D charged framework constructed by copper ions and bib ligands. The 1D channels were found in the structure of **3** for NTf_2^- anions moving, although the hydrogen bonding interactions restrain the translational move of NTf_2^- anions. After amorphization, the hydrogen bonding interactions between NTf_2^- anions and the framework were weakened proved

by UV-vis spectra and XAS curves, and NTf_2^- anions can move more easily in the framework result in the higher ionic conductivity.

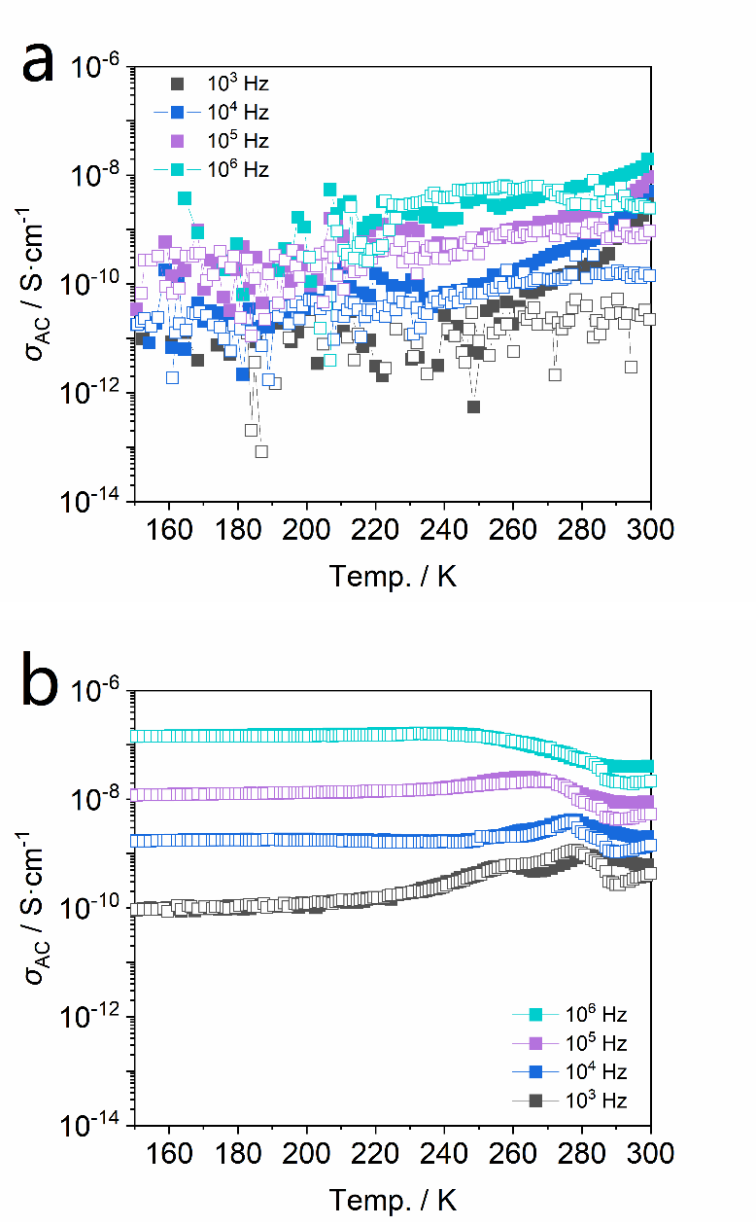

Fig. 5-11. Frequency and temperature dependent σ_{ac} of (a) **3** and (b) **3g**.

Finally, CO_2 adsorption/desorption properties of **3** and **3g** were investigated at 195 K. As shown in Fig. 5-12, both **3** and **3g** have almost no CO_2 adsorption properties. But for **3g**, the behavior like a gate adsorption behavior is observed above P/P_0 = 0.01. I will check the repeatability of this behavior in the future.

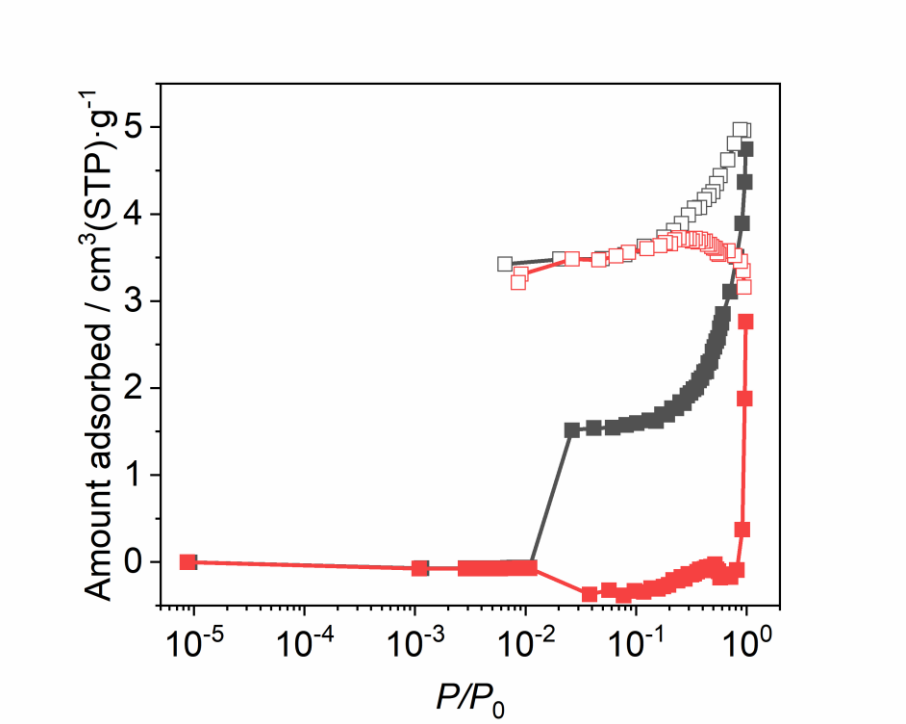

Fig. 5-12. CO_2 adsorption (closed symbols)/desorption (open symbols) isotherms for **3** (red) and **3g** (black) at 195 K.

5-3. Conclusion

I proposed a new strategy to construct a 3D CP glass. **3** owns the lowest T_m and T_g among the reported 3D CPs that can melt without decomposition. Such a superiority helps us to synthesize the CP glass (**3g**) in a relatively gentle condition. Furthermore, **3g** exhibited higher ionic conductivity than **3** in crystalline state. This work not only inspires us to develop more glassy 3D CPs by adopting flexible construction units, but also demonstrates the potential improvement of glassy 3D CPs comparing with traditional crystalline CPs.

5-4. Experimental section

5-4-1. Materials

Commercially available reagents were used as received without further purification. $Cu(NTf_2)_2$ and 1,4-bisimidazole butane (bib) were synthesized using previously described procedures.[30,31]

5-4-2. Synthesis of {[Cu(bib)$_{2.5}$]·2NTf$_2$} (3) in glass state

The synthetic procedure of crystalline **3** is described in chapter 4. Crystalline **3** was heated on the hot plate with a heating rate of 10 K/min until 450 K in ambient, then cooled down to room temperature to obtain **3g**.

5-4-3. Fourier Transform Infrared (FT-IR) spectra

FT-IR spectrum was measured using a Nicolet iS10 FT-IR (Thermo Scientific) equipped with a GladiATRTM accessory with a resolution of 4 cm^{-1} at room temperature.

5-4-4. Powder X-ray diffraction (PXRD) analysis

PXRD patterns were measured using a RINT-Ultima Ⅲ diffractometer (Rigaku) equipped with a TTK 450 low temperature chamber (Anton Paar) with Cu Kα radiation (λ = 1.5418 Å).

5-4-5. Differential scanning calorimetry (DSC)

DSC measurement was carried out with a Q2000 differential scanning calorimeter (TA Instruments) in the temperature range 173-373 K at a heating rate of 10 $K \cdot min^{-1}$ and a cooling rate of 5 $K \cdot min^{-1}$ under a flow of N_2 gas (flow rate 50 $mL \cdot min^{-1}$).

5-4-6. Dielectric measurement

Temperature- and frequency-dependent dielectric constants were measured using a two-probe alternating current (AC) impedance method at a frequency range of 1, 10,

100 and 1000 kHz (an Agilent precision impedance analyzer, 4294A). Two kinds of samples were prepared for the measurements. (1) Single crystals or pellet samples were placed into a cryogenics refrigeration system (Daikin PS24SS). The electrical contacts were prepared using gold paste (Tokuriki 8560) to attach the 10-μm-diameter gold wires to the single crystal. (2) Ground crystals were sandwiched between ITO electrodes to form an arrangement with an electrode area and gap of 50 mm^2 and 1.49 mm, respectively. The sample sandwiched by ITO electrodes was installed in cryostat and temperature was controlled by an ethanol bath with a handy cooler (model 202TCN, As one).

5-4-7. X-ray adsorption spectroscopy (XAS)

Cu K-edge XAS measurement of the samples were performed at BL14B1 station in SPring-8. All data were collected in transmission mode. The XAS samples were prepared by mixing the compounds with boron nitride and then pressing the mixture to obtain pellets. The data were normalized using Athena software.[32]

5-4-8. UV-vis spectroscopy

Adsorption spectra for the thin film samples of **3** and **3g** were measured with a JASCO V-770 UV-vis spectrophotometer.

5-4-9. Gas adsorption isotherm experiments

CO_2 (195 K) adsorption/desorption isotherms were measured by using a BELSORP-max (MicrotracBEL Corp.). Before the measurement, the sample was heated at 373 K in a vacuum for 20 h for activation by BELPREP-vac (MicrotracBEL Corp.).

5-4. References

1. B. Moulton & M. Zaworotko., From Molecules to Crystal Engineering: Supramolecular Isomerism and Polymorphism in Network Solids *Chem. Rev*. **2001**, *101*, 1629.
2. S. Kitagawa, *et al.*, Functional Porous Coordination Polymers *Angew. Chem. Int. Ed.* **2004**, *43*, 2334.
3. J. Lee, *et al.*, Metal–organic framework materials as catalysts *Chem. Soc. Rev.* **2009**, *38*, 1450.
4. D. Sheberla, *et al.*, Conductive MOF Electrodes for Stable Supercapacitors with High Areal Capacitance *Nat. Mater.* **2016**, *16*, 220.
5. G. M. Espallargas & E. Coronado, Magnetic functionalities in MOFs: from the framework to the pore *Chem. Soc. Rev.* **2018**, *47*, 533.
6. Peyman Z. Moghadam, *et al.*, Development of a Cambridge Structural Database Subset: A Collection of Metal–Organic Frameworks for Past, Present, and Future *Chem. Mater.* **2017**, *29*, 2618.
7. T. D. Bennett & S. Horike, Liquid, glass and amorphous solid states of coordination polymers and metal–organic frameworks *Nat. Rev. Mater.* **2018**, *3*, 431.
8. C. O. Tavra, *et al.*, Amorphous metal–organic frameworks for drug delivery *Chem. Comm.* **2015**, *51*, 13878.
9. K. W. Chapman, *et al.*, Trapping Guests within a Nanoporous Metal–Organic Framework through Pressure-Induced Amorphization *J. Am. Chem. Soc.* **2011**, *133*, 18583.
10. W. Chen, *et al.*, Glass Formation of a Coordination Polymer Crystal for Enhanced Proton Conductivity and Material Flexibility *Angew. Chem. Int. Ed.* **2016**, *55*, 5195.
11. Y. Wang, *et al.*, A MOF glass membrane for gas separation. *Angew. Chem. Int. Ed.* **2020**, *59*, 4365.
12. C. A. Angell, Formation of Glasses from Liquids and Biopolymers Science **1995**,

267, 1924.

13. Y. Su, *et al.*, Copper(I) 2-Isopropylimidazolate: Supramolecular Isomerism, Isomerization, and Luminescent Properties *Cryst. Growth Des.* **2015**, *15*, 1735.
14. D. Umeyama, *et al.*, Glass formation via structural fragmentation of a 2D coordination network *Chem. Commun.* **2015**, *51*, 12728.
15. T. D. Bennett, *et al.*, Melt-Quenched Glasses of Metal–Organic Frameworks *J. Am. Chem. Soc.* **2016**, *138*, 3484.
16. H. M. Lu, *et al.*, Size-, Shape-, and Dimensionality-Dependent Melting Temperatures of Nanocrystals *J. Phys. Chem. C* **2009**, *113*, 7598.
17. J. Hou, *et al.*, Halogenated Metal–Organic Framework Glasses and Liquids *J. Am. Chem. Soc.* **2019**, *141*, 12362.
18. H. Chen, *et al.*, Polymerized Ionic Liquids: The Effect of Random Copolymer Composition on Ion Conduction *Macromolecules* **2009**, *42*, 4809.
19. J. K. Cockcroft, *et al.*, Understanding the Structure and Dynamics of Cationic Surfactants from Studies of Pure Solid Phases. *Phys. Chem. Chem. Phys.* **2019**, *21*, 25945.
20. Q. Zheng, *et al.*, Understanding Glass through Differential Scanning Calorimetry *Chem. Rev.* **2019**, *119*, 7848.
21. A. Qiao, *et al.*, A metal-organic framework with ultrahigh glass-forming ability *Sci. Adv.* **4**, eaao6827.
22. W. Kauzmann, The nature of the glassy state and the behavior of liquids at low temperatures, *Chem. Rep.* **1948**, *43*, 219.
23. T. D. Bennett, *et al.*, Melt-Quenched Glasses of Metal–Organic Frameworks *J. Am. Chem. Soc.* **2016**, *138*, 3484.
24. D. Depuydt, *et al.*, Silver-Containing Ionic Liquids with Alkylamine Ligands, *ChemPlusChem* **2013**, *78*, 578.
25. Y. Huang, *et al.*, Catalytic reduction of NO on copper/MCM-41 studied by in situ EXAFS and XANES *Chemosphere*, **2003**, *50*, 1035.
26. C. G. Dodd & G. L. Glen, Chemical Bonding Studies of Silicates and Oxides by

X-Ray K-Emission Spectroscopy *J. Appl. Phys.* **1968**, *39*, 5377.

27. C. A. Angell. Dynamic processes in ionic glasses. Chem. Rev. **1990**, *90*, 523.
28. F. Kremer & A. Schönhals, Broadband Dielectric Spectroscopy. **2003**, Springer, Berlin, Heidelberg
29. T. V. Hoogerstraete, *et al.*, Crystal structures of low-melting ionic transition-metal complexes with N-alkylimidazole ligands. *CrystEngComm*. **2012**, *14*, 4902.
30. K. Fujii, *et al.*, Conformational Equilibrium of Bis(trifluoromethanesulfonyl) Imide Anion of a Room-Temperature Ionic Liquid: Raman Spectroscopic Study and DFT Calculations. *J. Phys. Chem. B* **2006**, *110*, 8179.
31. C. Li, *et al.*, Self-assembly of [2]pseudorotaxanes based on pillar[5]arene and bis(imidazolium) cations. *Chem. Commun.* **2010**, *46*, 9016.
32. B. Ravel, *et al.*, Hephaestus: Data Analysis for X-Ray Adsorption Spectroscopy Using IFEFFIT. *J. Synchrotron Radiat.* **2005**, *12*, 537.

Chapter 6

Decreasing structure dimensionality of a coordination polymer by recombination of coordination environment

Abstract

Although phase/structure transformations in coordination polymers (CPs) have been researched in last two decades, the framework dimensionality basically remained unchanged during such transition processes. Here, a two-dimensional (2D) CP, $\{[Cu(bip)_2(DMSO)_2]\cdot 2NTf_2\}$ (**4**·2DMSO), in which bip is 1,3-bis(imidazole)propane, was found to show an irreversible structure transition from 2D to one-dimensional (1D) after removing coordinated guest DMSO molecules with the cleavage and reformation of coordination bonds. To the best of our knowledge, it is rare to decrease the dimensionality of the CP from 2D to 1D by the recombination of its coordination environment. Furthermore, the desolvated **4** exhibited a reversible solid-to-solid phase transition at 365 K and an irreversible phase transition at 533 K.

6-1. Introduction

Recent years, many CPs with reversible or irreversible solid-to-solid phase/structure transitions have been reported.[1-5] Most of such transitions originate from their flexible metal nodes, flexible bridging ligands, and/or flexible assembled structures,[6-10] and chemists make use of these phase/structure transitions in CPs for gas separation, sensing and catalysis.[11-13]

However, it is difficult for CPs to achieve phase/structure transitions via reconnecting their coordination bonds, because it is easy for CPs to resolve themselves into the disordered state after breaking the coordination bonds.[14,15] Recently, some researchers tried to break coordination bonds in CPs and introduce monodentate carboxylic acid to construct defects in the frameworks.[16-20] These defective CPs showed higher surface area and larger pore sizes. A few examples are reported that the CPs can change their framework dimensionalities by the recombination of their coordination environments. Kondo et al. synthesized the 2D CP, ELM-11 ($[Cu(BF_4)_2(4,4'\text{-bpy})_2]$, bpy = 4,4′-bipyridine) from another CP, pre-ELM-11, ($\{[Cu(BF_4)_2(4,4'\text{-bpy})(H_2O)_2]\cdot 4,4'\text{-bpy}\}$) with the 1D framework by removing the coordinated water molecules.[21] In pre-ELM-11, each copper ion coordinates with two 4,4′-bpy ligands, two water molecules, and two BF_4^- anions, and the rest 4,4′-bpy ligands have the hydrogen bonding interactions with coordinated water molecules. After dehydration, coordinated water molecules are totally removed and the originally uncoordinated 4,4′-bpy ligands coordinate to copper ions, resulting in the conversion from the 1D chain to the 2D layer. It is worth noting that during the structural transition from pre-ELM-11 to ELM-11, the cleavage of Cu-H_2O coordination bonds and the formation of Cu-4,4′-bpy coordination bonds are observed. This 1D to 2D structural transition is reversible and the rehydration occurs to form the original 1D pre-ELM-11.[22]

Here, I synthesized the 2D CP, $\{[Cu(bip)_2(DMSO)_2]\cdot 2NTf_2\}$ (**4**·2DMSO) constructed from flexible components. This 2D CP can convert to a 1D structure after removing coordinated DMSO molecules. Different from ELM-11, the bridging ligands in **4**·2DMSO is a kind of bi-imidazole ligands, and an imidazole is more basic than a

pyridine because six electrons are delocalized on five atoms, resulting in higher electron density and stronger coordination bonds between imidazole groups and metal ions.[23] Therefore, it is a challenge to disconnect coordination bonds between imidazole groups and metal ions. The coordination of anions to metal centers can hinder the delocalization of positive charge over other bridging ligands and weaken the coordination bonds.[24] The coordination between NTf_2^- anions and cooper ions will weaken the coordination bonds between the bridging ligands and copper ions for the recombination of coordination environment.

6-2. Results and discussion

The structure of the blue crystal **4**·2DMSO was determined using a single-crystal XRD analysis. One copper ion coordinates with four bip ligands at an equatorial plane and two DMSO molecules at axial sites as shown in Fig. 6-1(a). The distances between the copper ion and DMSO molecules (Cu-O1 = 2.505(1) Å, and Cu-O2 = 2.555(8) Å) are much longer than those between the copper ion and the bip ligands (Cu–N1 = 2.014(8) Å, Cu–N2 = 2.022(8) Å, Cu–N3 = 2.029(6) Å, Cu–N4 = 1.994(9) Å) due to a Jahn-Teller distortion. Two crystallographically independent NTf_2^- anions are coordination-free in *trans* conformation and do not have any hydrogen bonding interactions with DMSO molecules or bip ligands. The bib ligands bridge the copper ions to form an undulating 2D layer as shown in Fig. 6-1(b) and (c), and the polymethylene chains of bip ligands in **4**·2DMSO are in *trans-trans* (*TT*) conformation. The distance between the neighboring 2D layers is 8.8 Å, and the distance between two neighboring copper ions within the 2D layer is 12.3 Å. Although the 2D layers are orderly arranged to form 1D distorted square prism tunnels as shown in Fig. 6-1(d), NTf_2^- anions are not located in such tunnels but plugged between the undulating 2D layers as shown in Fig. 6-1(b). At the same time, coordinated DMSO molecules lie in the tunnels.

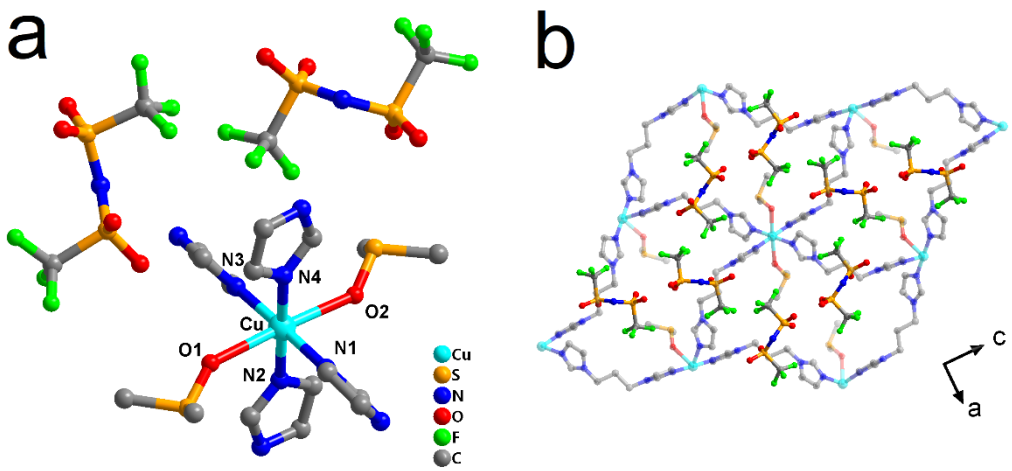

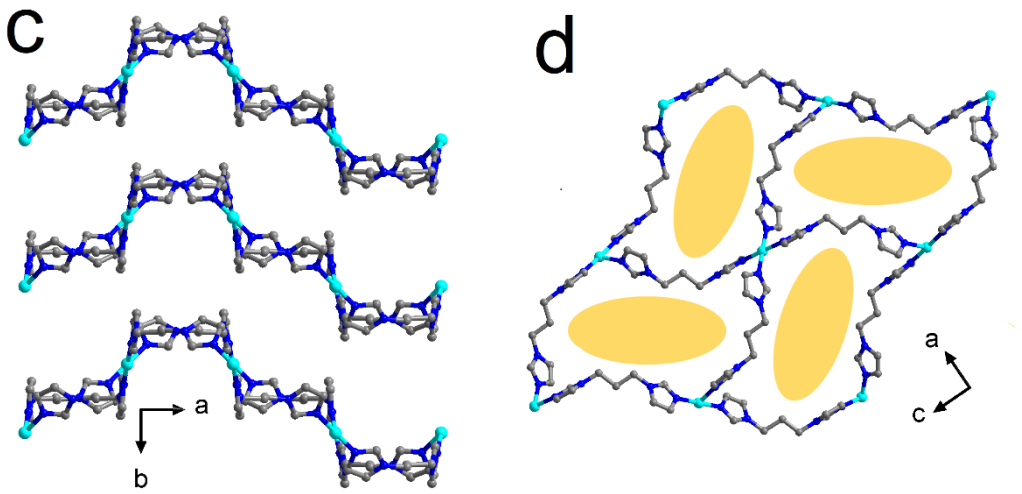

Fig. 6-1. Crystal structure of **4**·2DMSO. (a) Coordination environment around the copper center; (b) undulating 2D layer viewed along the *b* axis; (c) packing structure of undulating 2D layers viewed along the *c* axis, in which NTf_2^- anions and coordinated DMSO molecules are omitted; (d) 1D distorted square prism tunnel structure viewed along the *b* axis, in which NTf_2^- anions and coordinated DMSO molecules are omitted. In all figures, hydrogen atoms are omitted for clarity.

Thermal properties of **4**·2DMSO were investigated by TG-DTA. As shown in Fig. 6-2, an obvious weight loss (13.3 %) caused by the removal of coordinated DMSO molecules is observed from 357 to 410 K and corresponds to 1.9 mol of DMSO per 1 mol of copper ion, nearly matching with the chemical formula determined by the single-crystal XRD analysis. Furthermore, a small endothermic peak is observed at 550 K from the DTA curve, while there is no weight loss on the TG curve around its temperature, implying that a phase transition may occur at this temperature.

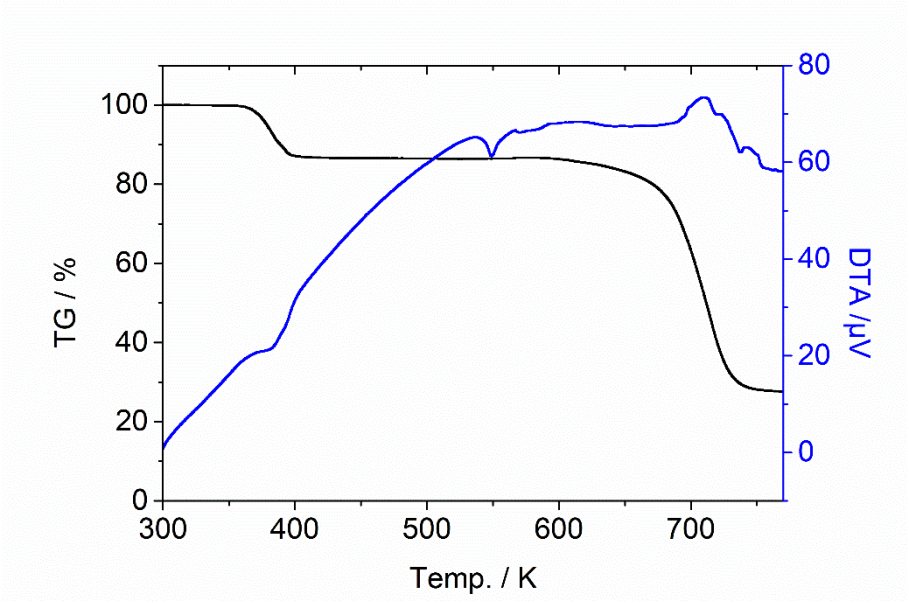

Fig. 6-2. TG-DTA curves of **4**·2DMSO from room temperature to 773 K.

Next, in order to check the structure after removal of guest DMSO molecules, FT-IR spectra were measured for **4**·2DMSO and the desolvated **4** obtained by heating **4**·2DMSO at 373 K for 6 hours. As shown in Fig. 6-3, the as-synthesized sample **4**·2DMSO has the band at 1019 cm^{-1} assigned to the symmetric vibration band of DMSO sulfonyl group, while this peak is disappeared in the desolvated **4**, indicating the complete desolvation of coordinated DMSO molecules. At the same time, the asymmetric vibration band of sulfonyl group originated from NTf_2^- anions shifts to lower wavenumber (from 1335 (**4**·2DMSO) to 1316 cm^{-1} (**4**)), while the symmetric vibration band of NTf_2^- sulfonyl group shifts to higher wavenumber (from 1050 (**4**·2DMSO) to 1062 cm^{-1} (**4**)), suggesting that the environment around the NTf_2^- anion may be changed after removing coordinated DMSO molecules.

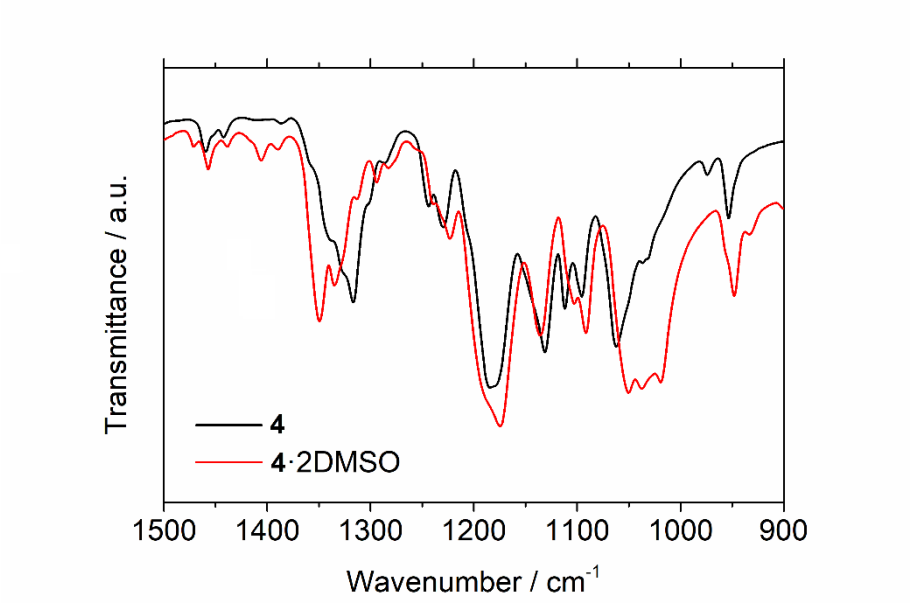

Fig. 6-3. FT-IR spectra of as-synthesized **4**·2DMSO and **4**.

PXRD patterns of **4**·2DMSO before and after desolvation are shown in Fig. 6-4. The PXRD pattern of **4**·2DMSO is similar but not completely match with the simulated pattern probably because the measured temperature (room temperature) is different from the temperature (173 K) at which the crystal structure of **4**·2DMSO is determined. After desolvation, a totally different PXRD pattern is obtained, implying that the desolvated **4** should have a totally different structure. It is difficult to determine the exact crystal structure using the crystal obtained by heating the crystal of **4**·2DMSO because of a loss of single crystallinity. Therefore, I tried to directly synthesize the single crystal of **4** without any guest molecules and succeeded in yielding it in H_2O-MeOH solvent condition.

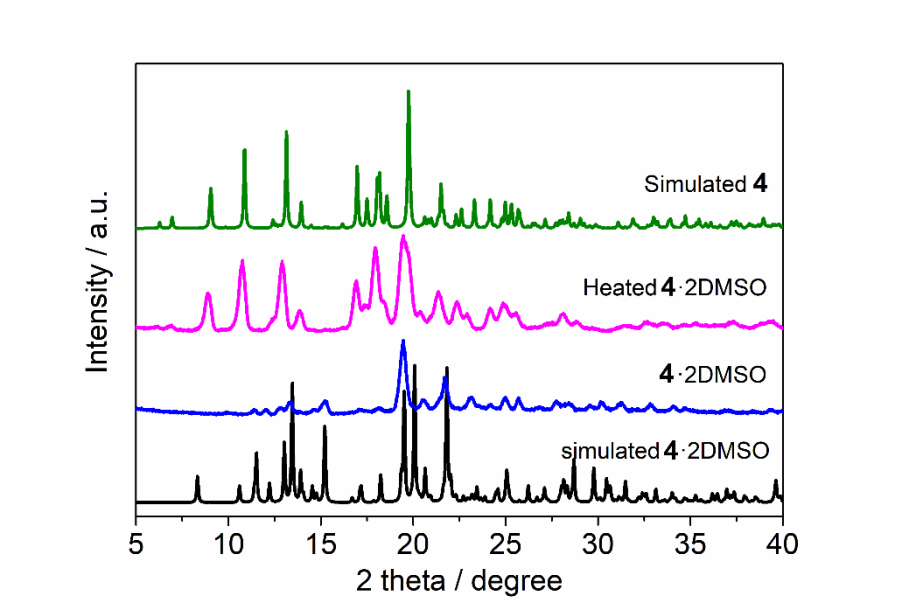

Fig. 6-4. PXRD patterns of simulated **4**·2DMSO, as-synthesized **4**·2DMSO, heated **4**·2DMSO and simulated **4**.

The crystal structure of **4** was characterized using a single-crystal XRD analysis. One copper ion coordinates with four bip ligands and two NTf_2^- anions as shown in Fig. 6-5(a). The distances between the copper ion and NTf_2^- anions (Cu-O1 = 2.699(3) Å and Cu-O2 = 2.583(3) Å) are much longer than those between the copper ion and the bip ligands (Cu–N1 = 1.982(5) Å, Cu–N2 = 1.991(4) Å, Cu–N3 = 2.029(6) Å, Cu–N4 = 1.962(4) Å) due to a Jahn-Teller distortion and the weaker coordination ability of NTf_2^- anions. The bip ligands bridge the copper ion to form the 1D doubly linked chain with a toroidal space of 5.7 Å × 9.6 Å as shown in Fig. 6-5(b). The distance between two neighboring 1D chains is 10.4 Å. The conformation of polymethylene chains of bip ligands in **4** changes from *TT* to *gauche-trans* (*GT*) conformation, while all NTf_2^- anions are still in *trans* conformation. Different from CP **1** introduced in Chapter 2, the 1D chains in **4** do not assemble to the quasi 2D layer but remain in a relatively independent 1D chain structure (Fig. 6-5(c)). In CP **1**, NTf_2^- anions do not have any intrachain hydrogen-bonding interaction, and they form weak hydrogen bonding interactions with the neighboring 1D chains. However, in CP **4**, because the orientation of NTf_2^- anions is parallel to the 1D chains, intrachain hydrogen-bonding interactions

between NTf_2^- anions and bip ligands are found. There are two kinds of weak intrachain hydrogen-bonding interactions (Fig. 6-5(d)); one is observed between the NTf_2^- fluorine atom and the bip methylene hydrogen atom with F9•••H15 = 2.625(4) Å, F9•••C8 = 3.453(6) Å, and F9•••H15-C8 = 143.3(3) °. The other is between another NTf_2^- fluorine atom and the bip imidazole hydrogen atom with F19•••H7 = 2.769(4) Å, F19•••C17 = 3.508(7) Å, and F19••• H7-C17 = 137.1(3) °. Therefore, a small void space surrounded by bip ligands and NTf_2^- anions is found with a radius of 0.7 Å as shown in Fig. 6-5(d).

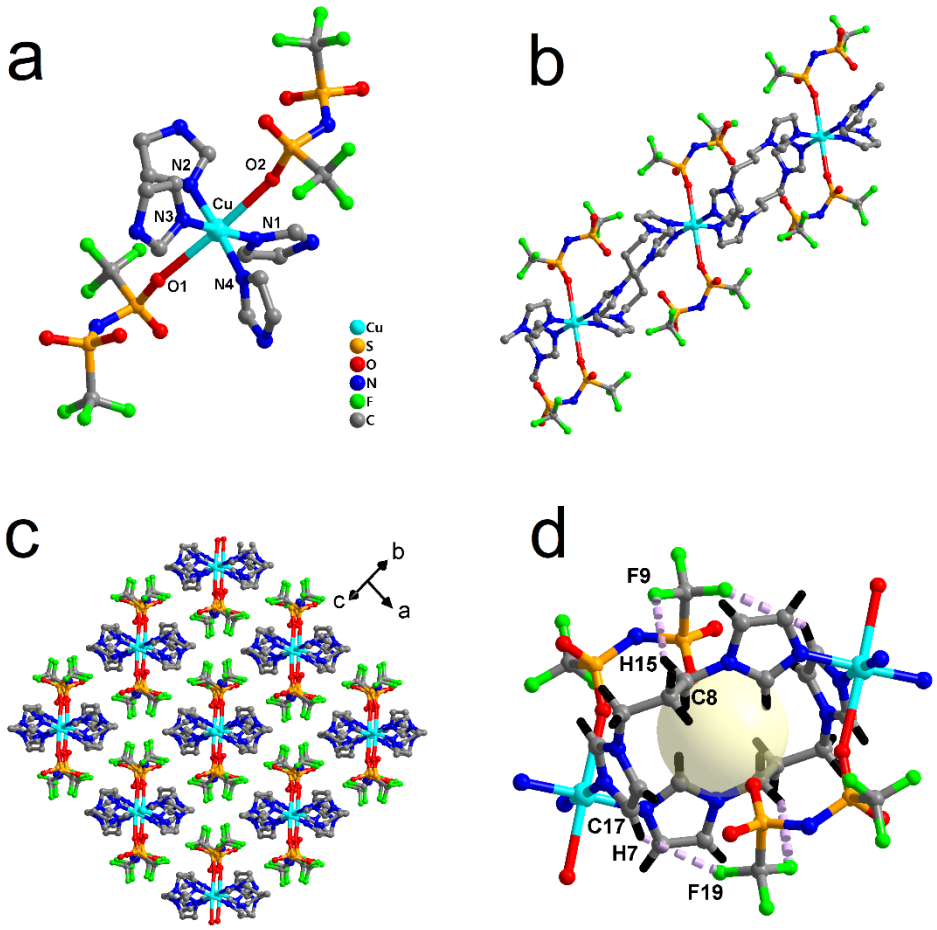

Fig. 6-5 Crystal structures of **4**. (a) Coordination environment around the copper center; (b) 1D doubly linked chain; (c) packing structure of 1D doubly linked chains; (d) view of the intrachain hydrogen-bonding interactions and small void space. In all figures, hydrogen atoms are omitted for clarity.

4 was exposed to DMSO vapor for 6 days to evaluate the reversibility of the structural transition between **4** and **4**·2DMSO. The PXRD pattern of the sample exposed to a DMSO vapor is very similar to **4** (Fig. 6-6), implying that it is difficult for **4** to convert to **4**·2DMSO again.

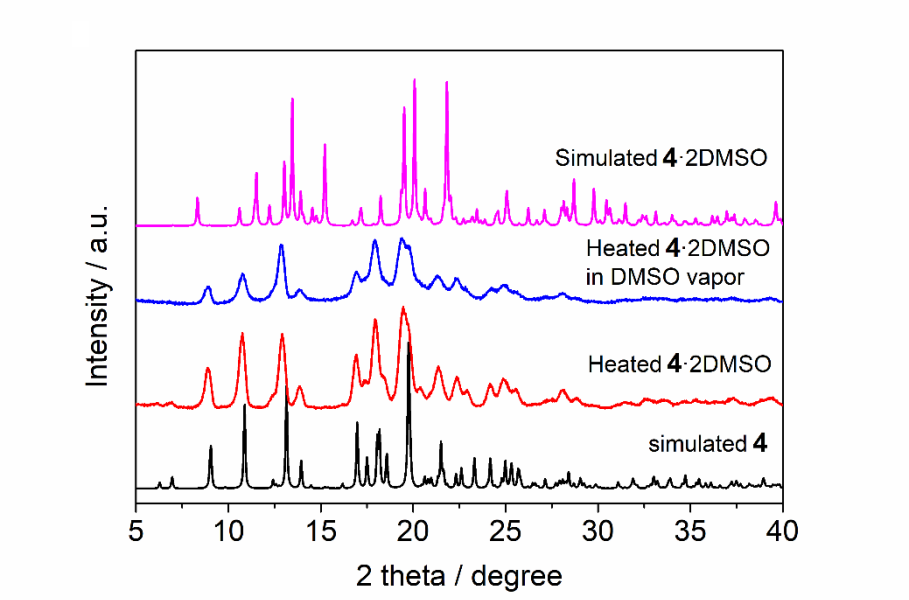

Fig. 6-6. PXRD patterns of simulated **4**, heated **4**·2DMSO, **4**·exposed to a DMSO vapor and simulated **4**·2DMSO.

CO_2 adsorption properties of **4**·2DMSO and **4** were investigated at 195 K as shown in Fig. 6-7. Compared with **1** that showed a typical gate-adsorption behavior, both **4**·2DMSO and **4** have no CO_2 adsorption properties at 195 K until $P/P_0 = 0.99$.

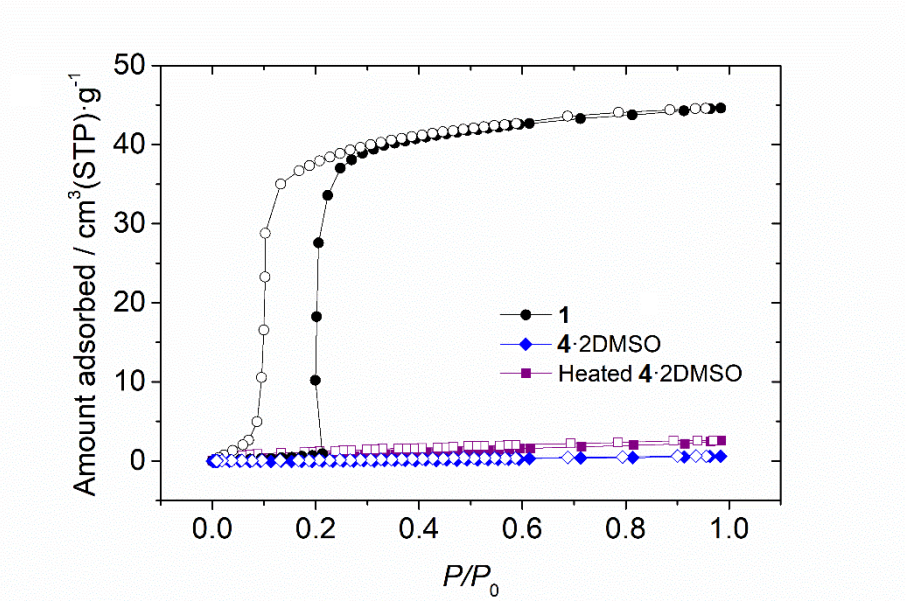

Fig. 6-7. CO_2 adsorption/desorption isotherms of **1**, **4**·2DMSO, and **4** at 195 K.

TG-DTA and DSC measurements were measured to explore the phase transition properties of **4**. As shown in Fig. 6-8(a), an endothermic peak is found at 533 K from the DTA curve, similar to **4**·2DMSO, while there is no weight loss on the TG curve around its temperature. The DSC curves evidence another reversible phase transition at 365 K in the heating process and 348 K in the cooling process (Fig. 6-8(b)), although no endothermic peak was found on DTA curve. These results suggest that **4** is an interesting phase transformable material and further evaluation is in progress.

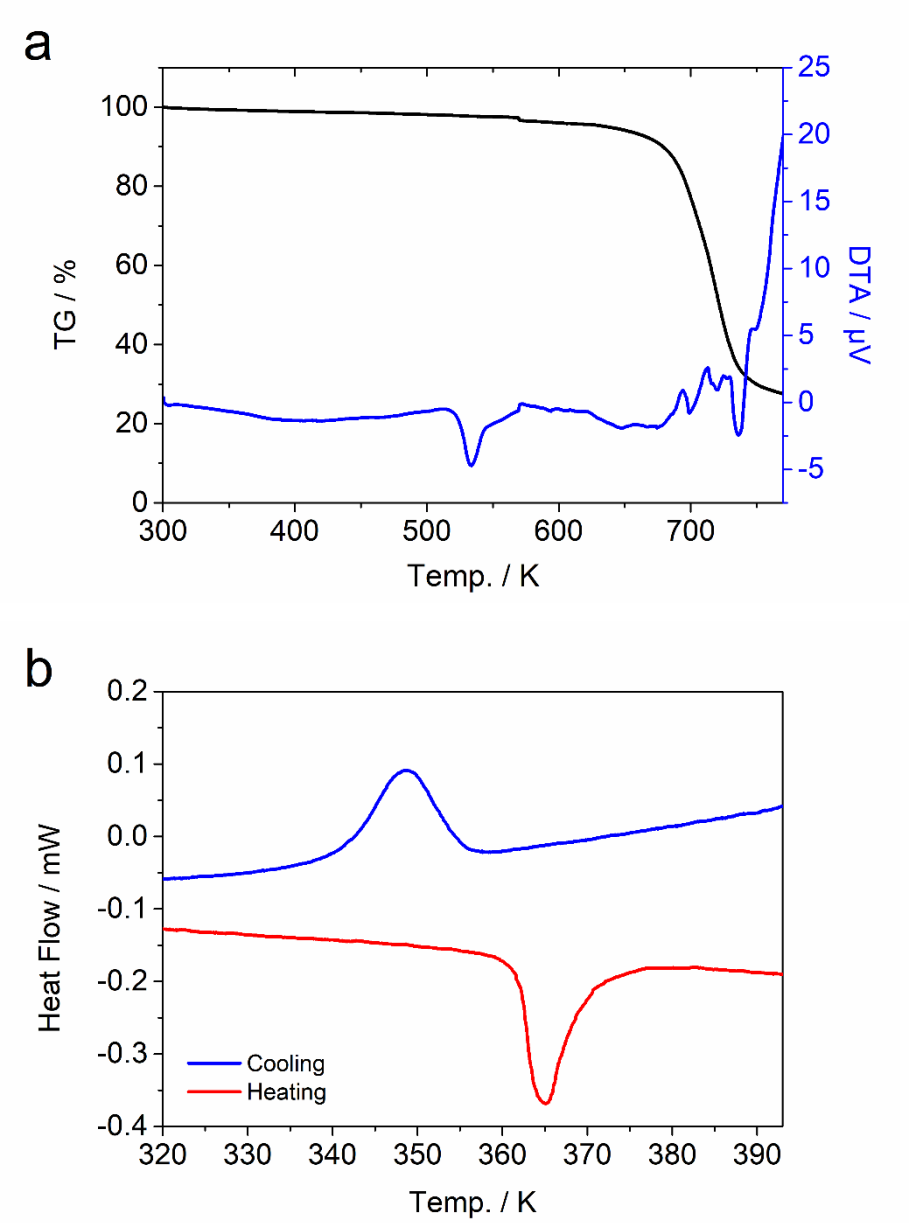

Fig. 6-8. (a) TG-DTA and (b) DSC curves of **4**.

Here, I discuss the irreversible structural transition from **4**·2DMSO to **4** using Fig. 6-9. In **4**·2DMSO, the NTf_2^- anions containing highly delocalized negative charges are introduced to the 2D framework as counter anions and there is no interaction between NTf_2^- anions and the 2D framework. During the desolvation process, DMSO molecules are removed with the cleavage of copper-DMSO coordination bonds to form open copper sites. Then, the NTf_2^- anions coordinate to these open copper sites instead of DMSO. At the same time, the cleavage and reformation of coordination bonds formed

between the copper ions and imidazoles of bip should occur to convert from the 2D to 1D framework. The coordination between NTf_2^- anions and cooper ions weakens the coordination bonds between the bip ligands and copper ions, probably causing the recombination of copper-bib coordination bonds. The change in the structural dimensionality is also supported by the conformational change of bip ligand from *TT* to *GT*. However, in contrast to pre-ELM-11, this structural transition is not reversible, probably because of stable 1D structure supported by the intrachain hydrogen bonds between the NTf_2^- anions and bip ligands.

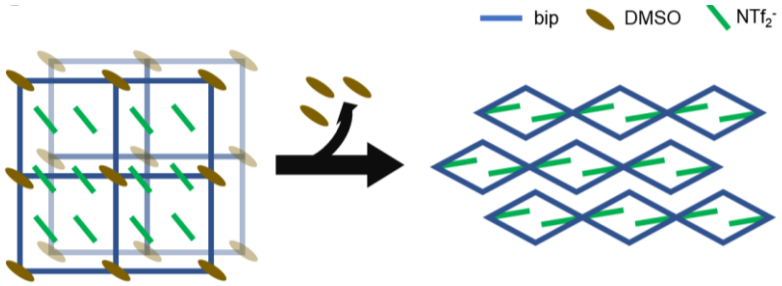

Fig. 6-9. Schematic view of the structural transition from **4**·2DMSO to **4**.

6-3. Conclusion

I have successfully synthesized the 2D CP **4**·2DMSO, which exhibits an irreversible structural transition from 2D to 1D by the recombination of coordination environment. The coordination bonds between NTf_2^- anions and copper ions should be the key for this structural transition. Furthermore, the different arrangement of NTf_2^- anions between **1** and **4** influences CO_2 adsorption behavior. Additional studies on this compound will center on the elucidation of thermally induced phase transition behaviors of the desolvated **4**.

6-4. Experimental section

6-4-1. Materials

Commercially available reagents were used as received without further purification. $Cu(NTf_2)_2$ and 1,3-bis(imidazole)propane (bip) were synthesized using previously described procedures.[26,27]

6-4-2. Synthesis of 4·2DMSO and 4

Single-crystal samples of **4**·2DMSO and **4** were prepared by using a diffusion method in the straight glass tube containing a bottom layer of 0.1 M aqueous $Cu(NTf_2)_2$, a middle layer of 1:1 water and MeOH/DMSO, and a top layer of 0.2 M bpp in MeOH/DMSO. After 2 weeks, the formed transparent and rod like blue/bpurple single crystals were separated by filtration, washed with water, and dried in the atmosphere.

6-4-3. Crystal structure determination

Crystal data were collected on a RIGAKU RAXIS-RAPID imaging-plate diffractometer with a graphite-monochromated Mo-Kα radiation (λ = 0.71075 Å) and a Rigaku Micro Max-007 HF diffractometer and a Pilatus 200 K detector with Cu Kα radiation (λ = 1.54184 Å). The structures were solved by using direct method (SHELXT) and refined by using full-matrix least-squares techniques on F^2 using SHELXL-2018 (ver. 2018/3). All non-hydrogen atoms were refined anisotropically. Hydrogen atoms were located at geometrically calculated positions and refined using a riding model. Olex2 was used as a graphical user interface. The crystallographic data of the crystals **4**·2DMSO and **4** are shown in Table 6-1.

Table 6-1. The crystallographic data of the crystals **4**·2DMSO and **4**.

	4·2DMSO	**4**
Chemical Formula	$\{[Cu(bip)_2(DMSO)_2]\cdot 2NTf_2\}$	$[Cu(NTf_2)_2(bip)_2]$
Empirical formula	$CuC_{26}H_{36}N_{10}O_{10}F_{12}S_6$	$CuC_{22}H_{24}N_{10}O_8F_{12}S_4$
Formula weight	1132.548	976.279
Crystal system	Cubic	Triclinic
Space group	$Pca2_1$	$P1$-
Temperature / K	173	173
a / Å	25.187(3)	10.3932(4)
b / Å	8.8407(9)	13.1469(6)
c / Å	19.6816(16)	14.3110(5)
α / °	90	90.688(3)
β / °	90	101.272(3)
γ / °	90	104.885(4)
V / Å^3	4382.6(7)	1849.36(13)
Z	2	4
GOF on F^2	1.037	1.009
R_1 $[I > 2\sigma(I)]$[a]	0.0907	0.0661
R_w $[I > 2\sigma(I)]$[b]	0.2320	0.1478

[a]$R_1 = \sum||F_o| - |F_c||/\sum|F_o|$. [b]$R_w = [(\sum w(|F_o|^2 - |F_c|^2)^2)/\sum w(F_o^2)^2]^{1/2}$.

6-4-4. Thermogravimetric differential thermal analysis (TG-DTA)

TG-DTA curves was measured by using a ThermoPlus2/TG-DTA8129 (Rigaku Corp.) from room temperature to 773 K under nitrogen flow of 100 mL/min and at a heating rate of 10 K/min.

6-4-5. Fourier Transform Infrared (FT-IR) spectra

IR (400–7800 cm^{-1}) spectra of all the crystals were measured using a Thermo Scientific Nicolet 6700 FT-IR spectrometer.

6-4-6. Differential scanning calorimetry (DSC)

DSC measurement was carried out with a Q2000 differential scanning calorimeter (TA Instruments) in the temperature range 173-373 K at a heating rate of 10 $K \cdot min^{-1}$ and a cooling rate of 5 $K \cdot min^{-1}$ under a flow of N_2 gas (flow rate 50 $mL \cdot min^{-1}$).

6-4-7. Powder X-ray diffraction (PXRD) analysis

PXRD patterns were measured using a RINT-Ultima Ⅲ diffractometer (Rigaku) equipped with a TTK 450 low temperature chamber (Anton Paar) with Cu Kα radiation (λ = 1.5418 Å).

6-4-8. Gas adsorption isotherm experiments

CO_2 (195 K) adsorption/desorption isotherms were measured by using a BELSORP-max (MicrotracBEL Corp.). Before the measurement, the sample was heated at 373 K in a vacuum for 20 h for activation by BELPREP-vac (MicrotracBEL Corp.).

6-5. References

1. D. Liu, *et al.*, A Reversible Crystallinity-Preserving Phase Transition in Metal–Organic Frameworks: Discovery, Mechanistic Studies, and Potential Applications. *J. Am. Chem. Soc.* **2015**, *137*, 7740.
2. M. C. Bernini, *et al.*, Reversible Breaking and Forming of Metal-Ligand Coordination Bonds: Temperature-Triggered Single-Crystal to Single-Crystal Transformation in a Metal-Organic Framework. *Chem. Eur. J.* **2009**, *15*, 4896.
3. H. Wu, *et al.*, Methane Sorption in Nanoporous Metal−Organic Frameworks and First-Order Phase Transition of Confined Methane. *J. Phys. Chem. C* **2009**, *113*, 7, 3029.
4. Y. Liu, *et al.*, Selective gas adsorption and unique phase transition properties in a stable magnesium metal-organic framework constructed from infinite metal chains. *CrystEngComm* **2013**, *15*, 9688.
5. S. Henke, *et al.*, Pore closure in zeolitic imidazolate frameworks under mechanical pressure. *Chem. Sci.* **2018**, *9*, 1654.
6. J. Park & M. Oh, Construction of flexible metal–organic framework (MOF) papers through MOF growth on filter paper and their selective dye capture. *Nanoscale* **2017**, *9*, 12850.
7. P. Horcajada *et al.*, How Linker's Modification Controls Swelling Properties of Highly Flexible Iron(III) Dicarboxylates MIL-88. *J. Am. Chem. Soc.* **2011**, *133* 17839.
8. J. Liang, *et al.*, A Robust Aluminum Metal-Organic Framework with Temperature-Induced Breathing Effect. *ACS Mater. Lett.* **2020**, *2*, 220.
9. J. Pang, *et al.*, Solvent-Assisted, Thermally Triggered Structural Transformation in Flexible Mesoporous Metal–Organic Frameworks. *Chem. Mater.* **2019**, *31*, 8787.
10. S. Jeoung, *et al.*, Tuning of the flexibility in metal–organic frameworks based on pendant arm macrocycles. *Chem. Commun.* **2019**, *55*, 8832.
11. L. Yang, *et al.*, A highly sensitive flexible metal–organic framework sets a new

benchmark for separating propyne from propylene. *J. Mater. Chem. A* **2018**, *6*, 24452.

12. X. Lv, *et al.*, Flexible metal–organic frameworks for the wavelength-based luminescence sensing of aqueous pH. *J. Mater. Chem. C* **2018**, *6*, 10628
13. H. Liang, *et al.*, Flexible self-supported metal–organic framework mats with exceptionally high porosity for enhanced separation and catalysis. *J. Mater. Chem. A* **2018**, *6*, 334.
14. R. S. Forgan, Modulated self-assembly of metal–organic frameworks. *Chem. Sci.* **2020**, *11*, 4546.
15. L. Zhang & Y. Hu, A Systematic Investigation of Decomposition of Nano $Zn_4O(C_8H_4O_4)_3$ Metal−Organic Framework. *J. Phys. Chem. C* **2010**, *114*, 2566.
16. G. C. Shearer, *et al.*, Defect Engineering: Tuning the Porosity and Composition of the Metal-Organic Framework UiO-66 via Modulated Synthesis. *Chem. Mater.* **2016**, *28*, 3749.
17. W. Liang, *et al.*, Tuning Pore Size in a Zirconi-um-Tricarboxylate Metal-Organic Framework. *CrystEngComm* **2014**, *16*, 6530.
18. H. Wu, *et al.*, Unusual and Highly Tunable Missing-Linker Defects in Zirconium Metal-Organic Framework UiO-66 and Their Important Effects on Gas Adsorption. *J. Am. Chem. Soc.* **2013**, *135*, 10525.
19. F. Zhang, *et al.*, Synergetic Catalysis of Palladium Nanoparticles Encaged within Amine-functionalized UiO-66 in Hydrodeoxygenation of Vanillin in Water. *Green Chem.* **2016**, *18*, 2900.
20. M. J. Cliffe, *et al.*, Correlated Defect Nanoregions in a Metal-Organic Framework. *Nature Commun.* **2014**, *5*, 4176.
21. A. Kondo, *et al.*, Novel Expansion/Shrinkage Modulation of 2D Layered MOF Triggered by Clathrate Formation with CO_2 Molecules. *Nano Lett.* **2006**, *6*, 2581.
22. Y. Cheng, *et al.*, Reversible Structural Change of Cu-MOF on Exposure to Water and Its CO_2 Adsorptivity. *Langmuir* **2009**, *25*, 4510.
23. S. Chen, The roles of imidazole ligands in coordination supramolecular systems.

CrystEngComm **2016**, *18*, 6543.

24. N. Shida, *et al.*, Redox chemistry of π-extended tellurophenes. *Commun. Chem.* **2019**, *2*, 124.
25. Y. Zhou, *et al.*, The influence of different N-substituted groups on the mechanochromic properties of 1,4-dihydropyridine derivatives with simple structures. *RSC Adv.* **2017**, *7*, 51444.
26. K. Fujii, *et al.*, Conformational Equilibrium of Bis(trifluoromethanesulfonyl) Imide Anion of a Room-Temperature Ionic Liquid: Raman Spectroscopic Study and DFT Calculations. *J. Phys. Chem. B* **2006**, *110*, 8179.
27. C. Li, *et al.*, Self-assembly of [2]pseudorotaxanes based on pillar[5]arene and bis(imidazolium) cations. *Chem. Commun.* **2010**, *46*, 9016.

Chapter 7

General conclusion

In this thesis, I adopted the component of ILs, bis(trifluoromethylsulfonyl)imide (NTf_2^-), to explore phase/structure transformable CPs. I principally showed two topics, that is, (1) structure transformations of CPs by an uptake/release of uncoordinated/coordinated guest molecules, and (2) phase transition behaviors of CPs by thermal stimuli without the participation of guest molecules.

(1) The investigation of structure transformations in CPs not only demonstrated the gas adsorption sites of CPs (chapter 2), but also provided a strategy to improve gas adsorption performances of CPs (chapter 3) as well as reduced structure dimensionality of CPs by recombination of coordination bonds induced by guest removal (chapter 6).

(2) The novel strategy of introducing bulky fluorinated NTf_2^- anions for creating fluid space not only served as the foundation for developing more crystalline CPs with interesting thermal-stimuli responsive properties (chapter 4), but also initiated a new branch of CPs that can convert to glass and/or liquid states without decomposition (chapter 5).

Although the bulky fluorinated anion, NTf_2^- has been widely used in ILs since the ILs including NTf_2^- anions usually have high stability and low viscosity, it is rarely used in CPs as the building block. In this thesis, NTf_2^- anion plays the key for diverse phase/structure transformations in CPs due to its flexible structure and ability to weaken intermolecular interactions. The strategy of introducing such bulky and flexible fluorinated anions to CPs will break with the stereotype images of crystalline CPs and open up a way to make hybrid amorphous materials.

List of publication

Chapter 2

Understanding the interactions between the bis(trifluoromethylsulfonyl)imide anion and absorbed CO_2 using X-ray diffraction analysis of a soft crystal surrogate

Xin Zheng, Katsuo Fukuhara, Yuh Hijikata, Jenny Pirillo, Hiroyasu Sato, Kiyonori Takahashi, Shin-ichiro Noro, and Takayoshi Nakamura

Commun. Chem., in revision

Chapter 4

A Synchronous Change in Fluid Space and Encapsulated Anions in a Crystalline Polymethylene Unit Containing Metal-Organic Framework

Xin Zheng, Hiroyasu Sato, Kiyonori Takahashi, Shin-ichiro Noro, and Takayoshi Nakamura

Cryst. Growth Des., **2020**, *20*, 3596.

Chapter 5

Enhancement of ionic conductivity by amorphization of three-dimensional coordination polymer

Xin Zheng, Kiyonori Takahashi, Masaru Kato, Yohei Uemura, Daiju Matsumura, Ichizo Yagi, Shin-ichiro Noro, and Takayoshi Nakamura

to be submitted.